Raman, Time-Domain Photoacoustic and Terahertz Spectroscopy of some Inorganic, Organic and High Energy Materials

A Thesis submitted for the award of the degree of

Doctor of Philosophy in Physics

by

Archana Kumari

15ACPA05

Supervisor: Prof.Anil Kumar Chaudhary



University of Hyderabad Hyderabad, India November 2020

Declaration

I, Archana Kumari, hereby declare that the work reported in this thesis entitled "Raman, Time-Domain Photoacoustic and Terahertz Spectroscopy of some Inorganic, Organic and High Energy Materials" is original and has been carried out by me under the supervision of Prof. Anil Kumar Chaudhary, Professor in ACRHEM (School of Physics), University of Hyderabad, Hyderabad, Telangana, India, as per the Ph.D. ordinances of the University, which is also free from plagiarism. I further declare that this work has not been submitted for the award of a research degree of any other University. I hereby agree that my thesis can be deposited in Shodhganga /INFLIBNET. A report on plagiarism statistics from the University Librarian is enclosed.

Archana Kumori

Archana Kumari

Reg. No: 15ACPA05

9,11

Prof. Anil Kumar Chaudhary

Thesis Supervisor,

ACRHEM,

University of Hyderabad.

Dr. Anil Kr. Chaudhary Professor (Physics)

Advanced Centre of Research in High Energy Materials (ACRHEM), UNIVERSITY OF HYDERABAD

HYDERABAD-500 046. T.S. INDIA.

Prof. Anil Kumar Chaudhary

Tel.: +91-40 2313 8807 Fax: +91-40 2301 0227

E-mail: akcsp@uohyd.ernet.in

anilphys@uohyd.ernet.in



ACRHEM

University of Hyderabad, Prof. C. R. Rao Road, Gachibowli, Hyderabad 500046, Telangana, India

Certificate

This is to certify that the thesis entitled "Raman, Time-Domain Photoacoustic and Terahertz Spectroscopy of some Inorganic, Organic and High Energy Materials" being submitted to the University of Hyderabad by Archana Kumari(Reg. No. 15ACPA05), for the award of the degree of Doctor of Philosophy in Physics, is a record of bonafide work carried out by her under my supervision and is free of plagiarism. The matter embodied in this report has not been submitted to any other University or Institution for the award of any degree or diploma.

Prof. Anil Kumar Chaudhary

(Supervisor) Anil Kr. Chaudhary

Professor (Physics)
Advanced Centre of Research in
High Energy Materials (ACRHEM),
UNIVERSITY OF PROFESSABAD
HYDERABAD-500 046, T.S. INDIA

Director

ACRHEM Director ACRHEM

Dean

School of Physics
DEAN
School of Physics

University of Hyderabad Hyderabad-500 046, INDIA



CERTIFICATE

This is to certify that the thesis entitled "Raman, Time-Domain Photoacoustic and Terahertz Spectroscopy of some Inorganic, Organic and High Energy Materials" submitted by Archana Kumari bearing registration number 15ACPA05 in partial fulfillment of the requirements for award of Doctor of Philosophy in physics at ACRHEM, School of physics, University of Hyderabad is a bonafide work carried out by him under my supervision and guidance. This thesis is free from plagiarism and has not been submitted previously in part or in full to this or any other University or Institution for award of any degree or diploma. Further, the student has the following publications before submission of the thesis for adjudication.

- Archana Kumari, A. K. Chaudhary, and M. Venkatesh, "Linear and nonlinear temperaturedependent transmission/absorption characteristics of cadmium telluride crystal for terahertz generation," Appl.Opt. 59,3417-3421,(2020)
- Archana Kumari, A. K. Chaudhary, Rajasekhar K. "Study of charge transfer mechanism of PEDOT polymer for detection of solid TEX and CL-20 explosives using pulsed photoacoustic technique" Spectrochim Acta A Mol Biomol Spectrosc. 241, 118597 (2020)
- Ramachandran K., Archana Kumari, Jitendra Acharya, Anil Kumar Chaudhary, Evaluation
 of PEDOT as a photoacoustic sensor for the detection of high energy materials using timeresolved pulsed photoacoustic and Raman spectroscopy
 Status: Review in JOLT(Journal of Optics and Laser Technology)
- Archana Kumari, Anil Kumar Chaudhary, Detection of RDX, TNT, and HMX Using PEDOT
 Optode in Pulsed Photoacoustic Spectroscopy A Non-Radiative Decay Technique
 Status: Under Revision with Applied Physics B
- Archana Kumari, Ramachandran K., Jitendra Acharya, Anil Kumar Chaudhary, Methodology for the use of PEDOT polymer as an active host medium for detection of High Energy Materials (HEMs) using Raman Spectroscopy Status: Submitted to MethodX
- Archana Kumari, Hanna J Maria, A.K. Chaudhary, and S. Thomas, Time Domain Pulsed Photoacoustic Technique to Study the Effect of Organic and Inorganic Fillers on Thermal and Optical Properties of Natural Rubber/Chlorobutyl Rubber Blend Nanocomposites Status: Under Revision in PRAMANA
- 7. Archana Kumari, D. Ganesh and A.K. Chaudhary, Use of Time domain Terahertz Spectroscopy for the characterization of Antibiotic Cefixime drug obtained from different origin along with assessment of their quality Status: Communicated to International Journal of Pharmaceutics

Further, the following courses have been taken as the part of the course work:

Course No.	Course offered at	Title of the course	Credits	Pass/Fail
1	ACRHEM	Introduction to Non-Linear Optics	4	Pass
2	SoP	Advanced Experimental techniques	4	Pass
3	SEST	Introduction to Nanoscience and Engineering	4	Pass
4	ACRHEM	Research methodology	4	Pass

Supervisor

Prof. Anil Kumar Chaudhary ACRHEM University of Hyderabad

Hyderabad, India

Dr. Anil Kr. Chaudhary
Professor (Physics)
Advanced Centre of Research in
High Energy Materials (ACRHEM),
UNIVERSITY OF HYDERABAD
HYDERABAD-500 046, T.S. INDIA.

Director

ACRHEM

University of Hyderabad

Hyderabad, India

Director

Dean

School of Physics

University of Hyderabad

Hyderabad, India

DEAN

School of Physics University of Hyderabad Hyderabad-500 046, INDIA

Acknowledgement

It is my great pleasure to express my sincere gratitude to the people who have been a constant source of inspiration during the course of my doctoral thesis.

Firstly, I would like to express my sincere gratitude to my advisor **Prof. Anil Kumar Chaudhary** for the continuous support, patience and motivation during the entire course.

Besides my advisor, I would like to thank the rest of my thesis committee: **Prof. Soma Venugopal Rao** and **Prof. Nirmal K. Viswanathan** for their insightful comments which incented me to widen my research area from various perspectives and encouragement. This journey would not have been complete without their constant support.

Further, I am grateful to the former and present directors of ACRHEM, Dr. V Kameshwara Rao and former Dean (Prof. Bindu A. Bambah), and present dean, Prof. A. Chatterjee for providing me all the school level laboratory facilities.

I am thankful to all the non-teaching staff and lab operators of ACRHEM and school of Physics for their help and support.

In addition I thank University of Hyderabad administrative sections for their kind cooperation in dealing with official works, whenever the need arose.

I am very thankful to my seniors, labmates and juniors for their help and support during my research work. My earnest thanks to our collaborators, Prof. S. Thomas, Dr. K. Rajshekhar and Dr. Bikas K. Sikdhar for their fruitful discussions and suggestions.

Undoubtedly, I am indebted to my family for their unconditional love and support without whom this journey would not have been possible. I am very much grateful to my parents for being my anchor and helping me in every walk of life. I feel blessed to have my sisters who have always believed in me.

Beyond everything, I am highly grateful to God, the omnipresent, for blessing me all the way throughout my life.

Table of Contents

			4		4
C	U.	ni	ľΩ	n	TC
	U.			ш	

Declarationi	
Certificateii	
Acknowledgementsiii	
Table of Contentsiv	
List of Tablesv	
List of Figuresvi	
Chapter 1	9
1.Introduction	9
Overview:	10
UV-Vis-NIR Interaction:	11
Classification of Spectroscopic Tools:	12
Time-Dependent Pulsed Photoacoustic Spectroscopy	13
Raman Spectroscopy	15
Objectives of Raman Spectroscopy in this thesis:	16
Time-Domain Terahertz Spectroscopy	16
Conclusion:	17
References:	18
Chapter 2	21
Experimental Techniques	21
Abstract	21
Wavelength-dependent Spectroscopic Techniques:	22
Time-Dependent Spectroscopic Techniques:	24
Chapter: 3	31
Use of PEDOT Polymer Optode as a Sensor for low-level detection of solid explosives using Tim domain Photoacoustic Spectroscopy	
Abstract	31
Introduction:	32
Section: 1	35
Detection of High Energy Materials (HEMs) Using PEDOT Optode as a Sensing Medium in Pulsed Photoacoustic Spectroscopy	35

Results and Discussion:	40
PA Cell Responsivity:	40
The PA signal Vs acoustic frequency:	41
Effect of Incident laser energy on the PA Signal:	44
Effect of changes in PA signals as a function of data acquisition time:	46
Principle of detection of explosives using PEDOT on the basis of Charge Transfer Mechan	ism: . 48
Minimum detection limit:	50
Interaction of PEDOT with nonexplosive materials containing nitro (-NO ₂) group:	51
Section: 2	52
Time Domain Pulsed Photoacoustic Technique to Study the Effect of Organic and Inorganic on Thermal and Optical Properties of Natural Rubber/Chlorobutyl Rubber Blend Nanocom	posites
Experimental Arrangement:	53
Results and Discussions:	54
Conclusion of the chapter:	60
References:	
Chapter: 4	66
Effect of charge transfer mechanism of PEDOT polymer on Stokes and anti-Stokes Raman lin RDX, HMX, and TNT Explosive samples	
Abstract:	66
Introduction:	67
Experimental Details:	69
Results and Discussion:	69
Conclusion:	88
References:	89
Chapter: 5	93
Study of temperature-dependent non-linear absorption properties of CdTe crystal during the of THz generation and time-domain Spectroscopy of antibiotic Cefixime medicine	
Abstract:	93
Introduction:	94
Section: 1	96
Temperature-dependent Study of linear/nonlinear absorption Properties of CdTeCrystal :	96
Section: 2	103
Application of Time-domain Terahertz Spectroscopy	103

Chapter 6	118
Conclusion and Future Scope	118
Future Scope:	120

- Publications
- Plagiarism Report
- Appendices

List of Tables

Table 2. 1 The Specifications of the Laser System	25
Table 2. 2 Physical parameters of the Laser System	
	26
Table 3. 1 represents the image, size, and density of the samples considered for the study	
frequency modes	
Table 3. 3 Represents the decay time rates of the explosives when mixed with PEDOT polymer	
Table 3. 4 shows the minimum detection limit of the explosive samples in the PA cell	
Table 3. 5 gives the details of the constituents of the samples S1-S5.	
Table 3. 6 The amplitude of the prominent peaks of different samples measured at 1.0 mJ	
Table 3. 7 Comprises the calculation of decay time constants of the samples S1-S5	
Table 3. 8 shows the absorption coefficients of the samples S1-S5	
Table 3. 9 Comprises thermal diffusivity and the penetration depth of the samples s1-s5	
Table 4. 1 Represents the peak assignment of some of the prominent peaks obtained in the Raman	
spectra of pure PEDOT.	70
Table 4. 2 Provides the details of the most prominent peaks observed in the Raman spectra of RDX	and
RDX+PEDOT.	72
Table 4. 3 The NO ₂ vibration mode frequency analysis of pristine RDX and mixed with PEDOT	
(RDX+PEDOT).	
Table 4. 4 The peak assignment of pristine HMX and mixed with PEDOT (HMX+PEDOT)	
Table 4. 5 The NO ₂ vibration mode frequency analysis of HMX and it is mixed with PEDOT (HMX	
PEDOT)	
Table 4. 6 shows the peak assignment of TNT and TNT+PEDOT	
Table 4. 7 The NO ₂ vibration mode frequency analysis of TNX and it is mixed with PEDOT (TNT-	
PEDOT)	82
Table 5. 1 Comparsion of conversion of THz frequency in the visible and IR region	94
Table 5. 2 The crystal's coherence length at considered wavelengths; 800, 850, and 900 nm	
Table 5. 3 shows the details of the polymorphs of the medicine samples of Cefixime procured from	
different pharmaceuticals and used for the study in this chapter	
Table 5. 4 shows the correspondence of various peaks obtained in the Raman Spectra to its	
corresponding bond assignment	. 106
Table 5. 5 Comparsion between THz and Raman Spectroscopy	
Table 5. 6 The absorbance and specific absorbance at THz frequencies; 0.5 THz	. 110

List of Figures

Figure 1. 1 The Electromagnetic Spectra	10
Figure 1. 2 Illustrations of the absorption and emission spectra	11
Figure 1. 3 shows the application of Beer-Lambert's law on a sample irradiated with light of intensit	
I_0	-
Figure 1. 4 The classification of Spectroscopic tools as presented in the thesis	
Figure 1. 5 Schematic diagrams of the experimental setup used by A. G. Bell for the discovery of the	
Photoacoustic Phenomenon	
Figure 1. 6 shows the progress made in the photoacoustic phenomenon since its discovery by A. G.	
in 1880	
Figure 1. 7 Diagram showing the difference between Raman and Rayleigh Scattering when the samp	ple
absorbs light	_
Figure 2. 1 Shows the UV-Vis-NIR Spectrometer	22
Figure 2. 2 Shows the schematic diagram of FTIR Spectrometer	
Figure 2. 3 Shows the schematic diagram of a Raman Spectrometer	
Figure 2. 4 Experimental setup for Photoacoustic Spectroscopy	20
Figure 3. 1 Schematic representation of radiative and nonradiative decay.	33
Figure 3. 2 This figure represents the formation of polaron and bipolaron on the polymeric chain of	
PEDOT responsible for its conduction	
Figure 3. 3 This figure schematically represents the classification of High Energy Materials	
Figure 3. 4 Schematic representation of negative charge on the oxygen atom and positive charge on	
PEDOT in PEDOT: PSS	
Figure 3. 5 UV-Vis spectra of (i) PEDOT: PSS, (ii) UV-Vis spectra of hydrazine hydrate treated	30
PEDOT: PSS	30
Figure 3. 6 "Q" factor Curves of the experimental photoacoustic cell	
Figure 3. 7 This graph represents the photoacoustic cell responsivity.	
Figure 3. 8 Graphs of the various PA modes of frequency domain signal (a) PEDOT, RDX, and	
PEDOT+RDX; (b) PEDOT, TNT, and PEDOT+TNT; (c) PEDOT, HMX, and PEDOT+HMX; (d)	
PEDOT, CL20, and PEDOT+CL20; (e)) PEDOT, TEX, and PEDOT+TEX	12
Figure 3. 9 PA signal as a function of incident laser energy (a) PEDOT; (b) PEDOT+RDX; (c)	43
PEDOT+HMX; (d) PEDOT+TNT; (e) PEDOT+CL20 and (f) PEDOT+TEX	15
Figure 3. 10 variation of PA signal as a function of data acquisition time at 0.5 mJ laser energy of	43
various samples: (a) PEDOT (b) PEDOT+RDX (c) PEDOT+TNT (d) PEDOT+HMX (e)	47
PEDOT+CL20 and (f)PEDOT+TEX.	
Figure 3. 11 Schematic diagram showing the charge transfer between CL 20 and PEDOT	
Figure 3. 12 Represents the FTIR spectra of pure explosives and PEDOT + Explosive samples	
Figure 3. 13 This graph represents the effect of mixing PEDOT to nonexplosive molecules containing vitus (NO) graphs.	
nitro (-NO ₂) groups.	
Figure 3. 14 Time-domain PA Spectra of samples S1-S5	DO

Figure 3. 15 Shows the data acquisition time of samples with their exponential decay nature and their
exponential fit
Figure 3. 16 Represents the procedure for estimation of absorption Coefficient
Figure 4. 1 shows the mechanism of scattering when a sample interacts with a light source
Figure 4. 2 The Raman spectrum of pure PEDOT polymer
Figure 4. 3 (a) shows the Raman spectra of RDX and (b)and the RDX +PEDOT mixture
$Figure\ 4.\ 4\ The\ ratio\ of\ anti-stokes\ to\ stoke\ the\ intensity\ of\ Raman\ spectra\ of\ RDX\ and\ RDX\ -\ PEDOT$
concerning vibration modes
Figure 4. 5 Raman spectra obtained for (a) pristine HMX and (b) PEDOT is mix with HMX76
Figure 4. 6 The ratio of anti-stokes to stoke the intensity of Raman spectra of HMX and HMX - PEDOT
concerning vibration modes
Figure 4. 7 Raman spectra obtained for pristine (a) TNT and (b) TNT and PEDOT
Figure 4. 8 The ratio of anti-stokes to stoke the intensity of Raman spectra of TNT concerning vibration modes.
Figure 4. 9 Intensity variation has been observed for (a) NO ₂ symmetric stretch and (b) NO ₂ asymmetric
stretch of explosives when it is mixed with PEDOT.
Figure 4. 10 The quantum Energy transitions for Raman Scattering represents the broadening of $\pm \delta \upsilon$
change of frequency at the excited state after mixing PEDOT with explosives
Figure 4. 11 (a) The Schematic representation of molecular interaction of oxidized PEDOT with RDX
molecule and (b) shows the shift in the peak of FTIR spectra of explosive molecules when PEDOT is
added to them85
Figure 4. 12 The topology used for the stretching mechanism of three atoms to estimate the reduced
mass of the system
Figure 5. 1 (a) represents the side-view of a photoconductive (PC) antenna and (b) shows the basic
working principle of a PC antenna
Figure 5. 2 (a) UV-Vis-NIR Lambda 650 spectrophotometer and (b) modified spectrometer with the
introduction of the oven with temperature controller
Figure 5. 3 The nonlinear transmission of CdTe using femtosecond laser pulses at different wavelengths
Figure 5. 4 (a & b) shows the variation of transmission of CdTe with respect to Wavelength and
temperature when subjected to UV-Vis-NIR spectrometer
$Figure\ 5.\ 5\ (a)\ Transmission\ vs.\ wavelength\ for\ CdTe\ at\ different\ temperatures\ and\ (b)\ Temperature\ vs.$
Energy of CdTe given by M-W equation. 99
Figure 5. 6 (a) Physical properties of CdTe: (a) Absorption Coefficient and (b) refractive index 99
Figure 5. 7 (a &b): the measured THz temporal profiles of <110>CdTe with respect to incident laser
central wavelength, which is tunable between 780 to 820 nm at input laser power 300 mW. It shows a
variation of THz amplitude with respect to delay time and frequency
Figure 5. 8 (a) Variation of THz amplitude as a function of wavelength and (b) Dependence of THz
radiation on incident angle of laser pulses
Figure 5. 9 (a, b): Terahertz spectrum of medicine samples, (a) Temporal profile of THz-pulse, and
(b) frequency domain spectra

Figure 5. 10 Raman Spectroscopy of medicine samples (1-5)	105
Figure 5. 11 Schematic diagrams explaining the joint region between Raman Spectroscopy and ti	me-
domain THz spectroscopy, excerpt taken from reference [27-29].	109
Figure 5. 12 (a)shows the absorbance strength, and (b) represents the specific absorbance of all	
samples(S1-S5) at different frequencies.	111
Figure 6. 1 It briefly illustrates the link between different techniques used in the thesis	119

Chapter 1 Introduction

1.1 Abstract

This chapter briefly introduces light-matter interaction and its importance in studying materials' internal structure with spectroscopic tools such as Photoacoustic, Terahertz, and Raman spectroscopy. The chapter begins with an introduction to spectroscopy. It then focuses on how different spectroscopic techniques came into being and tracing their developmental path since their conception and the progress made to date. Although this chapter takes us on a journey since discovering the phenomena to the state-of-the-art techniques involved in the present day scenario, the discussion primarily revolves around our interest and the problems we set out to tackle in this thesis.

1.2 Overview:

We perceive almost 80% of the world around us by using our sense of sight and can safely claim that 'light' is the connection between us and the universe. When one thinks about 'light,' the first thing that comes to mind is 'visible light,' which is that portion of the electromagnetic spectrum perceived by the human eye (Fig: 1.1). Observing and studying the world around us is only possible if this 'light' interacts with the matter present around us and helps us see them. Working with 'light,' one can either study its interaction with itself at different wavelengths and frequencies or study its interaction with matter. Thus, we can scientifically conclude that any light source is nothing but a 'probe' to determine the subject and its physical or chemical properties.

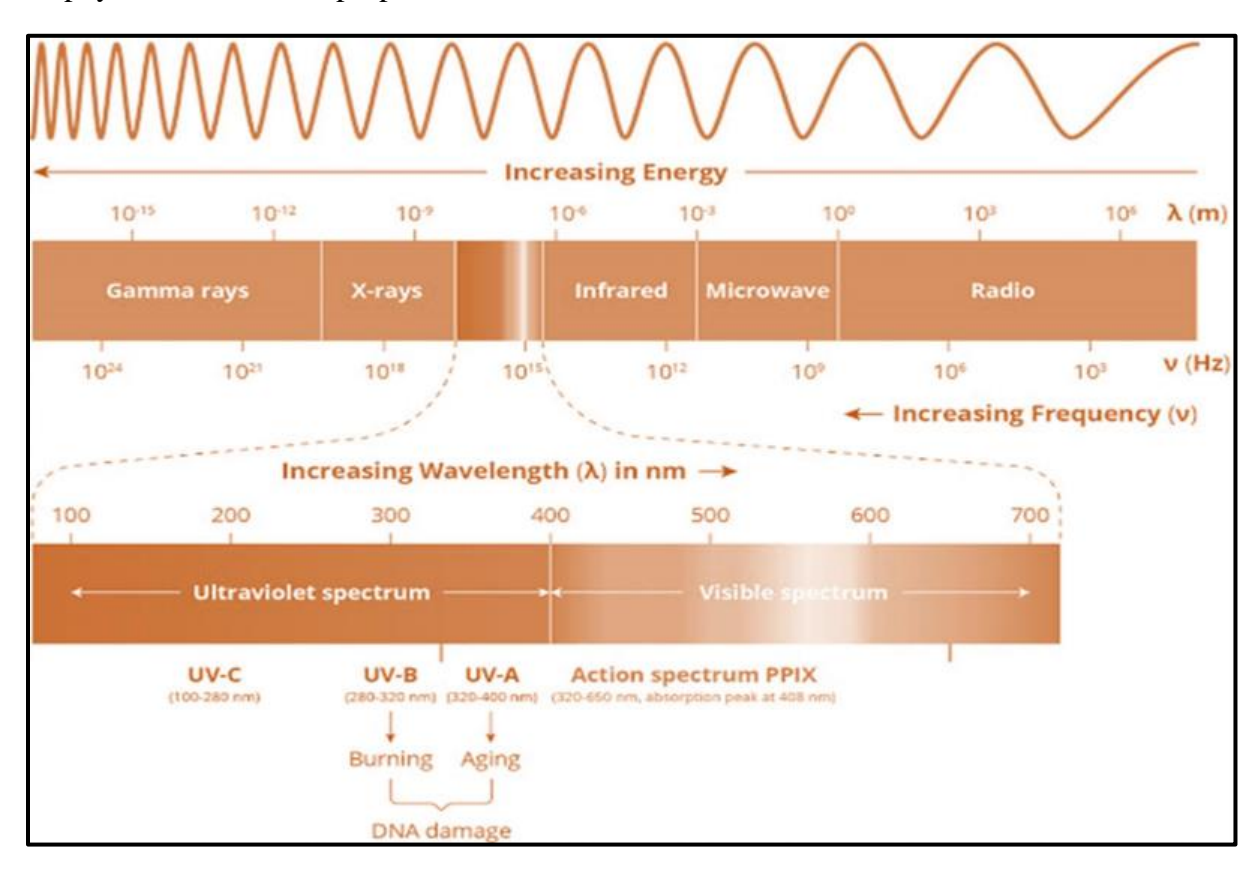


Figure 1. 1 The Electromagnetic Spectra

When light interacts with matter, we conceptualize the interaction between photons (energy packets) of light that have a particular wavelength and frequency associated with them either in the form of quanta/photon or in a wave the atoms/molecules present in a substance. These interactions give rise to an essential spectroscopic tool known as spectra, two types-Absorption, and Emission Spectra detected using an instrument known as a Spectrograph or Spectrometer forms the basis of spectroscopy. It is well-known that E.M. radiations carry energy in the form of waves, and upon interacting with particles, they produce some changes like the particle. This interaction can occur when a photon beam interacts with matter can be of many types, such as attenuation, scattering, transmission, absorption, and emission. When an electron absorbs a packet of energy (hv) as a photon in the ground state, it gets excited and goes to the excited state. The spectra obtained, in this case, is known as absorption spectra. An electron from an excited state falls to the ground state in emission spectra and releases a photon of energy, hv. This

phenomenon gives rise to emission spectra, which is shown in fig.1.2. Different parts of E.M. Spectra interact differently with the matter. Each piece of the ranges, beginning with gamma rays to radio waves, contains quantum energy suitable for excitation of a different physical phenomenon. It depends on the wavelength/frequency associated with that portion of the spectra. Some of the types of interaction required to resolve and understand the problems we set out to find a solution to this thesis are discussed briefly.

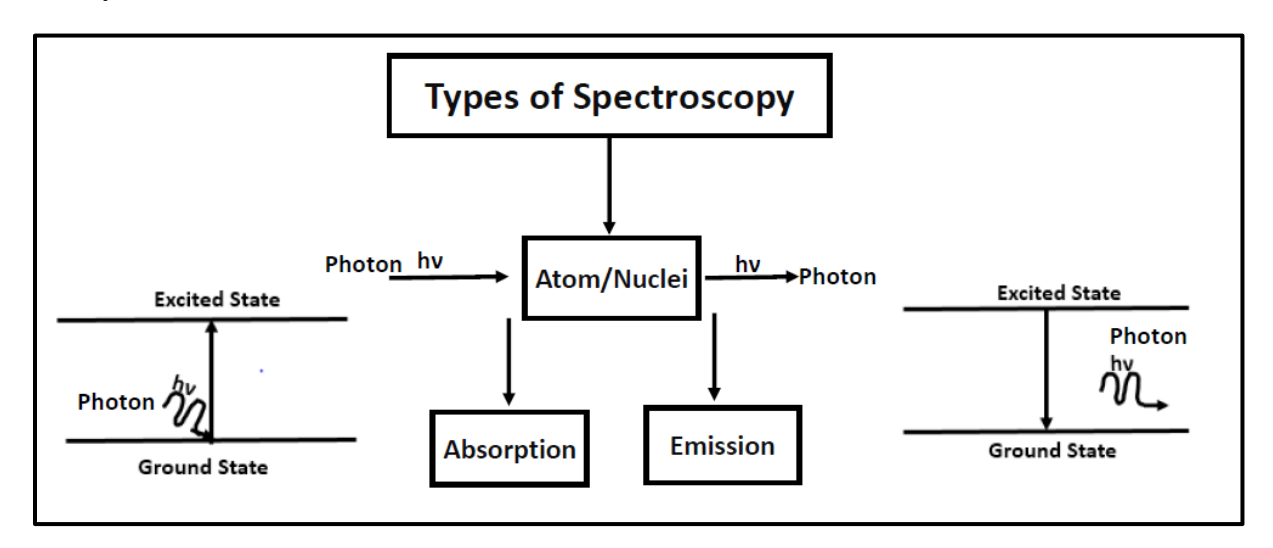


Figure 1. 2 Illustrations of the absorption and emission spectra

1.3 UV-Vis-NIR Interaction:

The corresponding wavelengths for ultra-violet, visible, and near infra-red radiation are as follows: 300-400 nm, 400-765 nm, and 765-3200 nm; respectively. The basic principle of absorption Spectroscopy is given by Beer-Lambert's law, as shown in fig.1.3. Equation 1-5 provides the relation between incident light of intensity, Io, and transmitted light of intensity, I.

Transmittance
$$(T) = \frac{I}{I_o}$$
 (1)

% Transmittance
$$(T) = \frac{I}{I_0} * 100$$
 (2)

$$\log(1/T) = \log(I_o/I) \tag{3}$$

$$Absorbance(Abs) = \log(1/T) \tag{4}$$

Transmitted Light,
$$I = I_o * 10^{-k*c*l}$$
 (5)

In Equation 5, 'k' is the proportionality constant, 'l' represents the optical path length traveled by the incident light, and 'c' is the sample's concentration. Thus, equation 4 & 5 can be written as:

Transmittance
$$(T) = \frac{I}{I_0} = 10^{-kcl}$$
 (6)

$$Absorbance(Abs) = \log(1/T) = -kcl \tag{7}$$

From the above equations, it is observed that the transmittance is not proportional to sample concentration, even though the sample's absorbance is proportional to it, as explained by Beer-Lambert's rule. The effect of scattered or reflected light must be negligible before using Beer-Lambert's law to measure transmitted light from any sample.

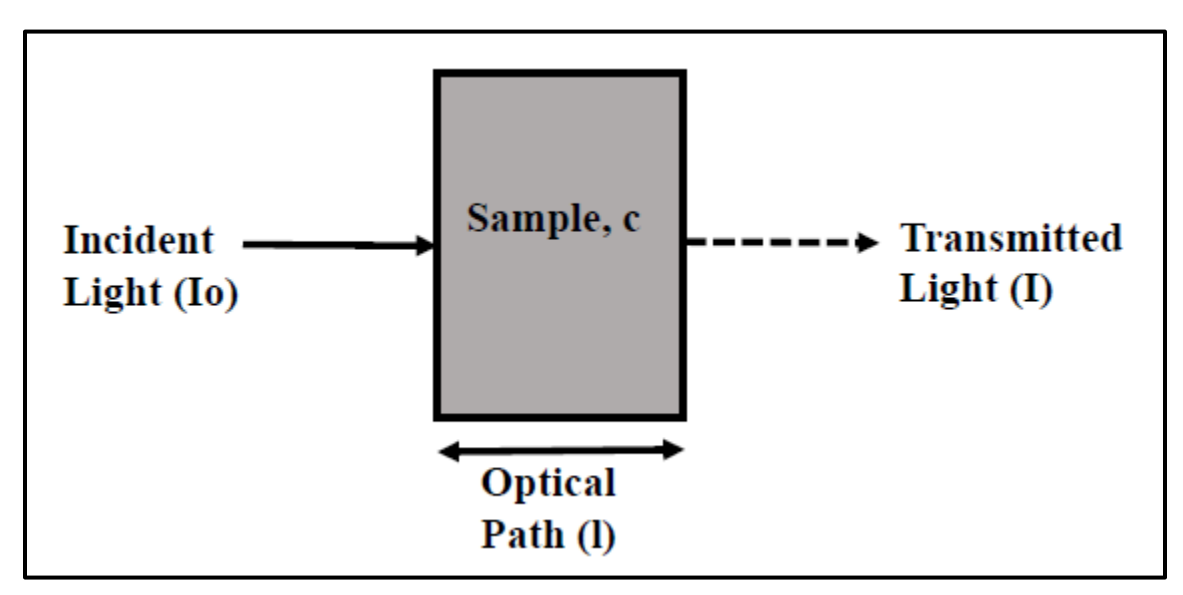


Figure 1. 3 shows the application of Beer-Lambert's law on a sample irradiated with light of intensity, I_0 .

1.4 Classification of Spectroscopic Tools:

In this thesis, we have used different spectroscopic techniques to study and analyze different materials, as shown in Fig.1. 4.

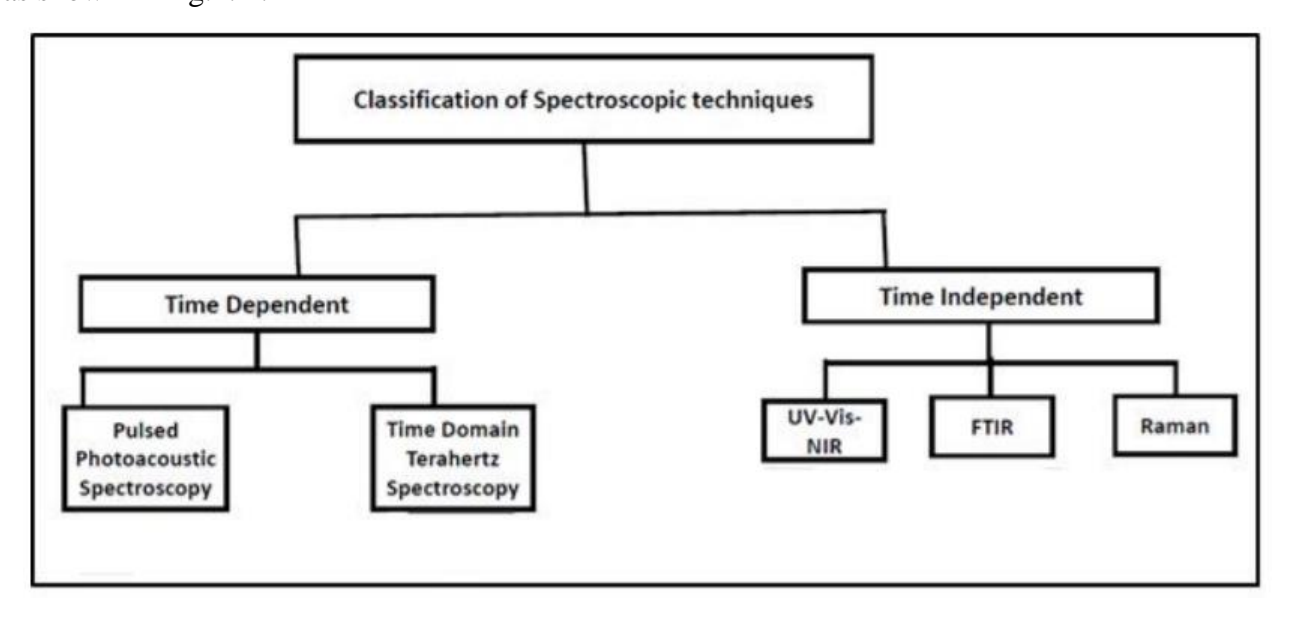


Figure 1. 4 The classification of Spectroscopic tools as presented in the thesis

1.5 Time-Dependent Pulsed Photoacoustic Spectroscopy

• The Discovery:

On 2nd November 1880, Alexander Graham Bell and his associate, Summer Tainter, first reported the Photoacoustic Phenomenon [1]. They described a device called a Photo-phone and used it to propagate speech (sound) using light as a medium of transfer. The schematic of the setup used by A. G. Bell is given in Fig.1.5.

When a modulated beam of light strikes a thin film/diaphragm, it produces a sound. Bell was able to hear this sound without any electrical means. He described this phenomenon as "Sound produced by Light" or the "Photoacoustic phenomenon." This phenomenon was further established for liquid as well as gaseous samples. From the experiments performed, it was concluded that the reason for the photoacoustic effect was the absorption of light by the sample under study, and it was found to be proportional to the intensity of the light. The condensation and rarefaction, which takes place each time the sample is subjected to a source of light (pulsed laser light in our case) produces a sonorous vibration which is detected by the detector as 'sound' thus giving rise to the photoacoustic phenomenon [1-2].

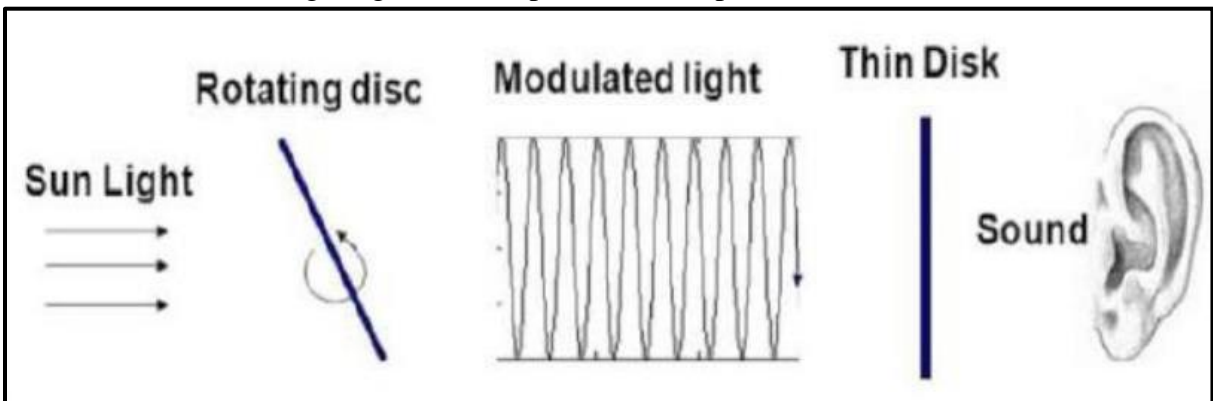


Figure 1. 5 Schematic diagrams of the experimental setup used by A. G. Bell for the discovery of the Photoacoustic Phenomenon

• The Progress:

The initial excitement with the invention of the photoacoustic effect faded off very soon after its discovery. Only after 50 years of the discovery, when the microphones became available, interest in the photoacoustic experiments was revived. However, it was concentrated more on the gaseous samples. The photoacoustic effect applications were demonstrated in the microwave, ultraviolet, and visible range as well.

The discovery of LASERs brought a revolution in photoacoustic (PA) spectroscopy because with the help of high power and monochromatic radiation, it became possible to increase the PA instrument's sensitivity by several orders. The first use of LASER radiation as a source for photoacoustic experiment dates back to 1968 when Kerr and Atwood used a tunable pulsed Ruby LASER to measure the absorption band of water vapor in room air with a spectral resolution of 0.2 angstroms. Using a CO₂ LASER, they were also able to measure the absorption coefficient in the CO₂+N₂ mixture. At the same time, the photoacoustic method underwent numerous modifications. A resonant absorption cell was used for the first time to

detect low concentration impurities in gases. By the year 1970, the photoacoustic method was able to identify weak absorption bands in gases. The high power of the laser pulse, high resolution, and reduced signal-to-noise ratio made it possible to study non-linear and multi-photon absorption. However, it took further 40 years for the work to begin in the field of solid-state photoacoustic effect. The flowchart in fig.1.6 depicts the progress made so far in this field.

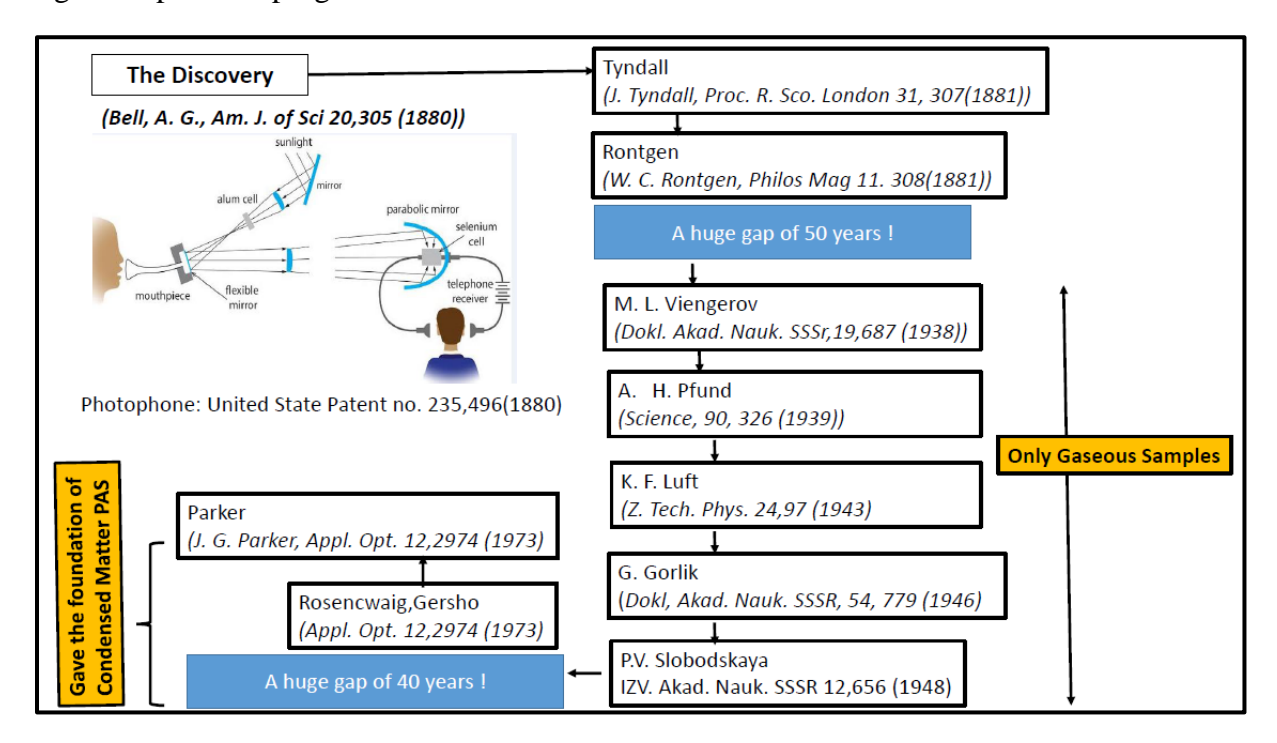


Figure 1. 6 shows the progress made in the photoacoustic phenomenon since its discovery by A. G. Bell in 1880

Theoretical Aspects related to Photoacoustic Phenomena:

The theory of the photoacoustic effect in solid-state samples is based on the R-G Theory [3]. The availability of high-intensity pulsed laser sources makes it possible to study the temporal response in which the solid sample is excited by a single optical pulse. The experimental details are explained in detail in the forthcoming chapters. The heat flow equation of the solid PA-Cell and other information can be found in Appendix A.

• Objectives of Photoacoustic Spectroscopy technique in this thesis:

- To aim towards the development of a cost-effective, reliable, and highly sensitive sensor for the low-level detection of solid explosives in the visible region of the E.M. spectra
- To study the role of conducting polymer, PEDOT as a sensing medium for explosives using visible 532 nm wavelength of the laser
- To analyze the effects of fillers used as reinforcements to increase the durability and strength of the rubber polymer

1.6 Raman Spectroscopy

• Overview:

In 1928, Chandrasekhar Venkata Raman discovered a phenomenon with the help of fundamental instruments; sunlight as the source, telescope as the collector, and just his own eyes as the detector. Gradually, many improvements were made to achieve the present state- of- the art Raman Spectrometer. It is most widely known for determining vibrational and rotational modes of molecules. It is also commonly used to identify unknown molecules as it provides specific structural fingerprint spectra. However, a substance must be Raman-active(polarizability can be changed during the vibration) to qualify for study using Raman Spectroscopy. Although Raman spectra are known to give information about the vibrational transitions, it can also provide information regarding the electronic transitions between ground states and low-energy excited states. Fig. 1.7 represents the interaction of materials with a light beam.

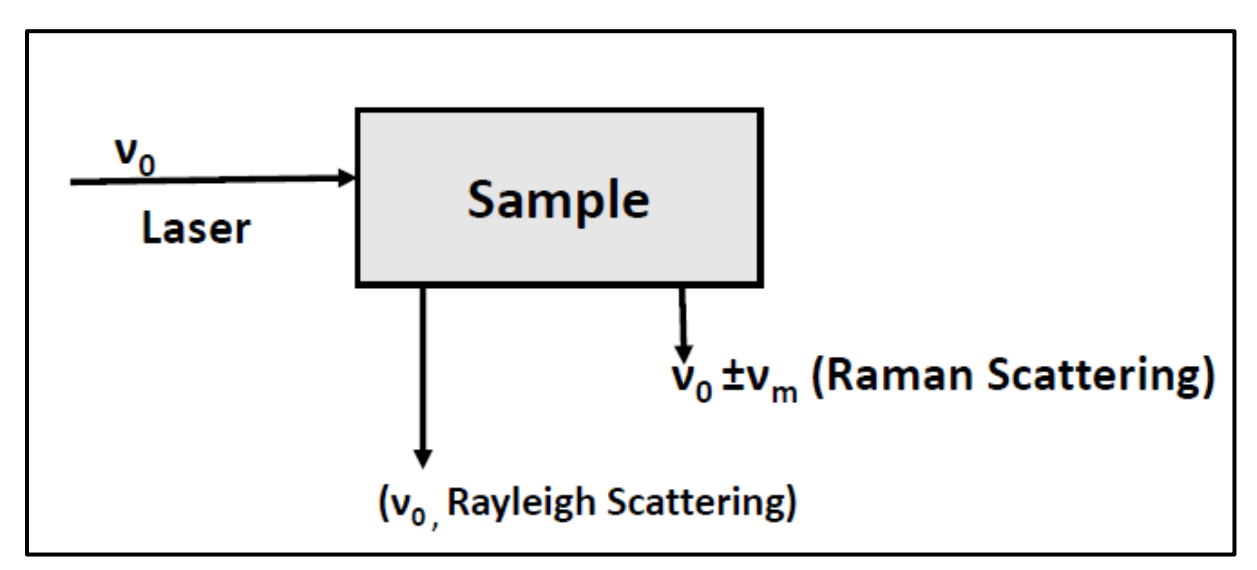


Figure 1. 7 Diagram showing the difference between Raman and Rayleigh Scattering when the sample absorbs light

The light from the sample gets scattered in the form of Rayleigh and Raman scattering. Rayleigh scattering is strong and is of the same frequency (v_0) as that of the incident light, whereas Raman scattering is weak (10^{-5} times the incident beam), having frequencies, v_0+v_m or v_0-v_m , where v_m is the molecular vibrational frequency. The term (v_0-v_m) represents the Stokes line, and (v_0+v_m) is the anti-Stokes line. Also, the Stokes lines are more intense than the anti-Stokes lines under normal circumstances, but Stokes lines of the spectrum are considered as both lines contain the same information about the molecule [4].

• Objectives of Raman Spectroscopy in this thesis:

- To find an alternative method for the detection of explosives with the help of Raman Spectroscopy using the study of the role of PEDOT polymer as a sensing medium by studying the change in the anti-Stokes/Stokes ratio
- To bridge the gap between Raman and terahertz spectroscopy based on studies conducted on antibiotic drug polymorphs, Cefixime.

1.7 Time-Domain Terahertz Spectroscopy

• Overview:

Terahertz frequency region consists of the area between microwave and infrared frequency domains and extends from $0.1x\ 10^{12}\ Hz\ (=3mm)$ to $10x10^{12}\ Hz\ (=0.03mm)$. These waves are also known as far-infrared, sub-millimeter, or T-rays (fig. 1). THz interacts energetically with polar molecules. It can easily penetrate through non-polar and non-metallic materials such as clothes, newspapers, etc. Hence, it is used to study vibrational-rotational and translation lines in all phases of matter; solid, liquid, or gas. Terahertz radiation is emitted from all bodies that possess a temperature of more than 10 K. With the progress in semiconductor technology and ultrafast Laser technology, it has become easier to generate and detect this radiation. THz radiation finds its application in homeland security, the IT industry, and the health sector. The sources of THz radiation can be coherent as well as incoherent sources. Some examples of incoherent sources are mercury arc lamp and silicon carbide globar lamps. They produce continuous THz radiation when they are heated up. However, coherent sources provide either continuous or pulsed waves. Gunn oscillators, IMPATT diodes, FIR Lasers, germanium Lasers, and Quantum Cascade Lasers are famous examples of continuous-wave terahertz sources [5-6].

Research in the field of Terahertz spectroscopy caught momentum only since the 1920s. This frequency has remained one of the least researched regions because of the difficulties faced in its generation detection. In recent times, most of the work related to THz spectroscopy is focused on imaging in biomaterial identification, detection of cancerous cells, oral health care, dermatology, DNA molecular structure, etc. THz radiation application is based on the materials' response to rotational transitions in molecules, large-amplitude vibrational motions of organic compounds, and lattice vibrations in solids [7-10].

• Objectives of Time-Domain Terahertz spectroscopy:

- To study the temperature-dependent properties of CdTe to explain the changes in the physical nature of the crystal when subjected to femtosecond laser pulses for a long duration of time
- Generation of THz frequency using CdTe crystal
- To study the temperature-dependent properties such as the energy of the bandgap, determination of Urbach-tail, and non-linear absorption with the help of a self-modified temperature-dependent spectrometer

• To use time-domain terahertz spectroscopy for characterization of an antibiotic Cefixime drug obtained from the different origin along with an assessment of their quality

1.8 Conclusion:

In this chapter, we have described various laser-based spectroscopic techniques used in the thesis. A visible (532 nm) nanosecond laser was used for photoacoustic spectroscopy. The purpose of the C.W. laser (532nm and 785nm) for Raman spectroscopy has been explained. We have used femtosecond laser for generation and detection of Terahertz using non-linear CdTe crystal. Along with that, FTIR and Raman spectroscopy has been used to establish all the new results obtained. It also highlights each spectroscopic technique's various essential objectives and provides a brief idea about the problems considered for tackling this thesis.

References:

- 1. A. G. Bell, On the Production and Reproduction of Sound by Light, Am. J. of Sci. 20, 305 (1880).
- 2. A. G. Bell, 'Upon Production of Light by Radiant Energy', by, The London, Edinburgh, and Dublin Philosophical Magazine and J. of Sc.11, 68 (1881)
- 3. Allan Rosencwaig and Allen Gersho, Theory of the photoacoustic effect with solids, J. of App. Phys. 47, 64 (1976)
- 4. M. López-López, C. García-Ruiz, Infrared and Raman spectroscopy techniques applied to identification of explosives, Trends Analyst. Chem. 54 36-44 (2014)
- 5. D. F. Plusquellic, K. Siegrist, E. J. Heilweil and O. Esenturk, Applications of Terahertz spectroscopy in biosystems, Chem Phys Chem, 8, 2412-2431 (2007)
- 6. S. Dexheimer, Terahertz Spectroscopy: Principles and Applications in Terahertz Spectroscopy: Principles and Applications, Taylor & Francis, 360 (2007)
- 7. M. C. Kemp, P. F. Taday, B. E. Cole, J. Cluff, A. J. Fitzgerald, and W. R. Tribe, Security applications of terahertz technology, Proc. SPIE, 5070, 44–52, (2003)
- 8. M. Venkatesh, K.S. Rao, T.S. Abhilash, S.P. Tewari, A.K. Chaudhary, Optical characterization of GaAs photoconductive antennas for efficient generation and detection of Terahertz radiation, Optical Materials 36, 596–601 (2014)
- 9. M. D. King, W. D. Buchanan, and T. M. Korter, Understanding the Terahertz Spectra of Crystalline Pharmaceuticals: Terahertz Spectroscopy and SolidState Density Functional Theory Study of (S)-(+)-Ibuprofen and (R.S.)- Ibuprofen, J. Pharm. Sci., 100(3), 1116–1129, (2011)
- 10. M. He, A. K. Azad, S. Ye, and W. Zhang, Far-infrared signature of animal tissues characterized by terahertz time-domain spectroscopy, Opt. Commun., 259(1), 389–392, (2006)
- G. Mogilevsky, L. Borland, M. Brickhouse, A. W. Fountain III, Raman Spectroscopy for Homeland Security Applications, Hindawi Publishing Corporation International Journal of Spectroscopy. 808079 1-12 (2012)
- 12. M. A. Bañares, G. Mestl, Structural characterization of operating catalysts by Raman spectroscopy, Adv.Catal. 52 43-128 (2009)
- 13. I. R. Lewis, N. W. Daniel, P. R. Griffiths, Interpretation of Raman spectra of nitro-containing explosive materials. Part I: Group frequency and structural class membership, Appl. Spectrosc. 51 1854-1867 (1997)

- 14. Finot, Eric, Thibault Brulé, Padmnabh Rai, Aurélien Griffart, Alexandre Bouhélier, and Thomas Thundat, Raman and photothermal spectroscopies for explosive detection, In Micro-and Nanotechnology Sensors, Systems, and Applications V, International Society for Optics and Photonics. 8725 872528 (2013)
- 15. K. S. Rao, A. K. Chaudhary, F. Yehya Investigation of solid carbon blacks using pulsed photoacoustic and double resonant Raman spectroscopy for the identification of trinitrotoluene, Sens. Actuators B Chem. 231 830-836 (2016)
- 16. Y. Liu, R. Perkins, Y. Liu, N. Tzeng, Normal mode and experimental analysis of TNT Raman spectrum, J. Mol. Struct. 1133 217-225 (2017)
- 17. S. Gulia, K. K. Gulati, V. Gambhir, R. Sharma, M. N. Reddy, Trace detection of explosives and their derivatives in stand-off mode using time-gated Raman spectroscopy, Vib. Spectrosc. 87 207-214 (2016)
- 18. I. Ricardo, L. C. Pacheco-Londoño, S. P. Hernández-Rivera, Monitoring the α→β solid-solid phase transition of RDX with Raman spectroscopy: A theoretical and experimental study,' J. Mol. Struct. 970 51-58 (2010)
- 19. P. Jander, R. Noll, Automated detection of fingerprint traces of high explosives using ultraviolet Raman spectroscopy, Appl. Spectrosc. 63 559-563 (2009)
- 20. D. D., Tuschel, A. V. Mikhonin, B. E. Lemoff, S. A. Asher, Deep ultraviolet resonance Raman excitation enables explosives detection, Appl. Spectro. 64 425-432, (2010)
- 21. K. L. Gares, K. T. Hufziger, S. V. Bykov, S. A. Asher, Review of explosive detection methodologies and the emergence of standoff deep U.V. resonance Raman, J. Raman Spectro. 47 124-141 (2016)
- 22. A. Hakonen, P. O. Andersson, M. S. Schmidt, T. Rindzevicius, M. Käll, Explosive and chemical threat detection by surface-enhanced Raman scattering: A review, Anal. Chim. Acta. 893 1-13, (2015)
- 23. A. K. M. Jamil, E. L. Izake, A. Sivanesan, P. M. Fredericks, Rapid detection of TNT in aqueous media by selective label free surface enhanced Raman spectroscopy, Talanta. 134 732-738 (2015)
- 24. M. Horikawa, T. Fujiki, T. Shirosaki, N. Ryu, H. Sakurai, S. Nagaoka, H. Ihara, The development of a highly conductive PEDOT system by doping with partially crystalline sulfated cellulose and its electric conductivity, J. Mater. Chem. C. 3 8881-8887 (2015)
- 25. K. P. Prabha, M. Beliatis, S. Georgakopoulos, V. Stolojan, J. Underwood, M. Shkunov. Laser patterned polymer/nanotube composite electrodes for nanowire transistors on flexible substrates, arXiv preprint ar X iv:1711.06925 (2017)

- 26. C. S. Casari, A. L. Bassi, A. Baserga, L. Ravagnan, P. Piseri, C. Lenardi, M. Tommasini, A. Milani, D. Fazzi, C. E. Bottani, P. Milani, 'Low-frequency modes in the Raman spectrum of sp-sp² nanostructured carbon', Phys. Rev. B 77, 19 195444(2008)
- 27. Iqbal, Zafar, K. Suryanarayanan, Suryanarayana Bulusu, and J. R. Autera, Infrared and Raman spectra of 1,3,5-Trinitro-1,3,5-Triazacyclohexane (RDX)', Picatinny Arsenal Dover, NJ PA-TR-4401 (1972)
- 28. I-M. Chou, Calibration of Raman shifts of cyclohexane for quantitative analyses of methane in natural and synthetic fluid inclusions J. Raman Spect. 46 987-988 (2015)
- 29. J. J. P. Stewart, S. R. Bosco, W. R. Carper, Vibrational spectra of 2, 4, 6-trinitrotoluene and its isotopically substituted analogues, Spectrochim. Acta A. Mol Spect. 42 13-21, (1986)
- 30. J. Clarkson, E. Smith, D. N. Batchelder, A. M. Coats, A theoretical study of the structure and vibrations of 2, 4, 6-trinitrotoluene, J. Mol. Str. 648 203-214, (2003)
- 31. H. Wackerbarth, L. Gundrum, C. Salb, K. Christou, W. Viöl, Challenge of false alarms in nitroaromatic explosive detection device based on surface-enhanced Raman spectroscopy, Appl. Opt. 49 4367-4371(2010)

Chapter 2 Experimental Techniques

2.1 Abstract

This chapter briefly outlines experimental arrangements, Laser systems, devices, and optical components in various experiments performed in the thesis. The practical information involves different spectroscopic techniques such as pulsed Time-Domain Photoacoustic Spectroscopy, Time- Domain Terahertz spectroscopy, and Raman Spectroscopy in detail. One of the chapter's objectives is to present the research methodology and techniques used to perform various experiments in this thesis and emphasize the research design's scope and limitations. The chapter first describes wavelength-dependent spectroscopic methods such as Ultraviolet-Visible-Near Infra-Red spectrometer, Fourier Transform Infrared Spectroscopy, and Raman Spectroscopy. It then also highlights the time-dependent spectroscopic techniques like Photoacoustic and Terahertz spectroscopy.

2.2 Wavelength-dependent Spectroscopic Techniques:

• UV-Vis-NIR Spectrometer:

This instrument provides a means for analyzing liquid, gas, and solid-phase materials through radiant energy in the far and near-ultraviolet, visible, and near-infrared electromagnetic spectrum regions, as shown in fig.1. PerkinElmer spectrometer Scan Lambda 650 spectrometer is used in this thesis. It has a halogen lamp as the radiation source and a photodiode or a CCD as the detector. Monochromators filter the light so that only a single wavelength reaches the sensor after passing through the sample. The light beam is divided into two equal intensity beams by a half mirror into a sample beam and a reference beam, respectively, and are made to pass through their respective cuvette (quartz), as in Fig. 2.1. The range of this spectrometer is 400-4000 nm.

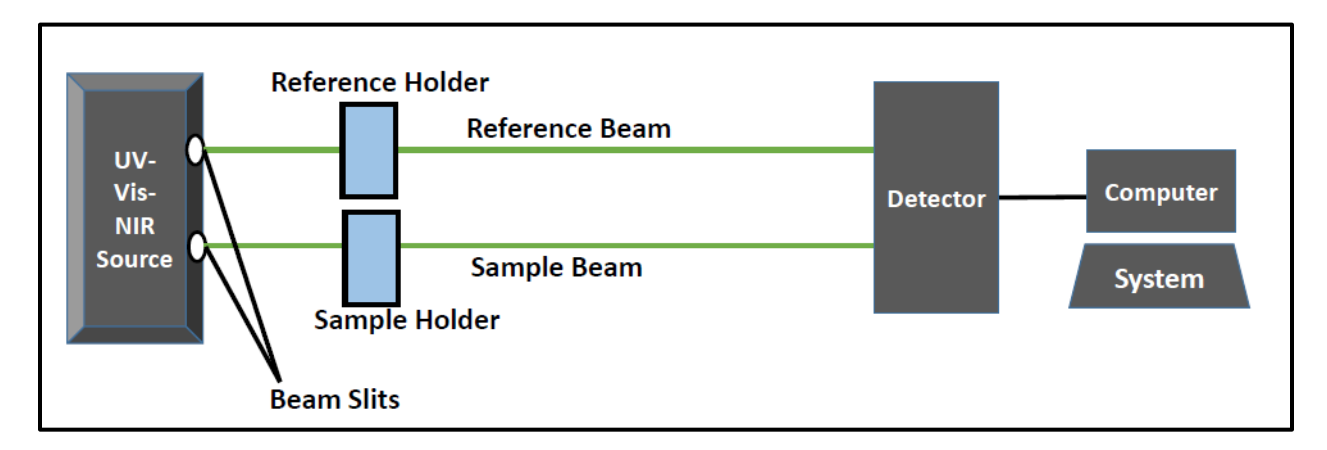


Figure 2. 1 Shows the UV-Vis-NIR Spectrometer

• FTIR Spectrometer:

FTIR or Fourier Transform Infra-Red spectroscopy uses an infra-red light source to provide a sample's absorption spectra. It works on the principle of Michelson's interferometer. When I.R. radiation is incident on materials under study, it absorbs the radiation at a wavelength corresponding to the molecular vibrational frequency. It transmits the rest, thereby providing a fingerprint absorption spectrum. Since all materials are a unique combination of particles, no two samples can produce the same infrared spectrum. Hence, it can be used as an identifying tool for different types of materials. Besides, the intensity of the FTIR absorption peak corresponds to the concentration of the material present. Fig.2.2 gives a schematic diagram of a usual FTIR spectrometer.

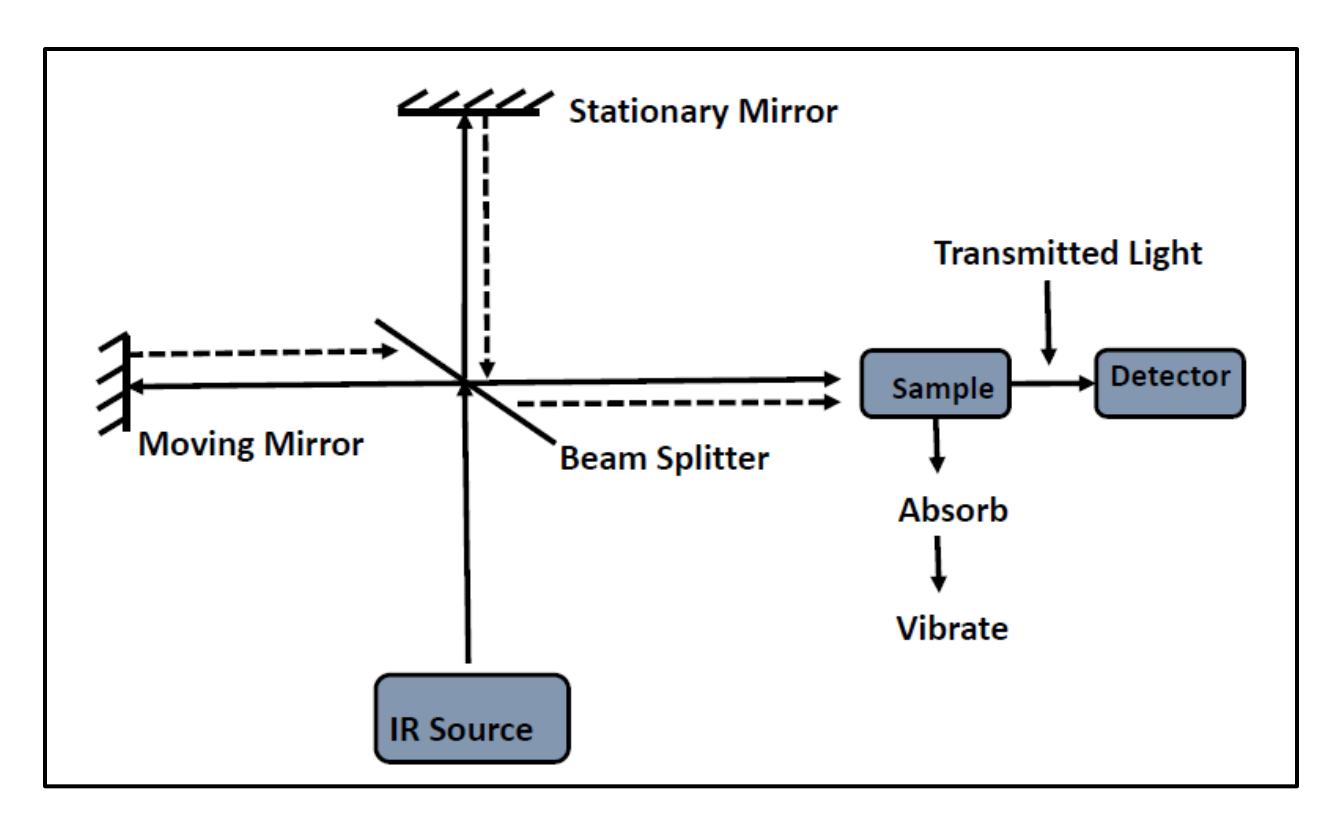


Figure 2. 2 Shows the schematic diagram of FTIR Spectrometer

This spectrometer consists of a beam splitter (KBr crystal in PerkinElmer I.R. spectrometer, which we have used) that splits the incoming infrared beam into two optical beams. One beam reflects off a flat mirror (M_s), fixed in place and the other beam reflects off of a flat mirror (M_m), which is allowed to move a very short distance away from the beam splitter. The two rays recombine and meet again at the beam splitter. Since the distance traveled by one beam is fixed and continuously changing for the other, the signal that exits the interferometer results from their interference.

The resulting signal is called an interferogram, a plot of the intensity at each frequency that provides the user with desired spectral information.

• Raman Spectrometer:

Raman based spectroscopy is known for its simple, quick, and non-destructive identification of molecules present in all phases of matter such as solid, liquid, or gases, making it one of the most versatile spectroscopic techniques. Due to different structural arrangements of various materials, Raman spectroscopy provides distinct spectra leading to unknown substances' compositions, making this technique ideal for qualitative analysis of materials, fig.2.3.

When a material is irradiated with a monochromatic laser, light from the illuminated spot is collected with a set of light collection optics and is sent through the spectrometer to obtain its spectrum. Instruments such as notch filters, tunable filters, laser stop apertures, etc. are used to reduce Rayleigh scattering and obtain high-quality Raman spectra. Nowadays, Raman spectroscopy has become even more accurate due to advancements in laser and computer technology.

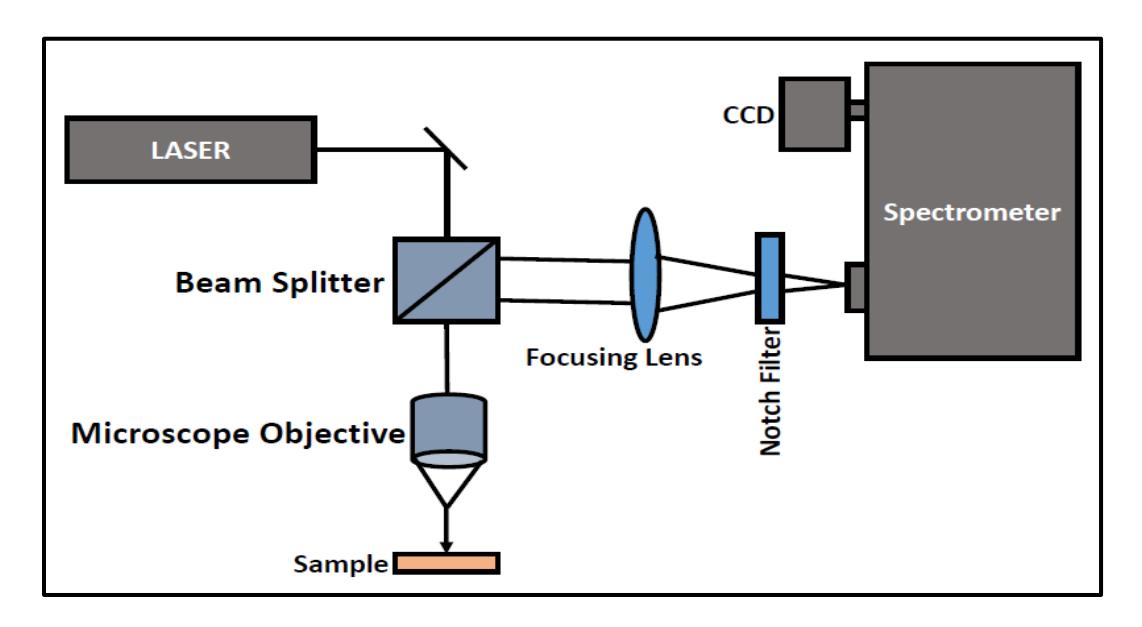


Figure 2. 3 Shows the schematic diagram of a Raman Spectrometer

2.3 Time-Dependent Spectroscopic Techniques:

Photoacoustic Spectroscopy:

• The photoacoustic spectroscopy technique:

The Photoacoustic effect is based on the principle of local heating of samples when subjected to a source of light. The heat generated is absorbed by the sample, causing a thermal expansion, which creates a pressure wave. This wave travels through the sample in compressions and rarefactions, giving rise to a sound wave at the same rate. We generally use either a continuous modulated beam or a pulsed laser beam for the excitation of the sample. FFT is used for converting the time-domain signal into a frequency domain resulting in a broad spectrum of acoustic frequencies. The laser source (Nd: YAG SpitLight), a four-level laser, is used along with a microphone (BSW, China), preamplifier, oscillator, and a computer system, as shown in fig. 2.4.

A well designed photoacoustic cell allows excitation of all types of cavity modes for the incident laser energy. In the P.A. technique, the Photoacoustic cell serves as a holder for the sample and the microphone used to detect the generated P.A. signals. According to the operation mode, the P.A. cell is divided into resonant and non-resonant. In the case of a non-resonant cell, the geometrical cavity does not match with the acoustic wavelength. However, modulation frequency of matches with at least one of the Eigenmodes of the cavity in case of a resonant cell. As a result, the cell's quality factor becomes high, and the amplitude of the excited resonance mode is amplified. It also possesses a high-quality factor that allows trace-level detection of high energy materials like RDX, HMX, TNT, and CL 20.

• The Experimental Arrangement:

Figure 2 provides the schematic diagram of the experimental setup of Time-domain Photoacoustic spectroscopy (PAS). The solid photoacoustic cell is an aluminum cubic shaped $(5\times5\times6\text{ cm}^3)$ cell containing the sample cavity. A Q-switched Nd: YAG laser of wavelength 532 nm (in the visible range)

was used as the source to excite the materials for analysis using this spectroscopic tool. The specifications of the laser system used as the source are given in Table 2.1.

Table 2. 1 The Specifications of the Laser System

Physical Parameter	Corresponding Value		
Model of the Laser (Four-level)	Spitlight 1200 INNOLAS Nd: YAG		
Energy Output (Maximum)	2000 mJ		
Available Wavelength(s)	1064/532/355/266 nm		
Diameter of the beam	6.5 mm		
Pulse width	7 ns		
Repetation Rate	10 Hz/20Hz		
Operating Temperature	15-35°C		
Set Operating Temperature	25°C		

We recorded the PA signal using a pre-polarized microphone, housed in a Teflon jacket and placed at a distance of 1.0 cm from the sample cavity. All the samples used for analysis were adjusted in the form of a circular disk with a uniform thickness and a diameter of 2mm, equivalent to laser spot size. The distance between the center of the sample to the detector (microphone) was 2.2 cm. An aluminum plate with a one-inch diameter quartz window combined with a neoprene washer was used to cover the cavity before irradiating the laser source sample. The obtained pre-amplified PA signal is fed to the digital storage oscilloscope (Tektronix, 200 MHz) to record the time domain signal which is later converted into FFT spectra using an indigenously developed data acquisition program in LabView software. Before conducting the experiment, the PA cell must be optimised for better performance. For this purpose, we have used graphite powder as it has excellent absorption through the entire wavelength range. The cell used in this experiment is a non-resonance photoacoustic cell.

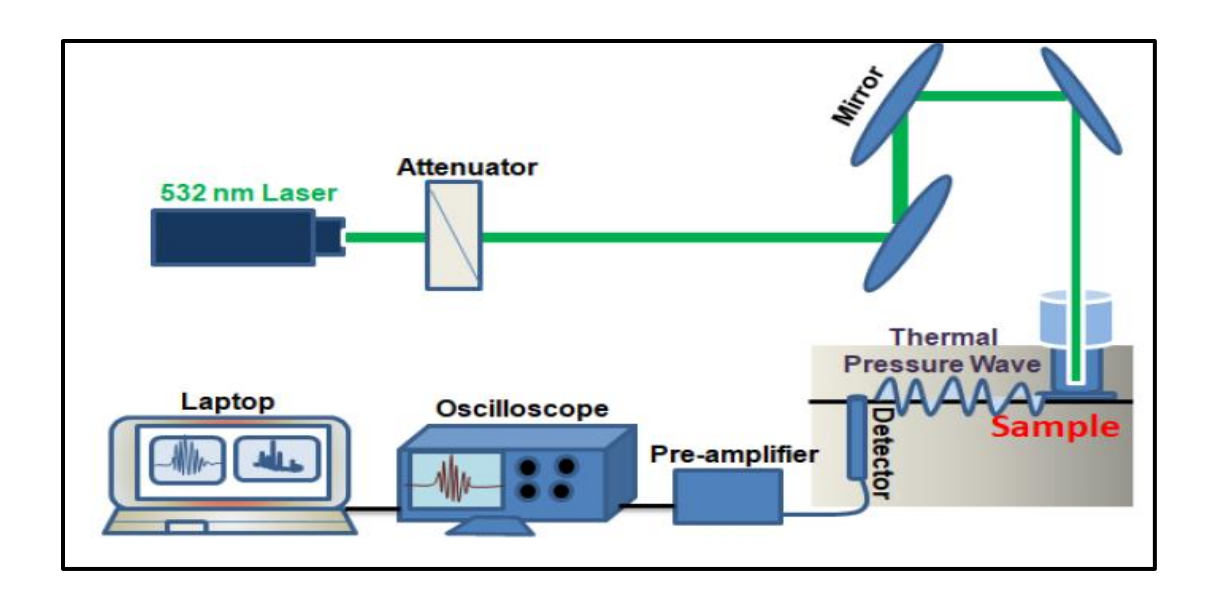


Figure 2. 4 Experimental setup for Photoacoustic Spectroscopy

• Terahertz Spectroscopy:

The Terahertz (THz) frequency range is observed between the EM spectra's microwave and infrared regions. Instrumental techniques such as XRD, SEM, EDX, and AFM, etc., give an ample amount of information about various materials. Still, molecular vibrations, details of the lattice or polymer structure, crystal Orientation, and low-energy molecular transitions can only be studied when the materials are subjected to ultrafast laser pulses. Despite having a broad range of applications in homeland security, imaging, explosive detection, and the health-care industry, this region is still less explored due to various reasons; some of them being low availability of stable femtosecond lasers, unavailability of appropriate THz sources and detectors, their high cost and maintenance, etc. However, over the past few years, research in THz spectroscopy has seen tremendous growth. Generation and detection of THz using non-linear crystals like CdTe, ZnGeP₂, etc. have become popular. Detection techniques such as EO (Electro-Optic) sampling technique and PC (Photoconductive) sampling technique have helped immensely develop this spectroscopic technique.

In this thesis, we have generated THz frequency waves using a nonlinear crystal, CdTe, and detected it through PC sampling by using photoconductive antennas. CdTe has various properties apart from high electro-optic and nonlinear coefficients, which makes it a suitable candidate for the generation of THz. Some of them are:

- Higher Ionicity & Stronger Bonds = Higher Melting Temperature
- Less Energy Lost = More Efficient & Potential For Lower Cost applications
- Higher Breakdown Voltage = High Power & Frequency Applications
- Higher Doping Concentration = Thinner device layers
- Higher Electron Mobility = Faster Operation

Apart from the generation of terahertz waves, we have also studied the dependence of emitted THz amplitude with respect to incident laser wavelengths. Besides, we examined the effect of angle of incidence of laser pulses on generated THz radiation. The linear/nonlinear transmission and absorption

properties of CdTe crystal were also explored. Further details about this technique can be found in chapter 5.

The coherent chameleon ultra-II femtosecond laser (~ 140 fs at 80 MHz repetition rate) was used as the source in our experiment. Some of the physical parameters of the laser system are comprised in Table 2.2.

Table 2. 2 Physical parameters of the Laser System

Laser	Variable Chameleon	Oscillator	Femtosecond
Parameters	Oscillator	(Micra-10)	(Legend)
Max Energy Output	4 W/46 nJ	700 mW/8.75 nJ	2.5 W/2.5 mJ
Diameter of beam	1.2mm	1.25mm	8mm
Pulse Duration of the laser	140fs	15fs	40fs
Repetition Rate Observed	80MHz	80MHz	1kHz
Polarization	Horizontal	Horizontal	Horizontal

The laser source is tunable between 680 - 1080 nm wavelengths, with 800 nm being the central wavelength. A variable attenuator is used in the experimental setup, which helps us to regulate the power of the incident laser pulse, which strikes the crystal that works as the source for THz radiation. The crystal was placed in a rotating mount (WP-840-0186) in order to vary the azimuthal angle of the crystal. The generated radiation can be maximized by azimuthally rotating the crystal and polarization of laser pulse. The pump and probe powers used for this technique are 300 and 75 mW, respectively. For detection, we have used the Photoconductive sampling technique using a photoconductive antenna (gap ~ 5 µm, length ~ 20 µm). Further details of the experimental setup along with optics arrangement are provided in Appendix B.

2.4 Conclusion:

In this chapter, we have presented various experimental techniques used to carry out different experiments discussed in this thesis. It discusses the working principles and the experimental arrangements of time-independent methods such as UV-Vis-NIR, FTIR, and Raman Spectroscopy, along with a brief description of time-dependent spectroscopic techniques such as photoacoustic and terahertz spectroscopy.

References:

- 1. J. S. Caygill, F. Davis, S. P. J Higson, Current trends in explosive detection techniques, Talanta. 88 14-29 (2012)
- 2. M. López-López, C. García-Ruiz, Infrared and Raman spectroscopy techniques applied to identification of explosives, Trends Analyt. Chem. 54 36-44 (2014)
- 3. S. Elbasuney, A. F. El-Sherif, Complete spectroscopic picture of concealed explosives: laser-induced Raman versus infrared, Trends Analyt. Chem. 85 34-41 (2016)
- 4. G. Mogilevsky, L. Borland, M. Brickhouse, A. W. Fountain III, Raman Spectroscopy for Homeland Security Applications, Hindawi Publishing Corporation International Journal of Spectroscopy. 808079 1-12 (2012)
- 5. M. A. Bañares, G. Mestl, Structural characterization of operating catalysts by Raman spectroscopy, Adv.Catal. 52 43-128 (2009)
- 6. I. R. Lewis, N. W. Daniel, P. R. Griffiths, Interpretation of Raman spectra of nitrocontaining explosive materials. Part I: Group frequency and structural class membership, Appl. Spectrosc. 51 1854-1867 (1997)
- 7. Finot, Eric, Thibault Brulé, Padmnabh Rai, Aurélien Griffart, Alexandre Bouhélier, and Thomas Thundat, Raman and photothermal spectroscopies for explosive detection, In Microand Nanotechnology Sensors, Systems, and Applications V, International Society for Optics and Photonics. 8725 872528 (2013)
- 8. K. S. Rao, A. K. Chaudhary, F. Yehya. Investigation of solid carbon blacks using pulsed photoacoustic and double resonant Raman spectroscopy for the identification of trinitrotoluene, Sens. Actuators B Chem. 231 830-836 (2016)
- 9. Y. Liu, R. Perkins, Y. Liu, N. Tzeng, Normal mode and experimental analysis of TNT Raman spectrum, Struct .Mol .J. 1133 217-225 (2017)
- 10. S. Gulia, K. K. Gulati, V. Gambhir, R. Sharma, M. N. Reddy, Trace detection of explosive and their derivatives in stand-off mode using time gated Raman spectroscopy, Vib. Spectrosc. 87 207-214 (2016)
- 11. M. Marshall, J. C. Oxley, Aspects of Explosives Detection, 1st Edition, Maurice Marshall, Jimmie Oxley, Oxford U.K., (2008)

- 12. Forensic Investigation of Explosions, 2nd Edition, A. Beveridge, Ed., Taylor & Francis Ltd, CRC Press, Boca Raton FL, (2012)
- 13. J. S. Caygill, F. Davis, Higson, S. P. J. Current trends in explosive detection techniques. Talanta 88, 14-29 (2012)
- 14. E. K. Jenkins, Effects of oral administration of metronidazole and doxycyline on olfactoary capabilities of explosives detection dogs. Am. J. Vet. Res. 77, 906-912 (2016)
- 15. J. I. Steinfeld, J.Wormhoudt, Explosives detection: A Challenge for Physical Chemistry. Annu. Rev. Phys. Chem. 49, 203–232 (1998)
- 16. T. M. Swager, Sensor Technologies Empowered by Materials and Molecular Innovations. Angew. Chem. Int. Ed. 57, 4248 –4257 (2018)
- 17. S. W. Thomas, G. D. Joly, T. M. Swager, Chemical sensors based on amplifying fluorescent conjugated polymers. Chem Rev. 107, 1339-1386 (2007)
- 18. T. L. Andrew, T. M. Swager, A Fluorescence Turn-On Mechanism to Detect High Explosives RDX and PETN. J. Am. Chem. Soc. 129, 7254-7255 (2007)
- 19. D. Gopalakrishnan, W. R. Direct Detection of RDX Vapor Using a Conjugated Polymer Network. J. Am. Chem. Soc. 135, 8357–8362 (2013)
- 20. XS Wang, L. Li, DQ Yuan, Fast, highly selective and sensitive anionic metal-organic framework with nitrogen-rich sites fluorescent chemosensor for nitro explosives detection. J. Hazard. Mater. 344, 283-290 (2018)
- 21. A. K. Chaudhary, G. C. Bhar, Low-limit photoacoustic detection of solid RDX and TNT explosives with Carbobdioxide Laser, J. Appl. Spectrosc. 73, 123-129 (2006)
- 22. K. S. Rao, A. K. Chaudhary, Investigation of solid carbon blacks using pulsed photoacoustic and double resonant Raman Spectroscopy for identification of trinitrotoluene Sens. And Act. B: chemical 231, 830-836 (2016)
- 23. D. F. Plusquellic, K. Siegrist, E. J. Heilweil and O. Esenturk, Applications of Terahertz spectroscopy in biosystems, Chem Phys Chem, 8, 2412-2431 (2007)

- 24. S. Dexheimer, Terahertz Spectroscopy: Principles and Applications in Terahertz Spectroscopy: Principles and Applications, Taylor & Francis, 360 (2007)
- 25. M. C. Kemp, P. F. Taday, B. E. Cole, J. Cluff, A. J. Fitzgerald, and W. R. Tribe, Security applications of terahertz technology, Proc. SPIE, 5070, 44–52, (2003)
- 26. M. Venkatesh, K.S. Rao, T.S. Abhilash, S.P. Tewari, A.K. Chaudhary, Optical characterization of GaAs photoconductive antennas for efficient generation and detection of Terahertz radiation, Optical Materials 36, 596–601 (2014)
- 27. M. D. King, W. D. Buchanan, and T. M. Korter, Understanding the Terahertz Spectra of Crystalline Pharmaceuticals: Terahertz Spectroscopy and SolidState Density Functional Theory Study of (S)-(+)-Ibuprofen and (R.S.)- Ibuprofen, J. Pharm. Sci., 100(3), 1116–1129, (2011)
- 28. M. He, A. K. Azad, S. Ye, and W. Zhang, Far-infrared signature of animal tissues characterized by terahertz time-domain spectroscopy, Opt. Commun., 259(1), 389–392, (2006)

Chapter: 3

Use of PEDOT Polymer Optode as a Sensor for lowlevel detection of solid explosives using Time domain Photoacoustic Spectroscopy

3.1 Abstract

This chapter has examined the role of a conducting polymer, Poly (3,4-ethylene dioxythiophene), commonly known as PEDOT, as an optode sensor for high energy materials (explosives). Since the photoacoustic spectrum behaves as a fingerprint spectrum of different materials, its analysis proves differences between various substances. The mixture of PEDOT and the explosives were irradiated with 7 ns pulses of 532 nm wavelength obtained from Q-switched Nd: YAG laser at 10 Hz repetition rate. The incident laser radiation initiates the transfer of electrons from the nitro group of the explosives to the oxidized PEDOT in excitons. This charge-transfer mechanism is explained in detail in this chapter. The transition of electrons from the excited state to the ground state is followed by a radiative and non-radiative decay process responsible for generating thermal pressure waves. These waves are measured in terms of acoustic waves in a specially designed solid PA Cell. The analysis of pure explosives such as RDX, HMX, TNT, CL20, and TEX, along with their mixture with pristine PEDOT, shows an enhancement in the mixture's peaks. The enhanced PA signal's strength for these explosives was of the order of 72.14, 3.24,3.55, 5.86, and 40.95 times, respectively, at 4.0 kHz frequency.

We have also investigated the samples' physical and chemical properties, such as the absorption coefficient and refractive index. We have further extended the study of polymers to an analysis of natural rubber polymer where it describes the effect of reinforcing agents like carbon fillers in different proportions in the matrix of natural rubber(NR)/chloro butyl rubber (CIIR) blends in terms of absorption, thermal diffusion and penetration depth using time-domain pulsed photoacoustic technique

3.2 Introduction:

In this chapter, we have used the pulsed photoacoustic spectroscopic(PAS) technique as a tool to detect high energy materials, also known as explosives, such as RDX, HMX, TNT, CL20, and TEX using a conducting conjugated polymer, PEDOT, as an optode sensor. These explosives' low-volatility and weak electron-withdrawing capabilities have proved to be a primary international concern in homeland security against terrorist activities, forensic science research, and a significant health hazard [1-3]. Besides, homeland security has a high demand for portable, reliable, and easy availability and affordability of detection systems [4]. Spectroscopic techniques, including metal detectors, gas chromatography coupled with mass spectrometry, SERS, electron capture detection, X-ray imaging, ion mobility spectroscopy (IMS), etc. are used for the detection and quantification of various explosive molecules. Unfortunately, a metal detector, which is the most commonly used device, is prone to false results. Even trained sniffer dogs are useful, but they demand training and are difficult to maintain [5]. Also, dogs detect explosives by inhaling their vapors, which can have adverse health effects in the long run. The analytical techniques used so far are associated with certain limitations such as cost, requires maintenance and trained operators, lack of portability, demands pre-concentration strategy, frequent calibrations, etc. Thus, we must look for portable, inexpensive, and reliable explosive sensors for identifying specific explosives.

Various research groups across the globe are trying to develop sensors for different explosives. For example, Swager and co-worker [6-8] synthesized various conjugated fluorescence molecules for the detection of explosives; Dichtel et al. [9] demonstrated the detection of RDX vapor using a conjugated polymer network of tris(phenylene)vinylene. Metal-organic frameworks (MOFs) were used as selective and sensitive detectors for nitro explosives [10,11]. The organic/inorganic conjugated polymers used by various researchers to detect explosives were mainly fluorescence quenching methods, which is a radiative decay process. Also, one of the significant shortcomings was the lack of explosive detection techniques in the visible region. This chapter has used visible 532 nm wavelength light obtained from a Q-switched Nd: YAG laser and incorporated it with a Photoacoustic spectroscopic tool, which is a nonradiative and non-destructive spectroscopic technique. We have chosen a PEDOT conjugate polymer as a sensor for explosives, keeping in mind that explosives like RDX, TNT, HMX, and other plastic explosives have no absorption in the visible region due to their high bandgap. However, their mixture with PEDOT shows excellent absorption in the ultra-violet to the NIR region. Our group, Chaudhary et al., has recorded rotational lines of TNT based on the PA technique using tunable continuous-wave CO₂ laser [12]. The same group has also reported Graphite as a sensing medium for TNT [13].

Most of the available scientific reports on optical detection of explosives are based on photoluminescence (PL) or fluorescence techniques using polymers as a matrix, using the radiative decay process. However, to date, detecting the plastic explosives in the visible region has not been extensively explored. From Fig.3.1, we see that before radiative decay, there exists another interesting process called nonradiative decay that occurs at the intra-band energy level of the excited state of the analyte and was known as early as before the PL/fluorescence. This provides valuable information about the transition of electrons in the visible region.

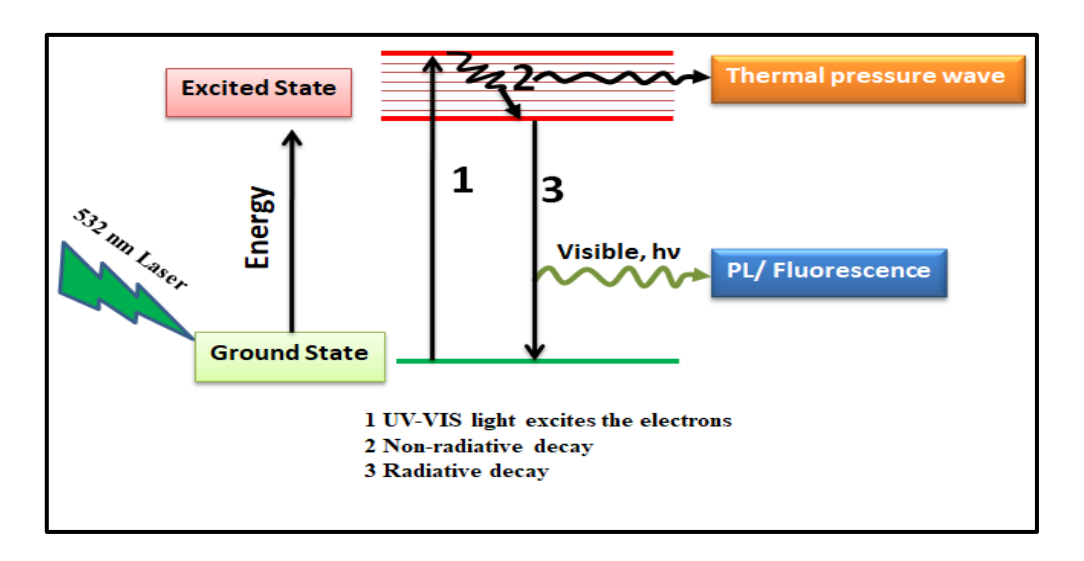


Figure 3. 1 Schematic representation of radiative and nonradiative decay.

This inspired us to use the nonradiative decay process to detect explosive materials by using PEDOT conjugated polymer. We have also been able to enhance the PA signal amplitude by using PEDOT polymer in place of Graphite, as was discussed in [13], where it had been used to detect TNT and other explosives, such as RDX, HMX, CL20, and TEX as well. We have used the phenomenon of charge-transfer mechanism (explained later in the chapter), which takes place from the HOMO of the explosive molecules to the LUMO of the PEDOT's polymeric chain, which forms the basis of their detection. The Lewis-acidity of Sulphur due to the positive charge density in the conjugate polymer PEDOT and the Lewis-base donors due to nitro-groups in the high energy molecules provides a donor-acceptor interaction which facilitates the electron/charge transfer, leading to the detection of the explosives.

PEDOT has various properties that facilitate this phenomenon. Along with being a conducting conjugated polymer, it carries a positive charge upon doping and has a small bandgap, high conductivity, and increased stability. The small bandgap structure allows it to have various applications like LEDs, capacitors, solar cells, etc. This polymer proves to be a good conductor because of its conducting mechanism and its relation to the doping process. PEDOT is in its neutral state, possesses the delocalized electrons along the chain, and by doping, we either remove or add an Electron. These two processes create cations and anions on the polymer called polarons, and a pair of polarons is known as a bipolaron. The movement of the bipolarons as a couple on the polymer chain is responsible for PEDOT's good

conductivity, as shown in Fig. 2.2. This continuous chain consists of sp² hybridized carbon, which leads to the formation of n-bonds due to which they conduct.

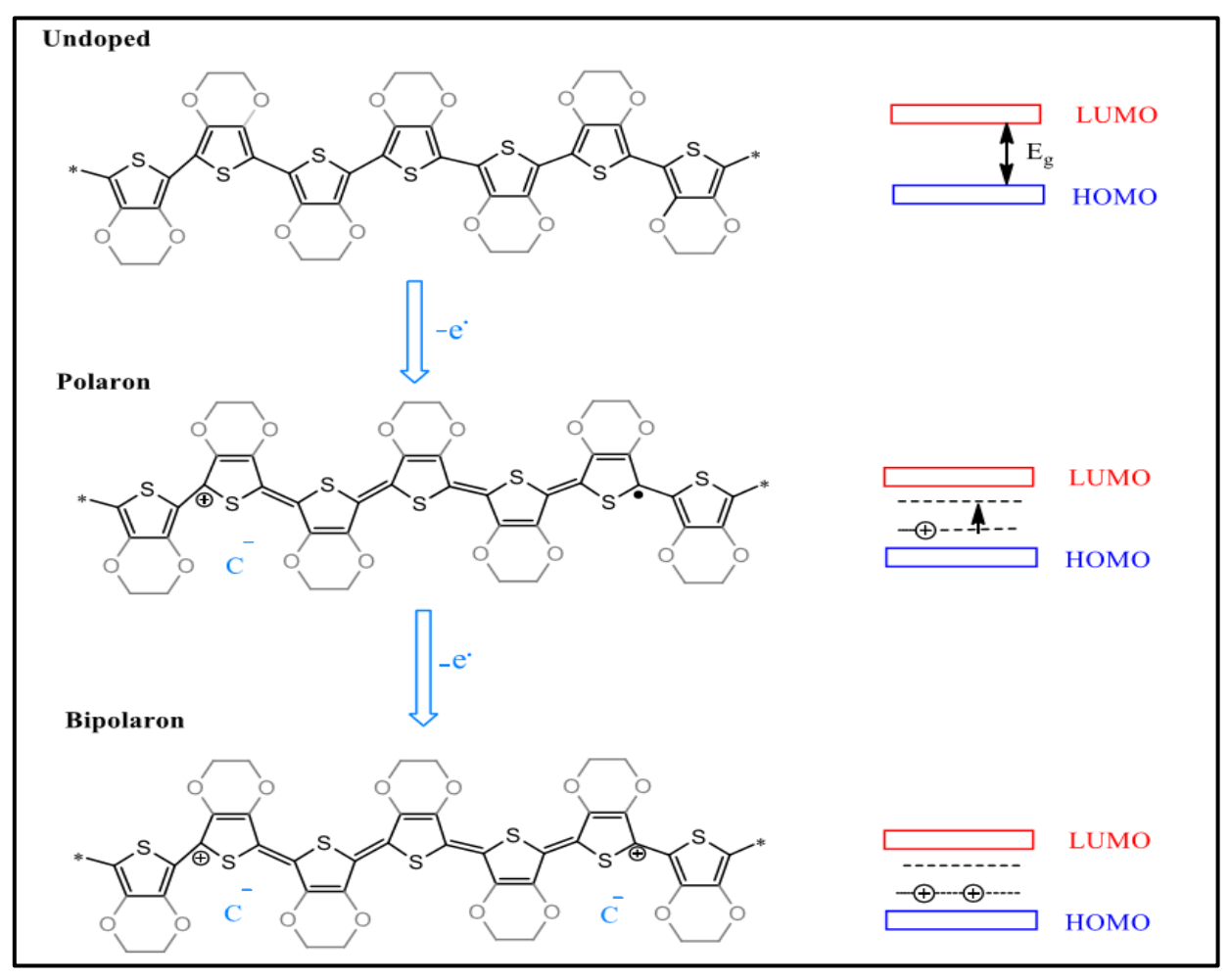


Figure 3. 2 This figure represents the formation of polaron and bipolaron on the polymeric chain of PEDOT responsible for its conduction

The present chapter is further divided into two subsections: Section 1 describes the use of PEDOT as an optode or a sensing medium for explosives, and section 2, also discuss the use of the time domain photoacoustic spectroscopic technique to study the quality and strength of rubber polymers with different types of inorganic and organic fillers. These fillers are added in different proportionate in the matrix of natural rubber (NR) /chloro butyl rubber (CIIR) blends in terms of their physical properties such as absorption, thermal diffusion, and penetration depth.

Section: 1

Detection of High Energy Materials (HEMs) Using PEDOT Optode as a Sensing Medium in Pulsed Photoacoustic Spectroscopy

3.3 Introduction to High Energy Materials:

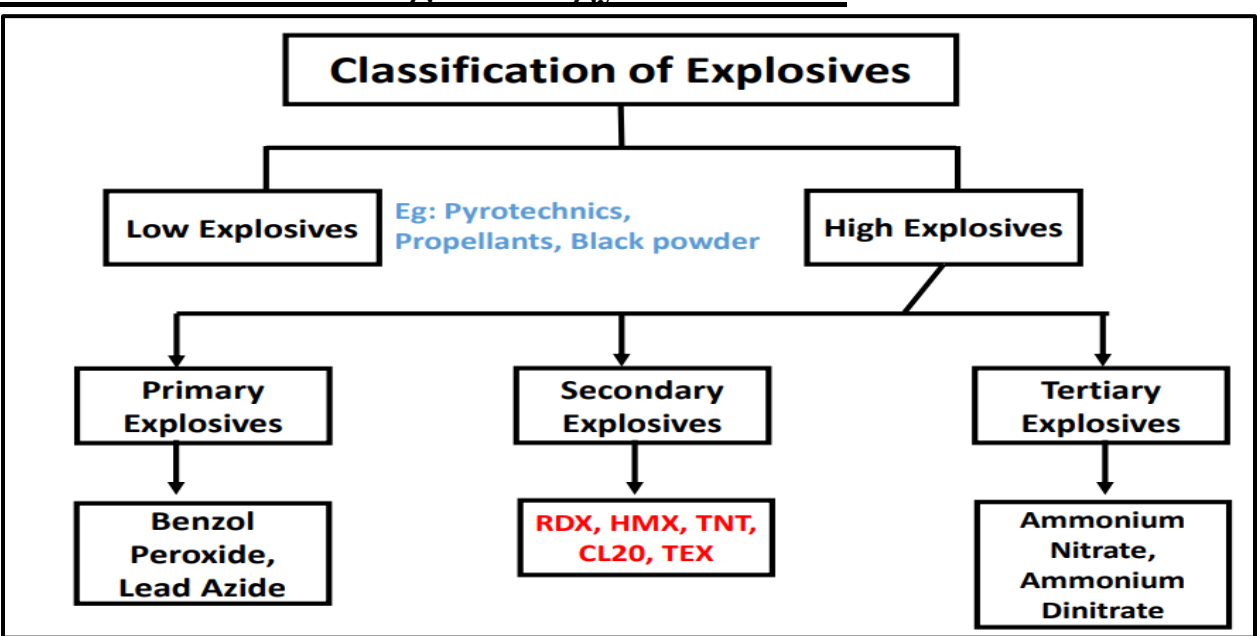


Figure 3. 3 This figure schematically represents the classification of High Energy Materials

The information and various details about the nature, physical, and chemical properties of different explosives is provided in Appendix C, provided at the end of the thesis. In this thesis, we have used the PAS technique to detect solid explosives, divided into three categories based on their chemical structure and the nitro (-NO2) group's placement. These are; aliphatic nitrate ester (R-O-NO2), nitro-aromatic (Ar-NO2), and cycloaliphatic nitramine (>N-NO2) groups. Further details are provided in Table 1 in Appendix C.

Detection of explosives can be made more accessible if we have all the information about their characteristic constituent particles. Traces of explosives, for example, few micrograms, can easily be transferred through hands and touched objects. Most of the detection technologies available today are dependent on the property of the transmission of explosives in the ultra-violet to the visible region. Raman spectroscopy has also emerged as a pioneering technique for the detection of these molecules. This technique is discussed in detail in the next chapter, chapter 4. Raman spectroscopy is an analytical tool that provides molecule-specific information in great detail. It has been in use as a standard analytical tool for identifying chemical substances for many years. Carter et al. studied the effects of the laser power on

explosive samples. They concluded that the signal's intensity increased linearly with laser power density for most of the materials analyzed.

• Experimental Arrangement:

The experimental setup for analysis of these materials is shown in Fig. 4, of chapter 2. Before recording the data with the help of PA, spectroscopy was performed in the solid-state by irradiating the samples with laser energy corresponding to 532 nm wavelength at 10 Hz repetition rate in the visible region of the EM Spectra; the samples that were used for the experiment were prepared. Solid explosive samples such as RDX, TNT, HMX, TEX, and CL20, respectively, were physically crushed into a fine powder using mortar-pestle. The grain size and other physical parameters were noted (Table 3.1), and the conducting conjugate PEDOT polymer was synthesized in the laboratory. A brief introduction to PEDOT polymer and its synthesis is discussed below.

Table 3. 1 represents the image, size, and density of the samples considered for the study

Sample Name	Sample Image	Size of the grain	Density (g/cm ³)
PEDOT		200 μm	1.331
RDX		100 μm	1.76

HMX		120 μm	1.91
TNT	10 × 10 × 10 × 10 × 10 × 10 × 10 × 10 ×	50 μm	1.654
PEDOT+RDX	-	60 μm	1.538
PEDOT+HMX	-	110 μm	0.157
PEDOT+TNT		130 μm	1.428

• Introduction to PEDOT Polymer and its synthesis:

Electrically conducting polymers have found broad applications in electronics and bioelectronics, among other applications in chemistry and spectroscopic studies. A large number of conducting polymers are available, both commercially as well as those synthesized in laboratories. Poly(3,4-ethylenedioxythiophene) or commonly known as PEDOT, is one such conducting polymer which is available commercially under the name of Poly (styrene sulfonate) or (PEDOT: PSS) as well as it can be easily synthesized. PEDOT has high chemical stability, high conductivity, and good optical properties. It is also used in light-emitting diodes (OLEDs) and various other devices. Recently, it has also found its application as useful biosensors. Fig 3.4 shows the structure of the polymer. It is the most versatile conducting polymer used for different practical applications as it possesses many unique properties described above.

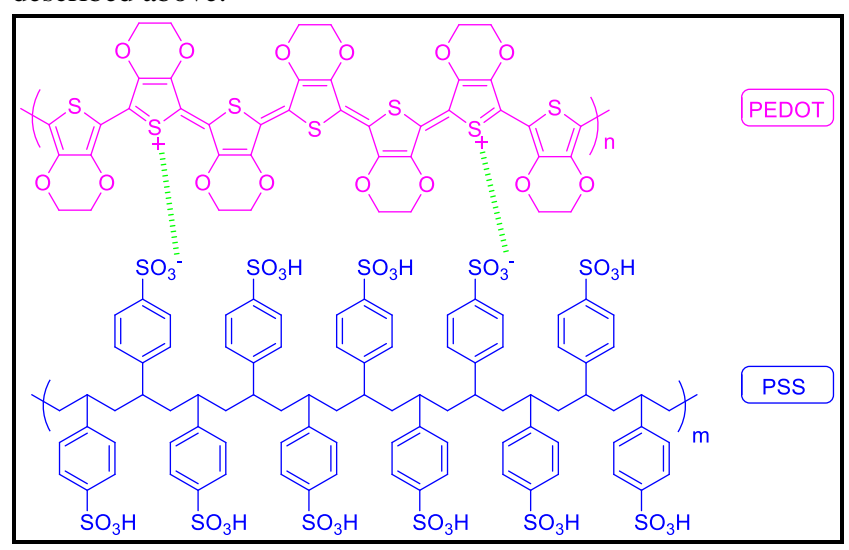
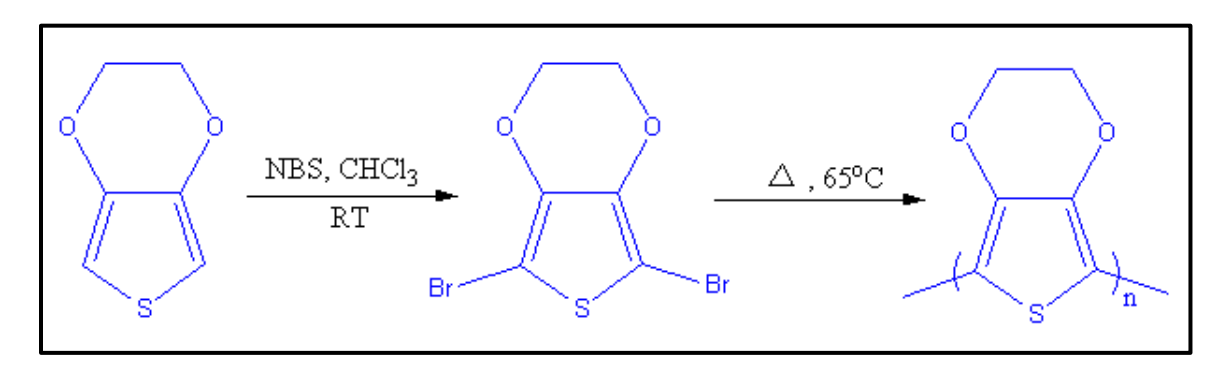


Figure 3. 4 Schematic representation of negative charge on the oxygen atom and positive charge on PEDOT in PEDOT: PSS

• Synthesis of PEDOT:

PEDOT is synthesized by adopting solid-state polymerization, and the detailed synthesizing method is discussed in scheme 1 as shown in the figure. The methodology of its synthesis has been adopted as provided in [14]. The final product is an insoluble deep blue solid, for which the molecular compositions and structure are determined using elemental analysis. This procedure suggests that, PEDOT is in its oxidized state in which each bi-polaronic unit is repeated after every five monomers (3,4-ethylene dioxythiophene (EDOT)) units, as shown in Fig. 2. PEDOT in the oxidized state shows an absorption in the near-infrared (IR) region, whereas its reduced state absorbs in the visible region due to transition of the electrons in $\pi \rightarrow \pi^*$ state. To further confirm the oxidized state, PEDOT powder was dispersed in aqueous media using polystyrene sulfonate (PSS) to obtain PEDOT: PSS aqueous dispersion.



Scheme 1: Schematic representations for the synthesis of PEDOT.

The dark blue color of the PEDOT polymer shows its reduced state, which exhibits strong absorption. However, the doped PEDOT shift in the maximum absorption towards longer wavelengths (Fig. 3.5), which explains the near transparency in its oxidized state. UV-Visible absorption spectroscopy was performed on PEDOT: PSS aqueous dispersion and the results are represented in fig.3.5. PEDOT: PSS aqueous dispersion displayed maximum absorbance above 890 nm (figure 3.5(i)) which also indicates the presence of the bipolar state of the oxidized state of PEDOT. When a drop of hydrazine hydrate (a reducing agent) was added to the dilute the initial aqueous dispersion, the absorption maxima shifted at 600 nm (visible region), which is attributed to the π - π * electronic transition of reduced PEDOT. Hence, UV-visible absorbance spectroscopy further confirms that the synthesized PEDOT was in an oxidized state.

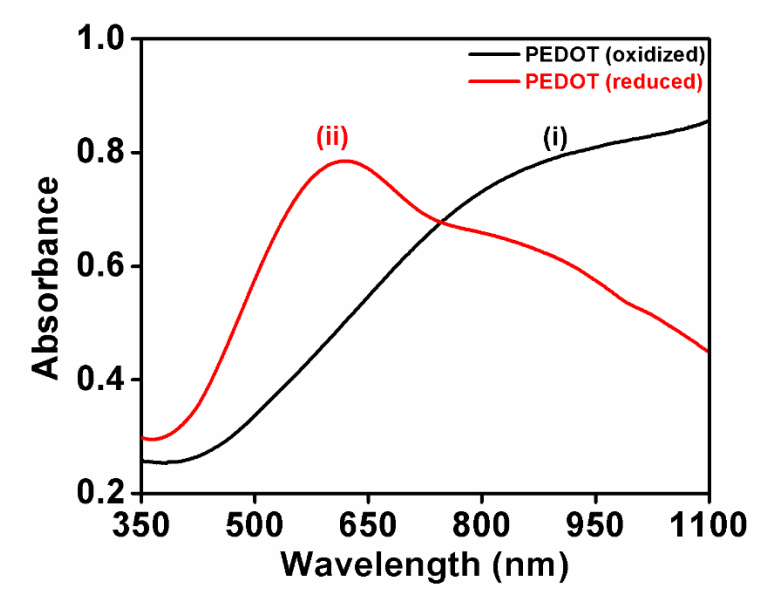


Figure 3. 5 UV-Vis spectra of (i) PEDOT: PSS, (ii) UV-Vis spectra of hydrazine hydrate treated PEDOT: PSS.

After the synthesis of PEDOT, the blue-black PEDOT powder was mixed uniformly with the explosive samples before performing the PA spectroscopy. The mixing was done physically using a mortar-pestle. There was no chemical treatment involved while preparing the samples. Pristine conjugated polymer (PEDOT), pristine explosives (RDX, TNT, HMX, TEX, and CL20) and PEDOT+ explosive mixtures (PEDOT+TNT, PEDOT+RDX, PEDOT+HMX, PEDOT+TEX, and PEDOT+CL20) are the samples

considered for study in this chapter. An equal amount of sample, in the ratio of 1:1, was taken while making the mixture of PEDOT and explosive, whereas 0.2mg of the pure explosive sample was taken while recording the data for pure explosive samples. The data was recorded for each of the samples at various incident laser energies; 0.5 mJ, 1 mJ, 1.5 mJ, 2 mJ, and 2.5 mJ, respectively, and the data acquisition time considered was 0.5 ms, 1.0 ms, 1.5 ms, and 2.5 ms, respectively.

3.4 Results and Discussion:

• The "Q" factor of the Photoacoustic cell

The quality factor 'Q' of the solid-state photoacoustic cell is estimated as the ratio of the energy stored in the PA cavity to the energy lost by the sample's molecules per cycle. This is expressed as:

$$Q = \frac{\omega}{\Delta \omega} \tag{1}$$

Here, ω is the central frequency, and $\Delta\omega$ represents the FWHM of the exciting acoustic modes. Fig. 3.6 shows the estimation of this factor where the data recorded at different incident energy using the 532 nm wavelength as the source has been fitted into a Lorentzian curve. The data acquisition time is kept constant at 5ms. 'Q' is directly proportional to ω of the acoustic mode, and therefore, high and sharp frequency acoustic modes of PA spectra result in a higher quality factor. Also, higher data acquisition values lead to a higher quality as it fills the gap between the two adjacent data points of PA spectra (i.e., provides low $\Delta\omega$). The quality factor is 18 in our case.

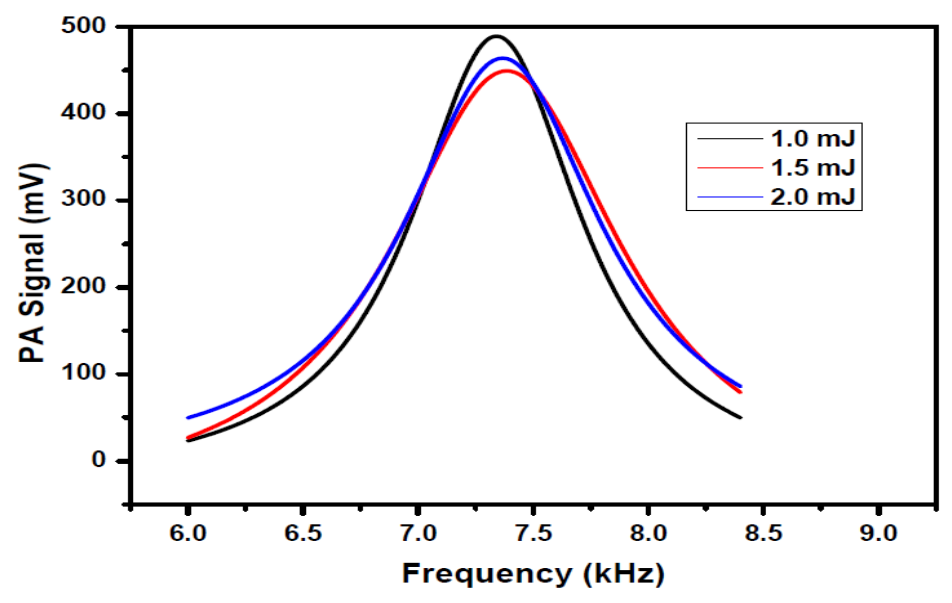


Figure 3. 6 "Q" factor Curves of the experimental photoacoustic cell

• PA Cell Responsivity:

We have estimated the solid-PA cell's responsivity at 10 kHz frequency mode using the same laser source. The variation in the incident energy vs. the photoacoustic signal was plotted for this estimation. Pure PEDOT has a cell responsivity of 7.5 mV/mJ, whereas explosive samples (High Energy Materials,

HEMs) such as TEX and CL20 show responsivity around 25 V/J. This concludes that when explosives are mixed with PEDOT, their cell responsivity is enhanced, as shown in Fig. 3.7.

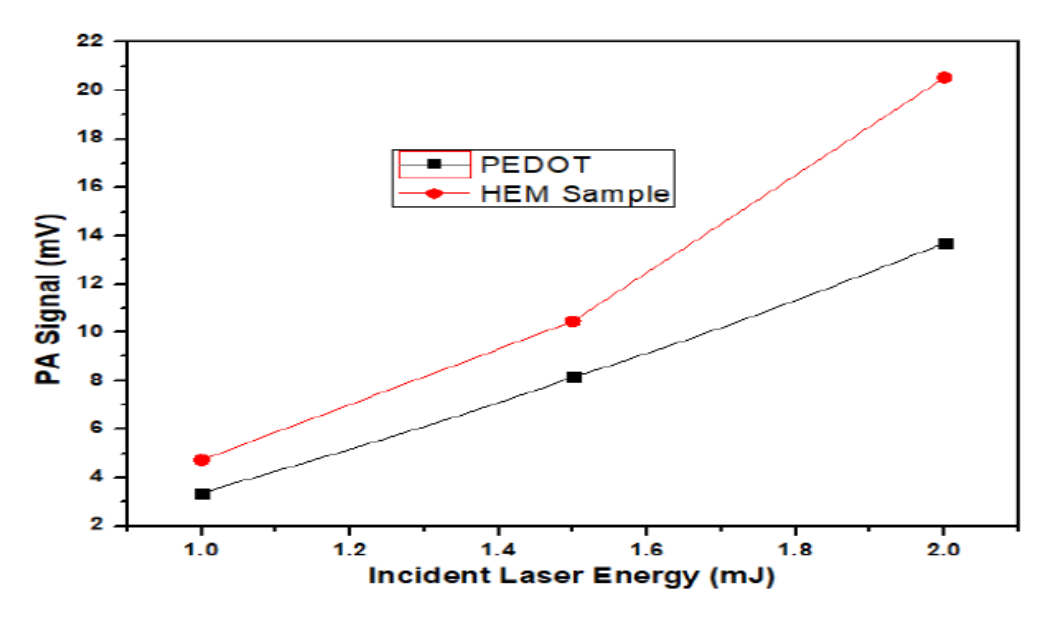
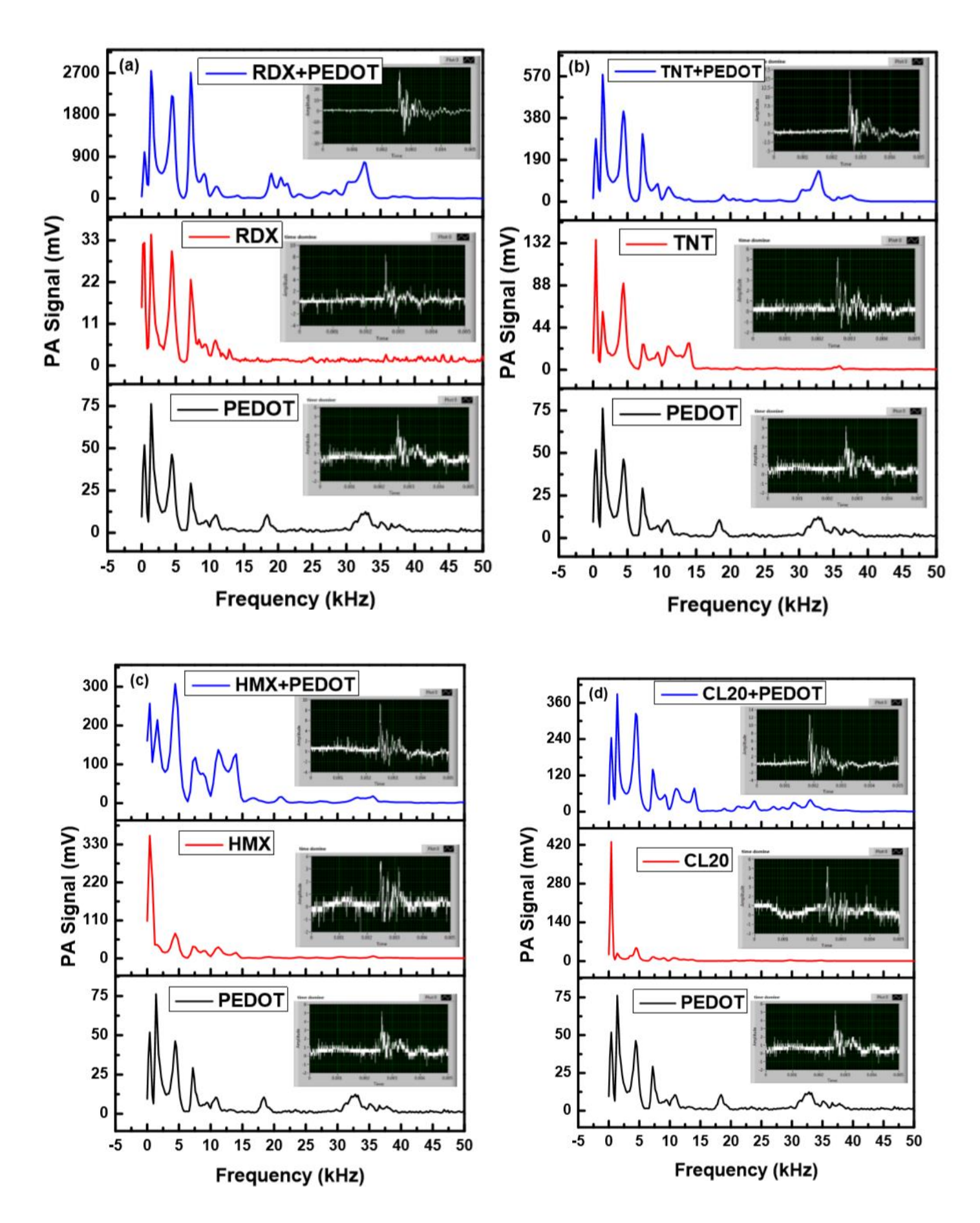


Figure 3. 7 This graph represents the photoacoustic cell responsivity.

• The PA signal Vs acoustic frequency:

Figure 3.8 represents the frequency domain spectra corresponding to 0.5 mJ laser energy and 0.5 ms data acquisition. It is observed that pristine PEDOT displays PA modes between 1.45 kHz and 32.8 kHz range, whereas primary explosives (RDX, TNT, HMX, TEX, and CL20) demonstrated PA modes between 1.45 kHz and 13.0 kHz range. The PA modes and the corresponding PA signal obtained for the samples are summarized in the related tables. Primary explosives (RDX, TNT, HMX, TEX, and CL20) don't show PA modes at 19.06 kHz and above, but their mixture with the conducting polymer PEDOT, demonstrate varying PA signals at these PA modes. Figure 8(a) presents the frequency domain spectra of PEDOT, RDX and PEDOT+RDX. It is observed that the PEDOT+RDX mixture possesses all the PA modes present in pristine PEDOT (1.45 kHz to 32.8 kHz) but with an enhanced PA signal. The enhancement factor of each prominent peak observed in the mixture of PEDOT+ explosives. The observed low response of oxidized PEDOT is due to low absorption in the visible region. Still, when it is mixed with the RDX and irradiated the laser energy corresponding to wavelength 532 nm, the electrons from the highest occupied molecular orbital (HOMO) of RDX is being transferred to the LUMO of the oxidized PEDOT. The weakly attached electron from lone pairs of electrons on the oxygen in the nitro-group of RDX transfers electrons to the PEDOT, thus, converting the oxidized PEDOT into reduced PEDOT.



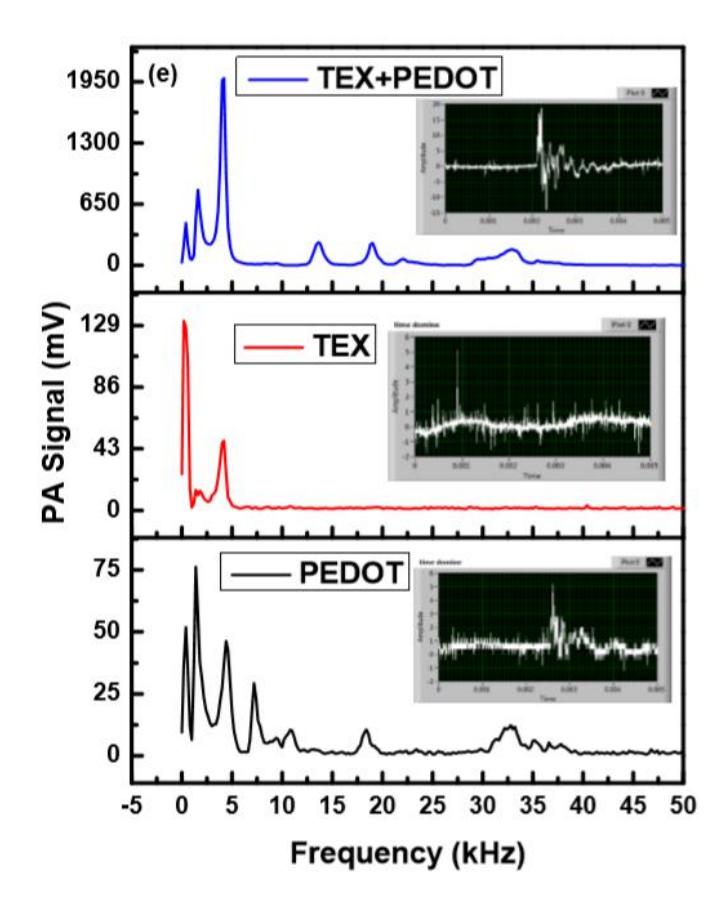


Figure 3. 8 Graphs of the various PA modes of frequency domain signal (a) PEDOT, RDX, and PEDOT+RDX; (b) PEDOT, TNT, and PEDOT+TNT; (c) PEDOT, HMX, and PEDOT+HMX; (d) PEDOT, CL20, and PEDOT+CL20; (e)) PEDOT, TEX, and PEDOT+TEX.

From fig. 3.8, it is observed that irradiating the PEDOT and the explosive mixtures with an incident laser energy results in enhancing the strength of the PA signal. PEDOT+TNT, PEDOT+HMX, PEDOT+CL20, and PEDOT+TEX mixtures displayed similar observations, but the PA signal enhancement was less as compared to PEDOT+RDX mixture. The enhancement factor of the explosives at some of the major frequency modes are provided in Table 3.2. The maximum PA signal enhancement for the PEDOT+RDX mixture indicates that the electron transfer from the explosive to the PEDOT is most efficient in RDX than TNT, HMX, CL20, and TEX.

Table 3. 2 shows the enhancement factors of explosives when mixed with PEDOT polymer at major frequency modes

Major	Enhancement	Enhancement	Enhancement	Enhancement	Enhancement
Frequency	factor of	factor of TNT	factor of	factor of	factor of TEX
Peak (kHz)	RDX		HMX	CL20	
1.0-1.5	78.45	8.54	4.48	10.62	26.31

4.0-4.5	72.14	3.55	3.24	5.86	40.95
7.0-7.5	118.39	10.57	2.56	7.91	-
11.0-11.5	35.76	1.51	3.18	6.27	-
13.0-14.0	-	-	6.51	23.42	158.49
30.0-32.0	484.27	8.54	4.39	43.14	92.58

• Effect of Incident laser energy on the PA Signal:

Variation of PA mode at 0.5 ms data acquisition time as a function of incident energy for PEDOT, PEDOT+TNT, PEDOT+RDX, PEDOT+HMX, PEDOT+CL20, and PEDOT+TEX is shown in fig.3.9. It is observed that above 2.0 mJ energy, the PA signal for pristine PEDOT increases with increasing incident laser energy, which is not the case for PEDOT and the explosive mixtures. In the case of PEDOT+TNT and PEDOT+HMX, the PA signal either decreases or remains the same till 1.5 mJ incident laser energy but above 1.5 mJ the PA signal increases till 2.2 mJ and on further increasing the incident energy the PA signal decreases, But in the case of PEDOT+RDX, the PA signal continuously increases till 2.2 mJ and after that decreases. Hence, it further confirms our hypothesis that the extent of electron transfer in PEDOT+RDX is more efficient than other explosive samples considered.

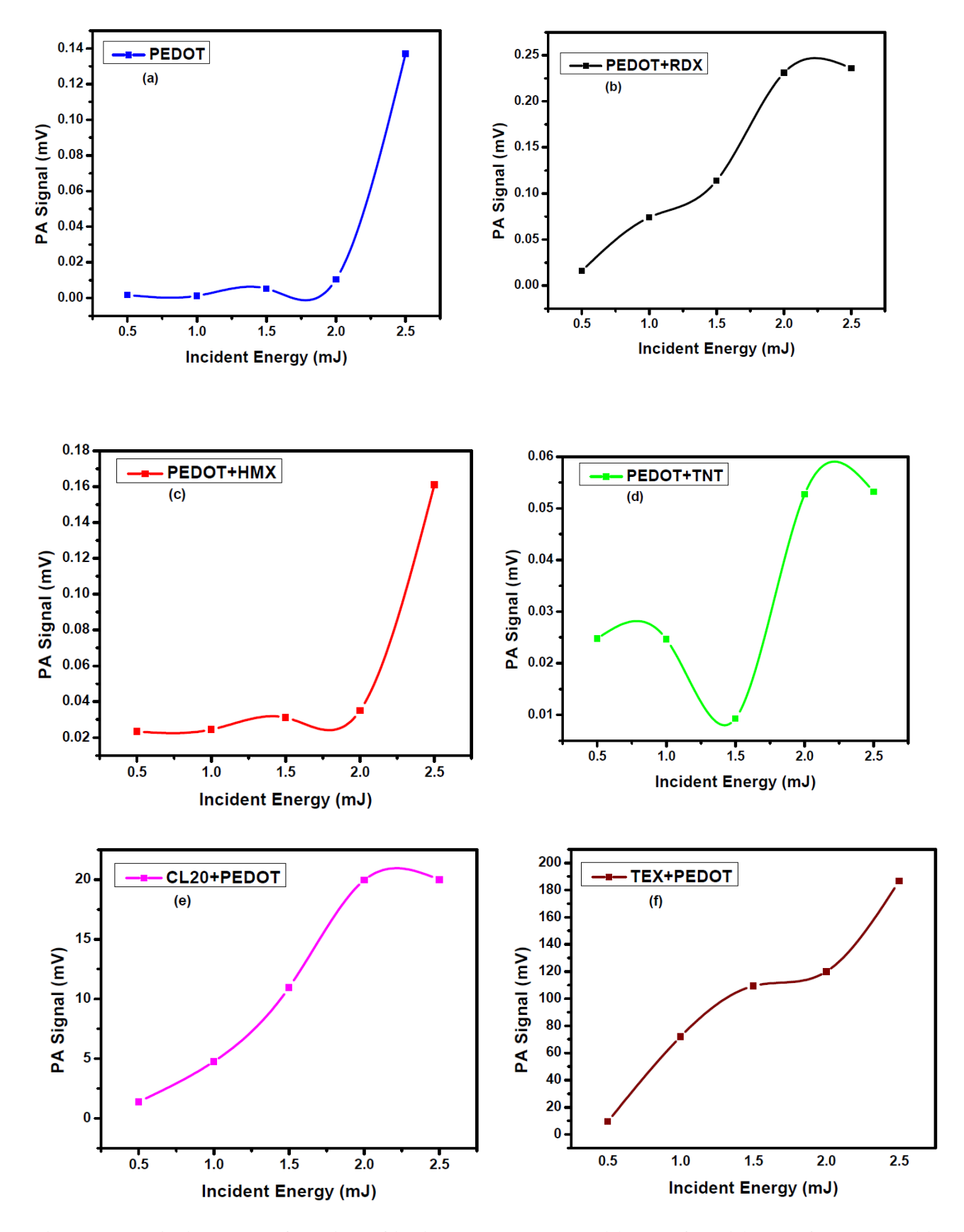


Figure 3. 9 PA signal as a function of incident laser energy (a) PEDOT; (b) PEDOT+RDX; (c) PEDOT+HMX; (d) PEDOT+TNT; (e) PEDOT+CL20 and (f) PEDOT+TEX

• Effect of changes in PA signals as a function of data acquisition time:

To study the variation of PA signals at 19.06 kHz mode for 0.5 mJ incident laser energy with respect to data acquisition time for PEDOT, and its mixture with TNT, RDX, HMX, CL20, and TEX, the data obtained is fitted with exponential fitting using the software as shown in Fig. 3.10 and the respective decay time of the samples are calculated from the fitted curves. The calculated decay time for PEDOT, PEDOT mixed with various explosive samples are provided in Table 3.3. The respective decay times of the samples indicate that the decay time of the PEDOT and the explosive mixtures are shorter than the pristine PEDOT and is well agreement the fact that the exciton decay becomes faster for the mixture of conjugate polymer and explosives than the pure conjugate polymers as reported earlier. Further, it is observed that the decay time for PEDOT+RDX and PEDOT+TNT, PEDOT+CL20, and PEDOT+TEX mixture is much shorter than that of PEDOT+HMX, which is due to the fact that the nitro groups in RDX are attached to a nitrogen atom of the ring. The nitro groups in RDX and HMX are more electron-rich than that of TNT. Since the nitrogen atom of the ring pushes its electrons to the nitro group and hence, the transfer of electrons becomes much efficient from HMX to oxidized PEDOT as compared to other explosives. Thus, the decay time of PEDOT+HMX is much faster than that of PEDOT and different explosive mixtures.

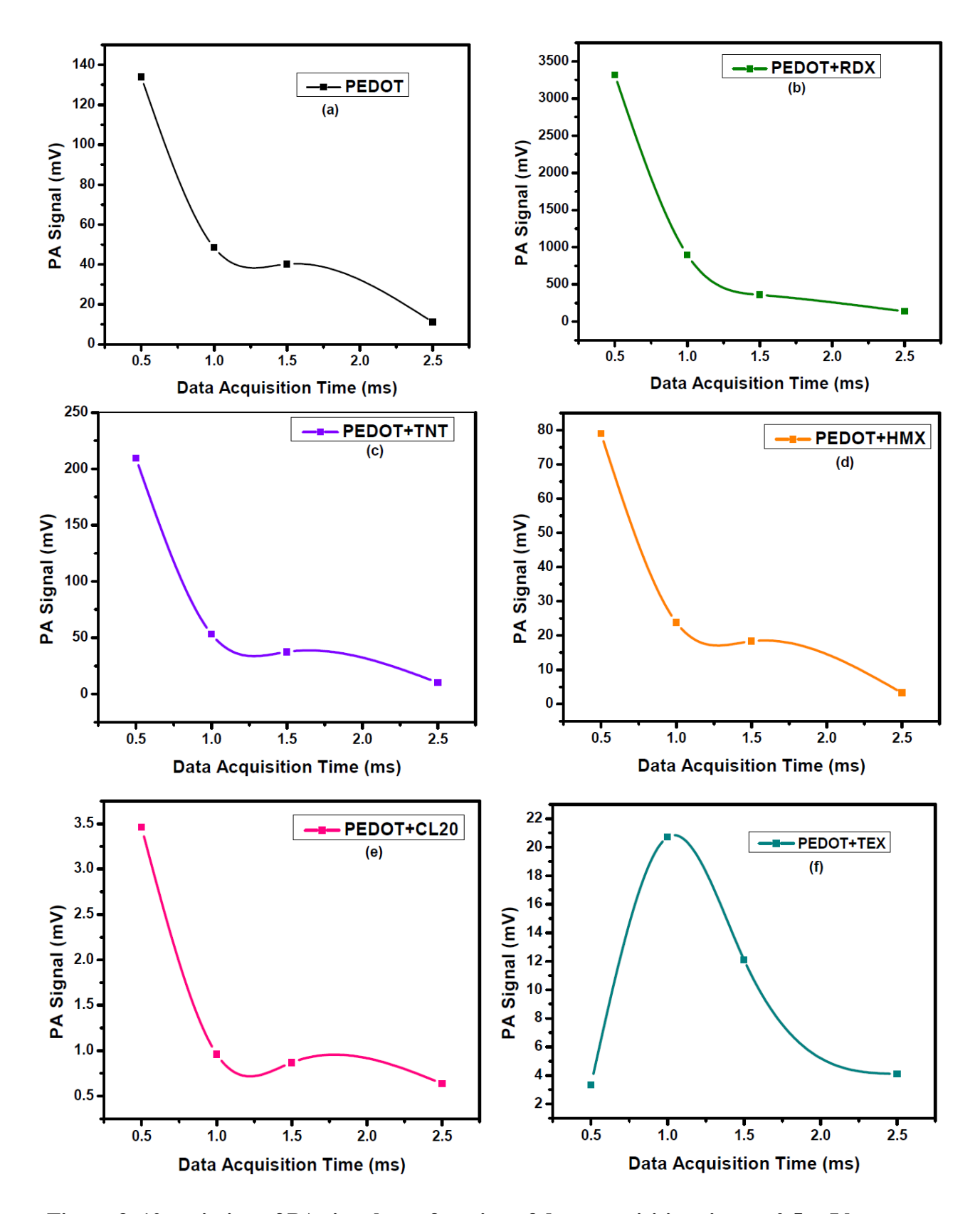


Figure 3. 10 variation of PA signal as a function of data acquisition time at 0.5 mJ laser energy of various samples: (a) PEDOT (b) PEDOT+RDX (c) PEDOT+TNT (d) PEDOT+HMX (e) PEDOT+CL20 and (f)PEDOT+TEX

The decay time of all the mixture samples is comprised in Table 3.3. From fig.3.10, it is observed that most of the materials studied show an exponential decay behavior for PA amplitude as the time varies, which is expressed as:

In the equation, A_1 , t_1 (exponential time decay) and y_0 , are the fitting constant.

Table 3. 3 Represents the decay time rates of the explosives when mixed with PEDOT polymer

S.No.	Sample Name	Decay Time (t ₁) (ms)
1.	PEDOT	0.46
2.	PEDOT+RDX	0.35
3.	PEDOT+TNT	0.32
4.	PEDOT+HMX	0.40
5.	PEDOT+CL20	0.20
6.	PEDOT+TEX	0.042

• Principle of detection of explosives using PEDOT on the basis of Charge Transfer Mechanism:

The role of PEDOT as a sensing medium is explained based on the phenomenon of charge transfer. The presence of positive charge concentrated on the sulfur atom of the conjugated and oxidized PEDOT polymer allows interaction with the negative charges present on the oxygen atom of the nitro-group of the explosives when they are homogeneously mixed together. This leads to an acid-base interaction between PEDOT and the explosive sample. The nitro groups of the high energy materials (explosives) act as weak Lewis-base donors to the PEDOT polymeric chain, providing a donor-acceptor interaction that proves crucial in providing a significant electron-transfer pathway. When exposed to the ring –strain of the explosives, the positive Sulphur-center increases its valence shell to act as a Lewis-base, forming a binding site by a process known as "strain-release" Lewis acidity, as depicted in Fig. 3.11. Since the Lewis acid-base interaction is weak, therefore, efficient detection for explosives is best in the solid phases of samples. When it is irradiated with visible 532 nm laser light, as shown in Fig. 3.11, the free electrons (excitons) produced from the explosive present in the mixture of PEDOT+ explosive interacts with the positive charge present on the sulfur. This can also be termed as an optode interaction, leading to nonradiative thermal pressure waves/ photoacoustic signal.

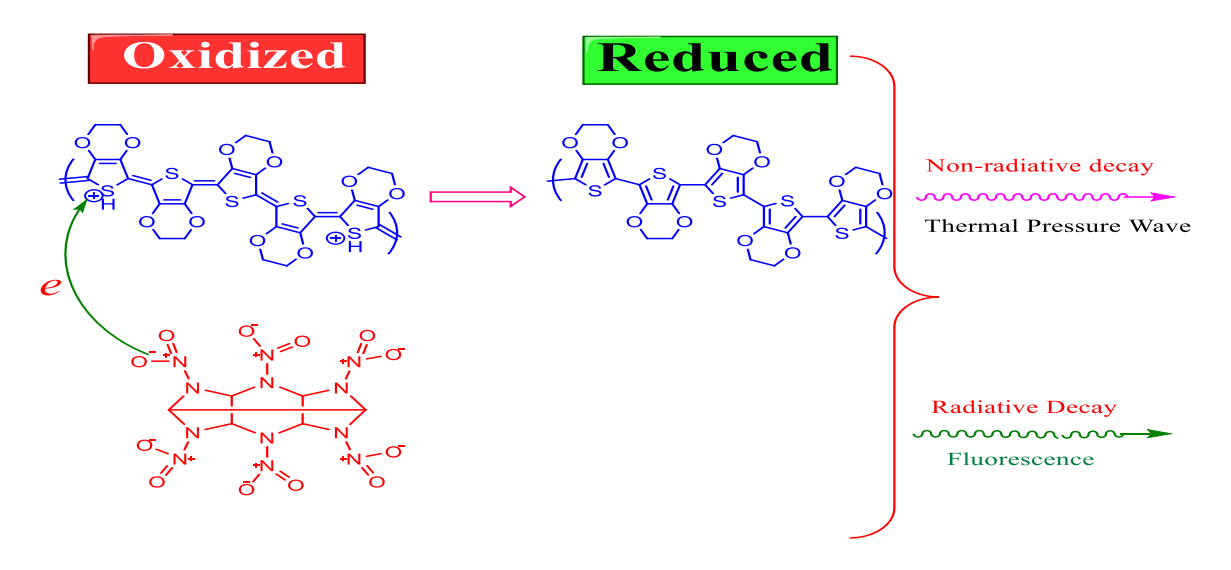


Figure 3. 11 Schematic diagram showing the charge transfer between CL 20 and PEDOT. In order to further prove this the occurrence of this columbic interaction between PEDOT and the explosives, FTIR spectra was analyzed for each of the samples, as represented in Fig. 3.12.

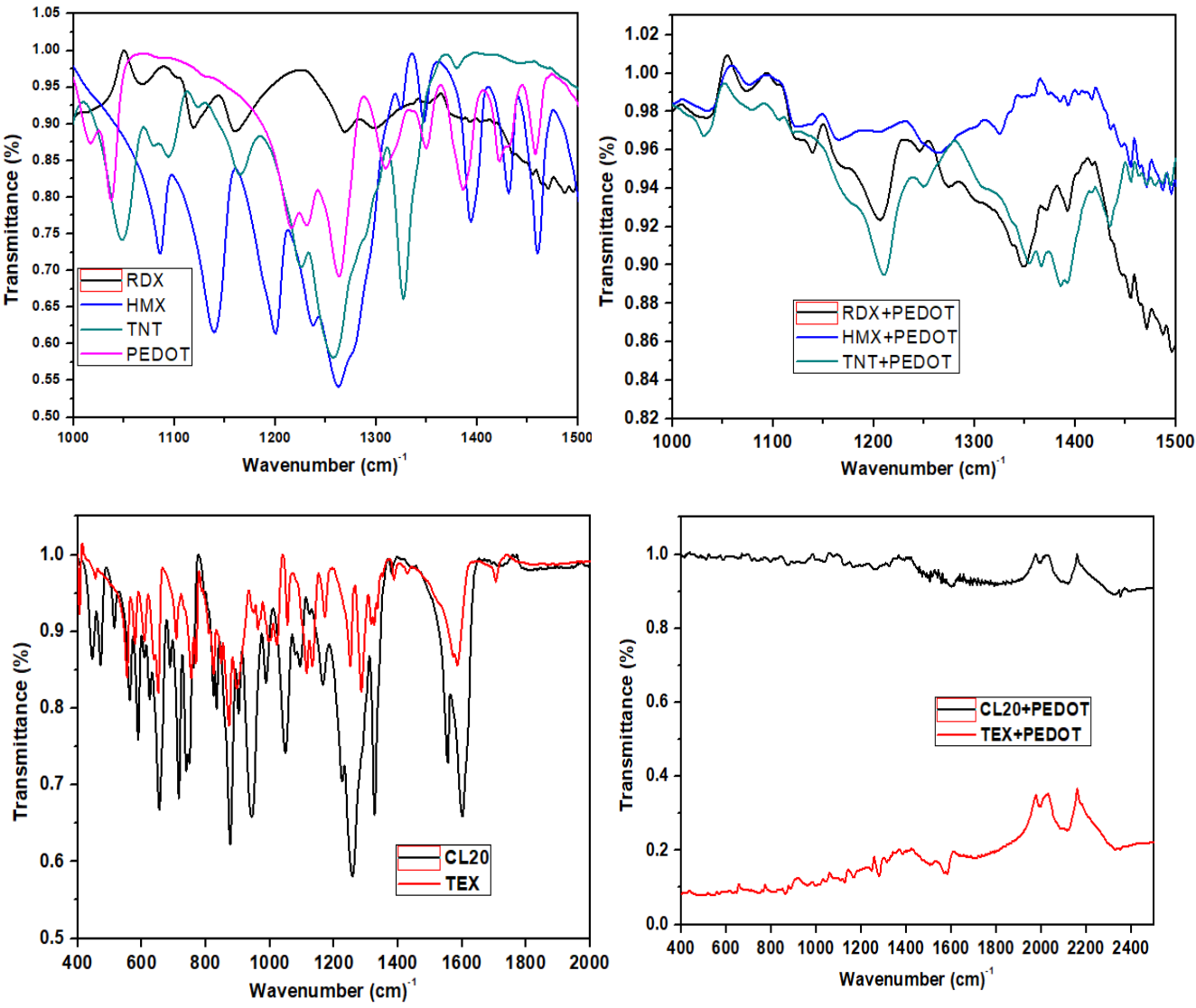


Figure 3. 12 Represents the FTIR spectra of pure explosives and PEDOT + Explosive samples

FTIR spectroscopy of pure explosives and their mixture with PEDOT between 2500 cm⁻¹ to 500 cm⁻¹ range was evaluated. The samples were studied in the range between 1000- 1300 cm⁻¹. Pure explosive samples shows strong absorption peaks at 1030, 1140, 1200, 1260 cm⁻¹, which is associated with C-N bonding. The strongest peak of HMX shows an absorption of 52% whereas TNT, PEDOT, and RDX show an absorption of 57.5% at 1260 cm⁻¹, 82.5% at 1300 cm⁻¹, and 90 % at 1270 cm⁻¹, respectively, as shown in figure 10. However, in the PEDOT+ explosives mixture, we observe drastic changes in the absorption along with the redshift effect towards 1210 cm⁻¹ range. The absorption for TNT, RDX and HMX gets reduced to 92 %, 94% and 97 % with a shift towards 1160 cm⁻¹. This confirms the process of photo-excitation based charge transfer mechanism that is initiated in the visible region. In the visible range, it provides a strong PA signal due to nonradiative decay, whereas, in IR region, it shows an optical bleaching effect for the explosive materials and opaqueity for TEX molecules. The shift of more than 3-4 cm⁻¹ also represents optical bleaching which confirms the electron-phonon interaction within the mixture as well.

• Minimum detection limit:

The estimation of minimum detection limit (D mim) of RDX is shown. 0.2 mg of sample was used in the experiment at 0.5 mJ laser energy. The D $_{mim}$ values of rest of the explosive samples such as TNT ,HMX, and TEX are comparised in the Table 3.4. The maximum strength of the PA signal for RDX was 33.1mV. Therefore, the signal to noise ratio (SNR) of the solis-PA system is:

$$SNR = 10 \log \left(\frac{S}{N}\right)$$

S represents the amplitude of the primary signal, and N represents the noise of the system. The maximum Noise measured in the PA cell is 150 μ V, and the maximum amplitude of the signal is 47.25 mV. Hence,

$$SNR = 10 \log \left(\frac{0.0331}{150 * 10^{-6}} \right) = 23.43 \ dB$$
$$\frac{S}{N} = \frac{0.0331}{150 * 10^{-6}} = 220.66$$

The minimum detection limit (D_{min}) of RDX is the ratio of the amount of the sample used for recording the spectrum and the SNR.

$$Dmin = \frac{0.2 * 10^{\circ} - 3}{220.66} = 9.063 * 10^{-7}g = 906.3 ng$$

Table 3. 4 shows the minimum detection limit of the explosive samples in the PA cell

S.No	Sample	Minimum Detection	Minimum
		Limit (D _{min}) (g)	Detection Limit
			(\mathbf{D}_{\min}) (\mathbf{ng})
1.	RDX	9.063*10 ⁻⁷	906.3
	TT 437	0.026410-8	00.26
2.	HMX	9.036*10 ⁻⁸	90.36
3.	TNT	2.272*10 ⁻⁷	227.2
4.	PEDOT+RDX	1.22*10 ⁻⁷	122.2
5.	PEDOT+HMX	5.789*10 ⁻⁷	578.9
6.	PEDOT+TNT	1.0*10 ⁻⁶	1000

• Interaction of PEDOT with nonexplosive materials containing nitro (-NO₂) group:

In order to investigate the charge transfer mechanism of PEDOT with nonexplosive samples, the same experiment was repeated with nonexplosive samples such as NaNO₂ and NaNO₃. The amplitude of the PA response of pure nonexplosives and their mixtureand is given in Fig. 3.13. It is easy to identify the PA spectra of pure explosives and nonexplosives by the significant difference in their peak amplitude. It also further confirms that PEDOT optode provides very strong and sharp signal for explosives as compared to nonexplosive samples. The PA signal peaks of obtained spectra of pure samples are weak, but their mixture with PEDOT provide broad and distorted peaks. This peak shows 20 times enhancement with respect to the pristine sample. However, the intensity of the signature peak is almost 3.5 times lower than the PA signal of pure PEDOT.

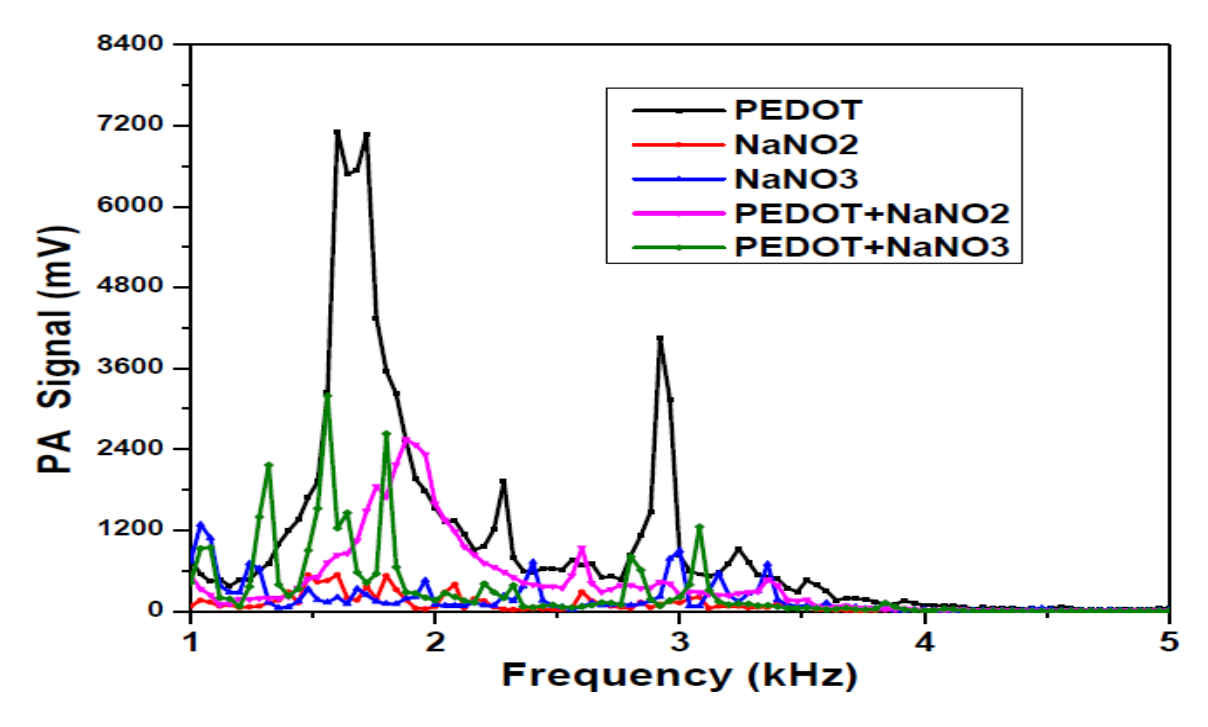


Figure 3. 13 This graph represents the effect of mixing PEDOT to nonexplosive molecules containing nitro (-NO₂) groups.

Section: 2

Time Domain Pulsed Photoacoustic Technique to Study the Effect of Organic and Inorganic Fillers on Thermal and Optical Properties of Natural Rubber/Chlorobutyl Rubber Blend Nanocomposites

3.5 General Introduction About Natural Rubber:

Rubber and elastomeric materials, either obtained from nature or grown chemically, find diverse applications in civil industries and the defense sector, ranging from making tires and tubes, biometric devices and memory storage devices, paints, etc. It is a natural polymeric material and possesses elasticity, which is only possible in molecules with long polymeric chains. The addition of reinforcing agents like carbon black or clay can improve tear strength, tensile strength, abrasive resistance, etc. It is better than metals in the sense that it does not rust with time. However, it has other limitations like degradation when exposed to environmental conditions like moisture, hazardous solvents, etc. Thus there arises a need to reinforce such polymers by the use of appropriate fillers. Here, in this chapter, carbon black was used along with organically modified montmorillonite clay.

It is well known the reinforcing efficiency of different fillers is dependent on the nature of the rubber matrix. It also depends on the physical parameters such as the structure, particle size, experimental conditions, and surface functionality. There are mainly two types of fillers; active and inert. The inert fillers like calcium carbonate, clay, etc. have little effect on rubber products' mechanical and dynamical properties. Still, they can be added to increase the mechanical properties and volume and mass of the

products. Nevertheless, active fillers like carbon black control the rubber product's mechanical, thermal and viscosity properties and increase the modulus at 100-200% because the strong binding force between carbon black and rubber constrains the polymer chain's movement and reduces the chain slipping. Still, the clay filler's surface area is minimal.

Consequently, the binding between rubber and carbon black is minimal. It is attributed to bound rubber where some part of rubber is attached to the filler during milling, which cannot be extended with the regular rubber solvents. This insoluble rubber is called the bound rubber. Fine filler binds a higher percentage of rubber molecules, whereas coarse filler binds none practically.

Pulsed photoacoustic spectroscopy is a well known non-destructive and highly sensitive analytical technique widely used in the low-level detection of atmospheric pollutants, explosives, and impurities in materials and biomedical imaging. Natural rubber is a polymer and has weak absorption in the visible region, but the addition of carbon black as filler enhances the strength of natural rubber and helps assess rubber's absorption and thermal properties. The use of 532nm wavelength source at 7ns repetition rate obtained from Nd: YAG laser system helps record time-domain spectra of rubber samples with different filler types. The study provides the optical and thermal interaction in terms of absorption coefficients, thermal diffusion length, penetration depth, and the samples' decay lifetime. Many researchers have proved that reducing the particle size of carbon black strengthens the rubber products' mechanical properties. It is motivating to determine the effect of nanoparticles in an insoluble form on NR's transport properties. The PA process and photothermal development are conjugate to each other, and thus we have extended our study to measure the thermal diffusivity and penetration depth of rubber samples. However, the present system is based on the RG theory. As per the available reports, this theory is applicable between the 6-12Hz frequency range using CW sources. However, a pulsed laser source was used in the present case. The RG diffusion model is also based on the measurement of amplitude and phase lag, i.e., $\Delta\Phi$ of CW optical/IR sources. However, in the present experiment, the used data acquisition LabVIEW program (designed by Chaudhary et al.) provides an inbuilt facility of signal processing. As a result, the pulsed laser offers an accurate measurement of the diffusion parameter without using any lock-in amplifier. Since ultra-short pulses generate thermal signals during diffusion from one end to another, the diffusion lifetime is 0.2 mm. In contrast, the pulse duration is 100ms, much higher than the samples' diffusion lifetime. Consequently, the present experimental setup confirms 10 Hz nanosecond laser pulses' suitability for recording thermal diffusivity parameters from rubber polymers.

3.6 Experimental Arrangement:

In this experiment, we have used the schematic diagram provided in Fig.2.4, Chapter 2. Samples were prepared by adding CB and clay fillers in different proportions into a 70/30 composition of CIIR /NR blend. Before subjecting the test samples (Table 3.5), the PA cell response, which is cubic shaped ($5\times5\times6$ cm³) and made of aluminum, was calibrated using graphite powder. Graphite is used due to excellent absorption properties in the entire optical wavelength range. After that, small rubber pieces (2.2 mm diameter) were placed in the cell and adjusted in a cell's circular cavity.

A Q-switched Nd: YAG laser of wavelength 532 nm at a 10 Hz repetition rate was used as a source to interact with the samples for recording the PA signals. The generated PA signal is accumulated by a prepolarized microphone (BSW, China), surrounded by a Teflon jacket, located 1 cm away from the sample cavity. Since the obtained PA signal has low intensity, it is amplified with a pre-amplifier before being

fed to the digital storage oscilloscope (Tektronix, 200 MHz) to record the time domain signal. The obtained time-domain signal is converted into FFT spectra with the help of Lab View software.

Table 3. 5 gives the details of the constituents of the samples S1-S5.

Sample no	Constituents
S1	70 g(CIIR)+30 g (Natural Rubber)+20 g (Carbon Black)+0 g (nanoclay)
S2	70 g(CIIR)+30 g (Natural Rubber)+20 g (Carbon Black)+0 g (nanoclay)
S3	70 g(CIIR)+30 g (Natural Rubber)+20 g (Carbon Black)+2 g (nanoclay)
S4	70 g(Organically Modified Clay)+30 g (Natural Rubber)+20 g (Carbon Black)+5 g (nanoclay)
S5	70 g(Organically Modified Clay)+30 g (Natural Rubber)+20 g (Carbon Black)+7.5 g (nanoclay)

3.7 Results and Discussions:

• Variation in the PA amplitude in the time-domain spectra of the Rubber Samples:

Fig. 3.14(s1-s5) show the time domain PA spectra of sample No. s1- s5, as mentioned in table 3.5. These samples' PA spectra were recorded at a fixed data acquisition time of 0.5 ms and 1.0 mJ laser energy. The magnitude of the prominent peaks is comprised in Table 3.6. It is very much clear from the low strength of the PA signal of sample s1 that rubber has weak absorption in the visible region, but a small addition of CB (Carbon Black) enhances the strength of the PA signal by order of 10 times, as observed in fig. 3.14.

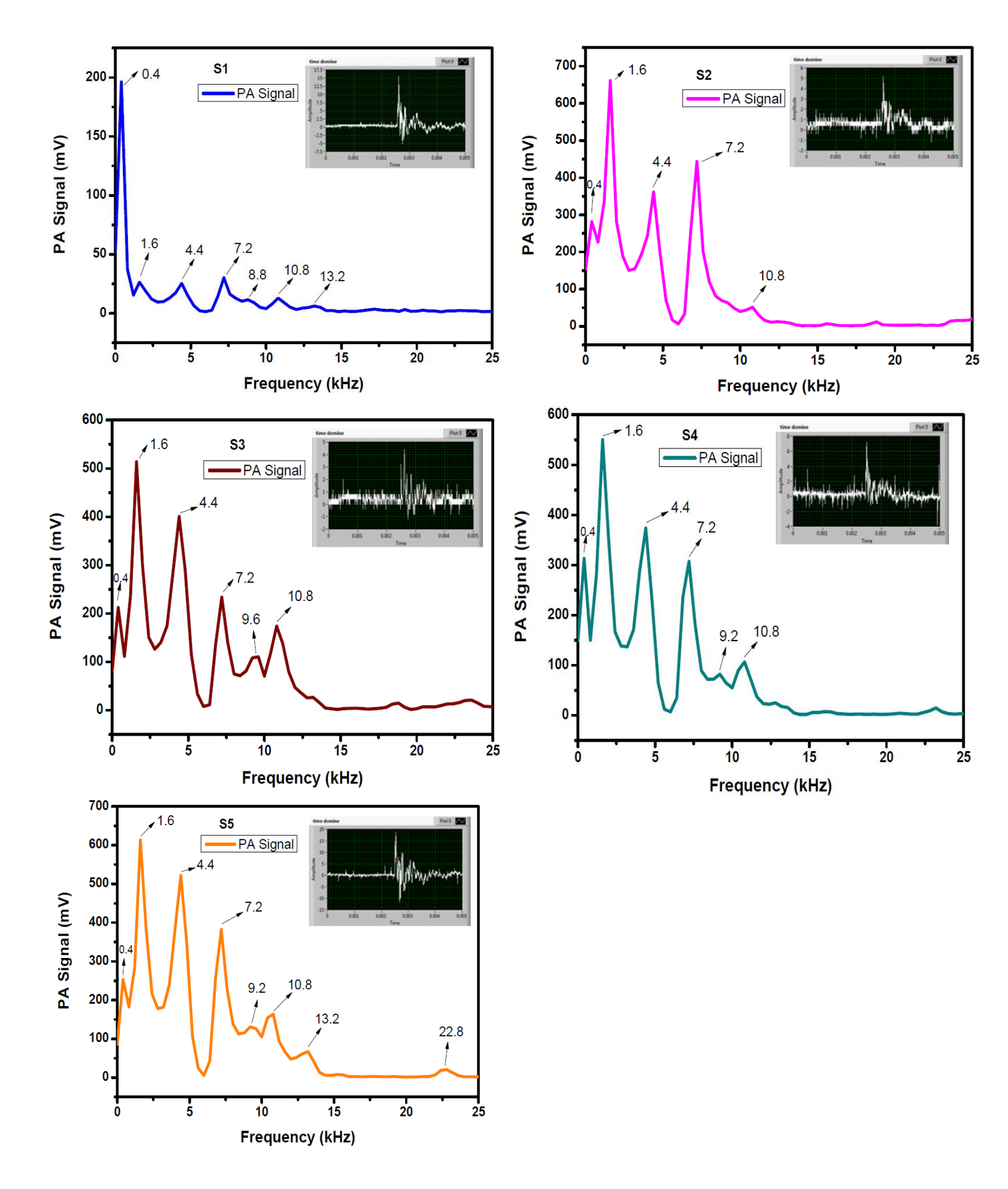


Figure 3. 14 Time-domain PA Spectra of samples S1-S5

Table 3. 6 The amplitude of the prominent peaks of different samples measured at 1.0 mJ

Sample	PA Signal at	PA Signal at	PA Signal at
All samples measured at 1.0 mJ	4.8 kHz (mV)	7.2 kHz (mV)	10.8 kHz (mV)
S1	25	30	15
S2	350	400	100
S3	200	150	55
S4	390	300	100
S5	450	400	100

From Table 3.6, the amplitude of sample 2(CIIR/NR/CB) is more than that of sample 1(CB+NR). So, it can be said that the amplitude of the PA signal increases as carbon black is added to natural rubber. However, for sample 3 to sample 5, clay was added in different proportions (Table 6). S3, which has the least amount of clay, shows a decrease in amplitude and decreases for S4 and S5. Also, the surface characteristics of CBs leads to the formation of bound rubber in various rubber filled systems. Therefore, the interaction parameter is mostly dominated by the promotion of bound rubber in CB filled elastomers. Accordingly, independence of the interaction parameter of CB with respect to the rubber matrix suggests that the interfacial interaction be more influenced by the structure and surface topology of the CBs. This promotes higher bound rubber, and hence, the rubber macromolecules attached to the carbon black surface are mainly through physical adsorption. However, clay is added to the samples; we do not observe the same nature. This is due to non-interaction of clay particles with the rubber matrix.

• Data Acquisition time vs. the PA Signal amplitude:

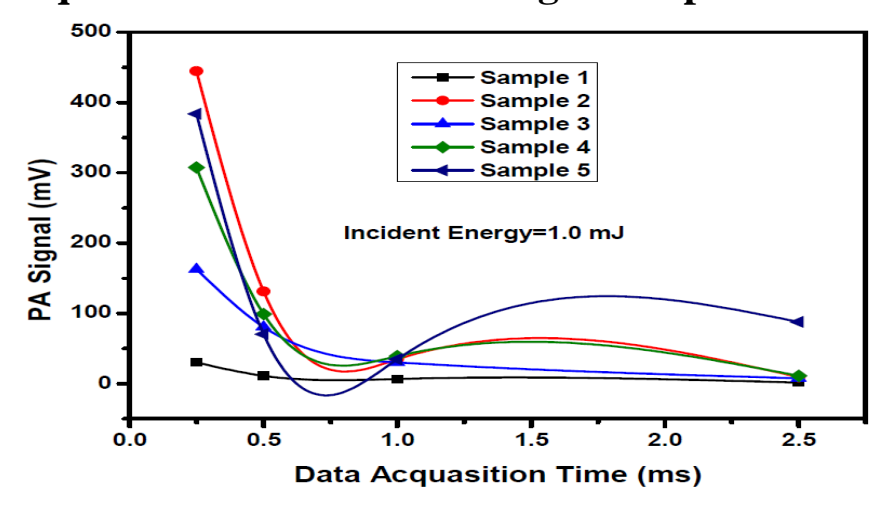


Figure 3. 15 Shows the data acquisition time of samples with their exponential decay nature and their exponential fit

From fig. 3.15, it is seen that all the samples show an exponential decay behavior for the PA amplitude as the time varies. The equation can be represented as:

$$y = y_0 + A_1 e^{-x/t_1}$$

Where y_0 , A_1 , t_1 (exponential decay time of acoustic mode to data acquisition time) are the fitting constants comprised in Table 3.7.

Table 3. 7 Comprises the calculation of decay time constants of the samples S1-S5

Sample	y ₀	\mathbf{A}_1	Decay Time t ₁ (ms)
S1	3.25	83.88	0.22
S2	16.87	1571.7	0.19
S3	9.34	316.09	0.34
S4	20.64	1010.11	0.198
S5	61.22	11500.1	0.069

• Absorption coefficient (α):

The absorption coefficient data is estimated from the rising part of the time domain signal, as explained in the flow chart. It is represented in Fig. 3.16.

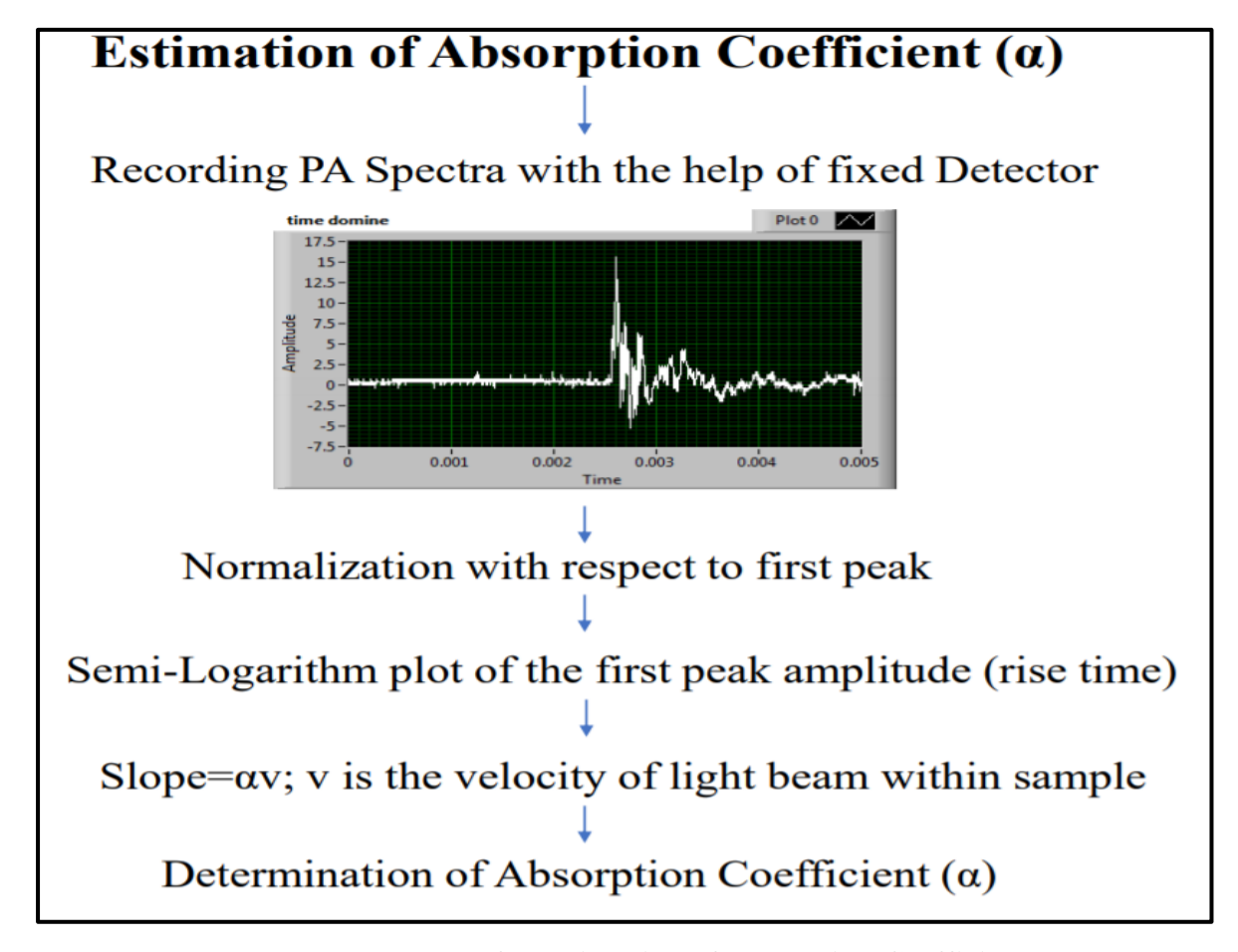


Figure 3. 16 Represents the procedure for estimation of absorption Coefficient

The absorption coefficient of each of the samples (S_1-S_5) is given in Table 3.8.

Table 3. 8 shows the absorption coefficients of the samples S1-S5

S.No.	Sample Name	Absorption Coefficient (cm	
1.	S ₁	0.75	
2.	S_2	2.72	
3.	S ₃	3.75	
4.	S ₅	3.76	
5.	S ₆	4.22	

• Estimation of Thermal Diffusivity and Penetration Depth:

The application of photoacoustic effect to measure thermal diffusivities for thin films was made by Adams and Kirkbright [15]. When a sample's surface gets illuminated with a modulated light beam, the generated temperature oscillations propagate across the sample. Pressure oscillations which arise due to

photoacoustic phenomenon of the same frequency are induced by temperature oscillations in the gas chamber, where they are detected by a microphone. The photoacoustic signal obtained by this procedure has a phase shift with respect to the incident chopped light. This happens due to a considerable time-lag between the heat transfer process and propagation of light. This time-lag can be removed by proper selection of chopper frequency in the case of CW photoacoustic systems. In this experiment, pulsed laser energy is used as a source to analyze the sample. This is controlled by two means; repetition rate of the laser system and proper selection of the samples' data acquisition time.

Thermal diffusivity (α) is measured through frequency analysis of the PA Signal's amplitude or phase by determining the characteristic frequency, f_c . It is given by the expression

$$\alpha = f_c * l_s^2$$

Here, ls represents the thickness of the sample, and f_c is the characteristic frequency. The slope of the graphs obtained must be less than 1. The straight line obtained for the reference sample has a slope (-1), which is in agreement with RG theory for an optically opaque and thermally thick material. The above expression of α can estimate the thermal diffusivity of the material. Since it is a derived quantity and it controls the rate of heat transfer through a medium, the unit of thermal diffusivity is basically [length²/s], where some of the literature report it as [m²s⁻¹],[cm²s⁻¹], or as [mm²s⁻¹]. One crucial condition which must be satisfied for optically opaque and thermally thick sample is:

$$\mathbf{a}_{s} * l_{s} < 1$$

as provides the thermal diffusion coefficient and is given by the formula,

$$a_s = \left(\frac{\pi f}{\alpha}\right)^{1/2}$$

Now, the penetration depth is the length up to which the incident beam is able to penetrate and interact with the sample. It is given by the following formula:

$$D_t = \left(\frac{2\alpha}{\omega}\right)^{1/2}$$

 ω is the central frequency. In the present case, the length is 0.2mm, which is 0.0002 meter. So, the unit of thermal diffusivity is considered as [m²s⁻¹]. All the calculated results are summarized in Table 3.9 below:

Table 3. 9 Comprises thermal diffusivity and the penetration depth of the samples s1-s5.

Sample	Thickness(mm)	Thermal Diffusivity(α)*10 ⁻⁶ [m ² s ⁻¹].	asls<1	Penetration Depth(Dt)(ms-2)
S1	0.20	0.88	0.79	0.1
S2	0.10	0.44	0.56	5.19

S3	0.25	1.1	0.88	0.13
S4	0.15	0.66	0.68	7.91
S5	0.2	0.88	0.79	0.1

• Calculation of viscosity (η) using Einstein, Guth, and Gold (EGG) Equation:

ECG equation is used to estimate the theoretical effect of reinforcing agents' viscosity of the rubber sample. The equations are as follows:

$$M = M_0(1 + 2.5C - 14.1C^2) \tag{1}$$

$$\eta_f = \eta_u * (1 + 2.5 * C + 14.1C^2)$$
(2)

$$\frac{\eta_s}{C} = 2.5 \tag{3}$$

Where η_f and η_u are the viscosities of filled rubber with reinforcing material and unfilled rubber, which is the natural rubber, C is the volume fraction of the filler. Bound rubber, which is produced after adding the fillings, is added to the filler fraction so that the viscosity of the filled rubber increases accordingly. The effect of bound rubber in the case of carbon black is not prominently manifested in carbon black.

Using the above equations (1-3), the value of Π was calculated. For Sample 1, which contained CR+NR, the value was 0.85, while for sample 2, which consisted of CR+NR+CB, the value was 0.54. The rest of the samples, which had varied proportions of natural clay, had imaginary values for ' η .' These shows that there is a limit to this equation in the domain of photoacoustic data when recorded for samples that have natural clay as a constituent.

3.8 Conclusion of the chapter:

In conclusion, in this chapter, we have carried out studies on two polymers; a conducting conjugated polymer, PEDOT, and natural rubber polymer. We have successfully demonstrated the stable physical interaction between the sulfur atom present on the PEDOT polymeric chain and the lone pair of electrons on the oxygen atom of explosives using Photoacoustic spectroscopy, explaining the phenomena charge-transfer mechanism which enables the detection of the explosive materials. Among the various explosives (RDX, TNT, HMX, CL20, and TEX), the maximum enhancement in the PA signal was observed in the case of RDX. The shorter decay time for the mixtures of PEDOT and explosives than that of pristine PEDOT represents exciton decay is faster for the combination than a new molecule. Absorption coefficient values showed that the PEDOT and the explosive mixtures have a higher absorption coefficient than new explosives. A maximum decrease in the absorption coefficient of PEDOT and explosives mixture was observed for PEDOT+RDX, which further confirms the interaction between PEDOT and RDX is maximum, resulting in faster electron transfer between PEDOT and RDX. We also studied the effect of non-explosive molecules containing nitro (NO₂) groups like nitrates and nitrites to clearly show the difference in the behavior of PEDOT when mixed with explosive and non-explosive

compounds. For forensic applications, we have also proposed storing PEDOT polymer in spray bottles keeping in mind its easy use on the field, cost, and availability.

In the case of rubber polymer, we have studied the effects of different fillers and reinforcing agents and have demonstrated the use of Time-domain photoacoustic technique in optical region λ =532 nm wavelength for the recording of several new parameters such as absorption coefficients, thermal diffusion coefficients, and penetration depth of purely natural rubber and rubber reinforced with carbon and clay fillers. The values of the absorption coefficient were in the range 39-89 cm⁻¹whereas thermal diffusion length and penetration depth is of the order of 0.1-0.625 x10⁻⁶ and 0.1-7.9 microns. Also, the calculated penetration depth and the thermal diffusivity of the rubber samples are matched with the necessary condition of $\alpha_s l_s < 1$ for thermally thick and optically opaque materials.

References:

- 1. M. Marshall, J. C. Oxley, Aspects of Explosives Detection, Ed., Elsevier, Oxford UK, (2009).
- 2. Forensic Investigation of Explosions (Second Edition), A. Beveridge, Ed., Taylor & Francis Ltd, CRC Press, Boca Raton FL (2012).
- 3. J. S. Caygill, F. Davis, S. P. J. Higson, Current trends in explosive detection techniques. Talanta, 88, 14-29 (2012).
- 4. E. K. Jenkins, T. M. Lee-Fowler, A. T. Craig, E. N. Behrend, G. E. Moore, Effects iof oral administration of metronidazole and doxycyline on olfactoary capabilities of explosives detection dogs. Am. J. Vet. Res. 77, 906-912 (2016).
- 5. J.I. Steinfeld, J. Wormhoudt, Explosives detection: A Challenge for Physical Chemistry. Annu. Rev. Phys. Chem. 49, 203–232 (1998).
- 6. T. M. Swager, Sensor Technologies Empowered by Materials and Molecular Innovations. Angew. Chem. Int. Ed. 57, 4248 –4257 (2018).
- 7. S. W. Thomas, G. D Joly, T. M. Swager, Chemical sensors based on amplifying fluorescent conjugated polymers. Chem Rev., 107, 1339-1386 (2007).
- 8. T. L. Andrew, T. M. Swager, A Fluorescence Turn-On Mechanism to Detect High Explosives RDX and PETN. J. Am. Chem. Soc. 129, 7254-7255 (2007).
- 9. D. Gopalakrishnan, W. R. Dichtel, Direct Detection of RDX Vapor Using a Conjugated Polymer Network. J. Am. Chem. Soc. 135, 8357–8362 (2013).
- 10. A. Lan, K. Li, H. Wu, A Luminescent Microporous Metal–Organic Framework for the Fastand Reversible Detection of High Explosives. Angew. Chem. Int. Ed. 48, 2334-2338 (2009).
- 11. XS Wang, L. Li, DQ Yuan, YB Huang, R. Cao, Fast, highly selective and sensitive anionic metalorganic framework with nitrogen-rich sites fluorescent chemosensor for nitro explosives detection. J. Hazard. Mater., 344, 283-290 (2018).
- 12. A. K. Chaudhary, G. C. Bhar, Low-limit photoacoustic detection of solid RDX and TNT explosives with Carbobdioxide Laser, J. Appl. Spectrosc. 73, 123-129 (2006).
- 13. K. S. Rao, A. K. Chaudhary, Investigation of solid carbon blacks using pulsed photoacoustic and double resonant Raman Spectroscopy for identification of trinitrotoluene Sens. And Act. B: chemical 231, 830-836 (2016).
- 14. B. K. Sikder, A step towards the processability of insoluble or partially soluble functional and structural variants of polymers based on 3,4-alkylenedioxythiophene.RSC Adv. 6, 107776-107784, (2016).
- 15. M. J. Adams, G. F. Kirkbright, Thermal Diffusivity and Thickness Measurements for Solid Samples Utilising the Optoacoustic Effect, Analyst, 102, 678-682 (1977).
- 16. H. P. Martinez, C. D. Grant, J. G. Reynolds, W. C. Trogler, Silica anchored fluorescent organosilicon polymers for explosives separation and detection. J. Mater. Chem. 22, 2908-2914 (2012).
- 17. N. Pon Saravanan, S. Venugopal, N. Senthilkumar, P. Santosh, B. Kavita, P. H. Gurumallesh, Voltammetric determination of nitroaromatic and nitramine explosives contamination in soil. Talanta 69, 656–662 (2006).

- 18. Y. M. Taha, M. T. Saowapon, H. D. Osthoff, Detection of Nonvolatile Inorganic Oxidizer-Based Explosives from Wipe Collections by Infrared Thermal Desorption-Direct Analysis in Real Time Mass Spectrometry. Anal. Bioanal. Chem, 410, 4203-4212. (2018).
- 19. R. Gillibert, J. Q. Huang, Y. Zhang, W. L. Fu, Explosive detection by Surface Enhanced Raman Scattering. Trends in Analyt. Chem. 105, 166-172 (2018).
- 20. K. Wells, D. A. Bradley, A review of X-ray explosives detection techniques for checked baggage. Appl. Radiat. Isot. 70, 1729-1746 (2012).
- 21. W. Liu, M. Li, K. Gao, Experimental research on detecting explosives by pulsed fast thermal neutron analysis. J. Neutron Res. 18, 29-34 (2015).
- 22. R. R. Kunz, K. E. Gregory, D. Hardy, The role of stationary phase selection on performance for explosives analysis using GC-ECD. J. Chromatogr. Sci. 48, 310-316 (2010).
- 23. H. A. Yu, Recent developments in the electrochemical detection of explosives: Towards field-deployable devices for forensic science. Trends in Analyt. Chem. 97, 374-384 (2017).
- 24. Z. Du, T. Sun, J. Zhao, D. Wang, Z. Zhang, W. Yu, Development of a plug-type IMS-MS instrument and its applications in resolving problems existing in in-situ detection of illicit drugs and explosives by IMS. Talanta 184, 65-72 (2018).
- 25. A. Hahma, O. Pham-Schoenwetter, Odor samples for the training of explosive-sensitive dogs. Eur. Pat. Appl. EP 3281930 A1 20180214 (2018).
- 26. T. L. Andrew, T. M. Swager, Detection of explosives via photolytic cleavage of nitroesters and nitramines. J Org Chem. 76, 2976-2993 (2011).
- 27. T. M. Swager, Sensor Technologies Empowered by Materials and Molecular Innovations. Angew. Chem. Int. Ed. (2018), 57, 4248 –4257.
- 28. S. W. Thomas, G. D. Joly, T. M. Swager, Chemical sensors based on amplifying fluorescent conjugated polymers. Chem Rev. 107, 1339-1386 (2007).
- 29. X. Liu, Y. Xu, D. Jiang, Conjugated Microporous Polymers as Molecular Sensing Devices: Microporous Architecture Enables Rapid Response and Enhances Sensitivity in Fluorescence-On and Fluorescence-Off Sensing. J. Am. Chem. Soc. 134, 8738-8741 (2012).
- 30. Y. Che, D. E. Gross, H. Huang, D. Yang, X. Yang, E. Discekici, Z. Xue, Diffusion-Controlled Detection of Trinitrotoluene: Interior Nanoporous Structure and Low Highest Occupied Molecular Orbital Level of Building Blocks Enhance Selectivity and Sensitivity. J. Am. Chem. Soc. 134, 4978-4982 (2012).
- 31. B. Bhusan, A. Halasz, J. Spain, S. Thiboutot, G. Ampleman, J. Hawari, Biotransformation of Hexahydro-1,3,5-trinitro-1,3,5-triazine Catalyzed by a NAD(P)H: Nitrate Oxidoreductase from Aspergillus niger. Environ. Sci. Technol. 36, 3104-3108 (2002).
- 32. A. Lan, K. Li, H. Wu, D. H. Olson, T.J. Emge, A Luminescent Microporous Metal—Organic Framework for the Fastand Reversible Detection of High Explosives. Angew. Chem. Int. Ed. 48, 2334-2338 (2009).
- 33. XS Wang, L. Li, DQ Yuan, YB Huang, R. Cao, Fast, highly selective and sensitive anionic metalorganic framework with nitrogen-rich sites fluorescent chemosensor for nitro explosives detection. J. Hazard. Mater. 344, 283-290 (2018).
- 34. R. Freeman, T. Finder, T.; Bahshi, L.; Gill, R.; Willne, I. Functionalized CdSe/ZnS QDs for the Detection of Nitroaromatic or RDX Explosives. Adv. Mater. (2012), 24, 6416–6421.

- 35. F. Yehya, A. K. Chaudhary, D. Srinivas, K. Muralidharan, Study of thermal decomposition mechanism and low-level detection of explosives using pulsed photoacoustic technique. Appl. Phys. B. 121, 193.202 (2015).
- 36. K. S. Rao, A. K. Chaudhary, N. Kommua, A. K. Sahoo, Evaluation of thermal stability and acoustic fingerprint spectra of energetic 1,2,4-triazoles based on bond lengths of chemical substituents using pulsed photoacoustic technique. RSC Adv. 6, 4053-4062 (2016).
- 37. A. K.Chaudhary, K. S. Rao, A. S. Kumar, Study of thermal decomposition mechanisms and absorption cross section of nitro-rich phenyl- and bis-series 1,2,3-triazoles. Appl Opt. 55, 817-824 (2016).
- 38. J. C. Sanchez, A. G. DiPasquale, A. L. Rheingold, W. C. Trogler, Synthesis, Luminescence Properties, and Explosives Sensing with 1,1-Tetraphenylsilole- and 1,1-Silafluorene-vinylene Polymers Chem. Mater. 19, 6459–6470 (2007).
- 39. J. C. Sanchez, W. C. Trogler, Efficient blue-emitting silafluorene–fluorene-conjugated copolymers: selective turn-off/turn-on detection of explosives. J. Mater. Chem. 18, 3143–3156 (2008).
- 40. S. J. Toal, D. Magde W. C. Trogler, Luminescent oligo(tetraphenyl)silole nanoparticles as chemical sensors for aqueous TNT. Chem. Commun. 5465–5467 (2005).
- 41. J. Yang, S. Aschemeyer, H. P. Martinez, W. C. Trogler, Hollow silica nanospheres containing a silafluorene–fluorene conjugated polymer for aqueous TNT and RDX detection. Chem. Commun. 46, 6804–6806 (2010).
- 42. J. C. Sanchez, S. A. Urbas, S. J. Toal, A. G. DiPasquale, A. L. Rheingold, W. C. Trogler, Catalytic Hydrosilylation Routes to Divinylbenzene Bridged Silole and Silafluorene Polymers. Applications to Surface Imaging of Explosive Particulates. Macromolecules, 41, 1237–1245 (2008).
- 43. H. Sohn, M. J. Sailor, D. Magde, W. C. Trogler, Detection of Nitroaromatic Explosives Based on Photoluminescent Polymers Containing Metalloles. J. Am. Chem. Soc. 125, 3821–3830 (2003).
- 44. J. C. Sanchez, A. G. DiPasquale, A. A. Mrse, W. C. Trogler, Lewis acid-base interactions enhance explosives sensing in silacycle polymers. Anal. Bioanal. Chem. 395, 387–392 (2009).
- 45. S. J. Toal, J. C. Sanchez, R. E. Dugan, W. C. Trogler, Visual Detection of Trace Nitroaromatic Explosive Residue Using Photoluminescent Metallole-Containing Polymers. J. Foren. Sci. 52, 79–83 (2007).
- 46. S. J. Toal, W. C. Trogler, Polymer sensors for nitroaromatic explosives detection. J. Mater. Chem. 16, 2871–2883, (2006).
- 47. H. Sohn, R. M. Calhoun, M. J. Sailor, W. C. Trogler, Detection of TNT and Picric Acid on Surfaces and in Seawater by Using Photoluminescent Polysiloles. Angew. Chem. 113, 2162–2163 (2001).
- 48. J. C. Sanchez, S. J. Toal, Z. Wang, R. E. Dugan, W. C. Trogler, Selective Detection of Trace Nitroaromatic, Nitramine, and Nitrate Ester Explosive Residues Using a Three-Step Fluorimetric Sensing Process: A Tandem Turn-off, Turn-on Sensor. J. Foren. Sci. 52, 1308–1313 (2007).
- 49. L. Groenendaal, F. Jonas, D. Freitag, H. Pielartzik, J. R. Reynolds, Poly(3,4-ethylenedioxythiophene) and Its Derivatives: Past, Present, and Future. Adv. Mater. 12, 481-494 (2000).
- 50. G. Heywang, F. Jonas, Poly(alkylenedioxythiophene)s—new, very stable conducting polymers. Adv. Mater. 4, 116-118 (1992).
- 51. L. M. Herz, C. Silva, A. C. Grimsdale, K. Müllen, R. T. Phillips, Time-dependent energy transfer rates in a conjugated polymer guest-host system. Phys. Rev. B. ,70 165207 (2004).

- 52. A. Das , K.W. Sto ckelhuber , R. Jurk , M. Saphiannikova , J. Fritzsche , H. Lorenz , M. Klu ppel , G. Heinrich, Modified and unmodified multiwalled carbon nanotubes in high performance solution-styrene—butadiene and butadiene rubber blends, Polymer 49 5276–5283 (2008)
- 53. Akbar Varamesh, Mahdi Abdollahi, and Homayon Hossein Khanli, Structure and Properties of NR/BR Blend/Clay Nanocomposites Prepared by the Latex Method, ISSN 0965545X, Polymer Science, Ser. A, 55, 2, 115–120, (2013)
- 54. Morteza Ahmadi, Akbar Shojaei, Cure kinetic and network structure of NR/SBR composites reinforced by multiwalled carbon nanotube and carbon blacks, Thermochimica Acta, 566 238–248 (2013)
- 55. S. Choi, C. Nah, S.G. Lee, C.W. Joo, Effect of filler–filler interaction on rheological behaviour of natural rubber compounds filled with both carbon black and silica, Polym. Int. 52 23–28, (2003)
- 56. M. A. Lo´pez-Manchado, J. Biagiotti, L. Valentini, J. M. Kenny, J ApplPolym Sci, 92,3394, (2004)
- 57. S. Thomas, R. Stephen, Rubber Nanocomposites, Preparation, Properties and Applications, Wiley, Singapore, (2010)
- 58. A. K. Bhowmick, S. K. De, Effect of temperature curing and curing system on structure–property relations of rubber blends, Rubber Chem. Technol., 53, 960–974, (1980)
- 59. D. J. Kohls, G. Beaucage, Rational design of reinforced rubber, Curr. Opin. Solid State Mater. Sci. 6, 183–194, (2002)

Chapter: 4

Effect of charge transfer mechanism of PEDOT polymer on Stokes and anti-Stokes Raman lines of RDX, HMX, and TNT Explosive samples

4.1 Abstract:

In continuation of the previous discussion in chapter 3 based on the absorption process of photoacoustic technique, we have continued exploring the charge-transfer mechanism involved for enhancing the signal of explosives under the influence of 532 nm wavelength. In this chapter, we have studied the effect of the Charge-transfer mechanism in Raman Spectroscopy and observed the impact of photon-electron-phonon interaction, a new area of research in the field of conductive PEDOT polymer. The pristine PEDOT is less sensitive to 532 nm wavelength (2.33eV) in the case of Raman Spectroscopy peak shift if we compare with that of the absorption technique of photoacoustic spectroscopy the previous chapter. However, it influences the mixture's Raman Stokes and anti-Stokes lines of explosives. The study also reveals that a small quantity (1.0 mg) of powdered PEDOT polymer is suitable to initiate the charge transfer mechanism between its oxidized state to the lone pairs of electrons present on the nitro group explosive molecules.

Consequently, the peak intensity of obtained Raman spectra of RDX, HMX, and TNT is reduced by order of 22.5, 11.45, and 17.2 times, respectively, along with the shift of the NO₂ vibrational modes. This phenomenon is also attributed to Photon-electron-phonon interaction. We have further estimated the functional group's reduced mass to ascertain the force constant and the intensity ratios of AS /S lines to confirm the charge transfer mechanism. The charge transfer mechanism's effect is also reflected in a drastic change in FTIR spectra's transmission /absorption characteristics of the same PEDOT and explosive mixtures. The investigation was restricted to the visible range. Still, when the same mix of samples was subjected to the tunable IR region, we observed an optical bleaching effect in the mixture of pure PEDOT and explosives, which is still another area of rigorous investigation.

4.2 Introduction:

We observe the Raman effect when a photon is an incident on a molecule. It interacts with the electric dipole inherent in the molecule, giving rise to scattering. Raman scattering is based on the difference in the vibrational or rotational quantum states of molecules interacting with the light beam. When a sample is irradiated by a source of light, having a frequency v_0 , a part of the light in the form of photons are absorbed by the sample, whereas another part of this light beam gets scattered (Fig.4.1) into Rayleigh Scattering and Raman Scattering. The Rayleigh scattering is strong and has the same frequency as the incident beam, v_0 while the Raman scattering is very weak (around v_0 the incident beam) and has two frequencies; $v_0 - v_m$, which represents the Stokes line and $v_0 + v_m$ which is the anti-Stokes line and v_m is the vibrational frequency of the molecule.

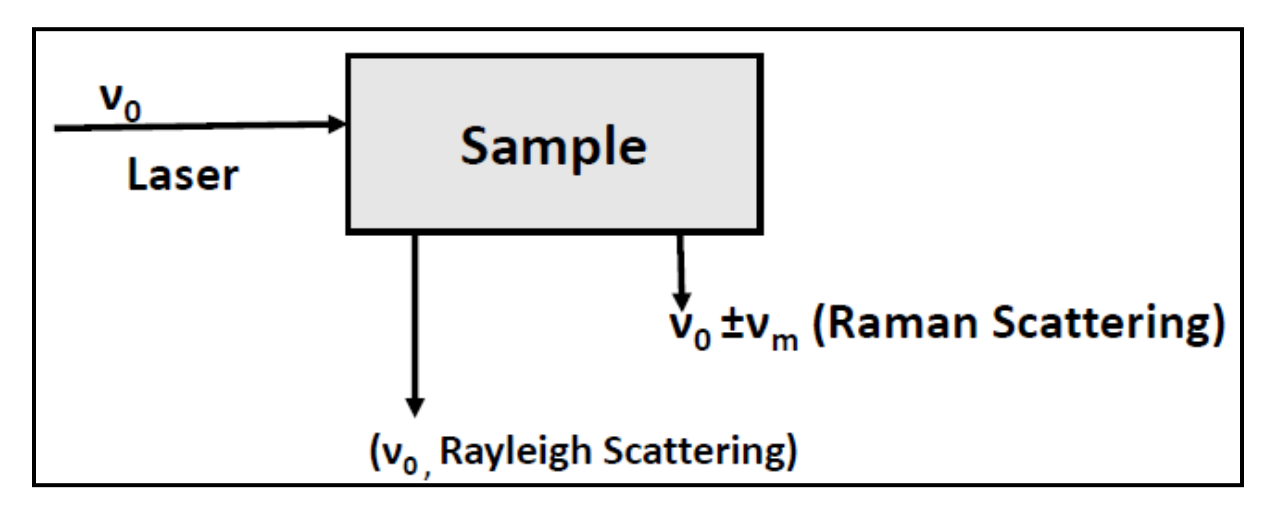


Figure 4. 1 shows the mechanism of scattering when a sample interacts with a light source

We measure the vibrational frequency (ν_m) with respect to the shift from the incident beam frequency (ν_0) . Although Raman spectra are typically observed for vibrational and rotational transitions, it is possible to observe Raman spectra for electronic transitions between ground states and lower energy excited states. Raman spectra are measured in the UV-Vis region. Further details about the classical theory of Raman Scattering is given in Appendix D.

Previously, we studied about the techniques of detecting high energy materials/explosives using Photoacoustic spectroscopy. This chapter is dedicated to finding an alternative method for detection of such materials. We have chosen Raman Spectroscopic technique because of various factors. It is easily available, has easy to operate instrumentation, requires very small amount of sample and encompasses both IR as well as visible region of the electromagnetic spectra. Laser and other technological advancements have helped Raman spectroscopy to become a non-invasive and non-destructive optical spectroscopic technique.

Pristine PEDOT polymer is less sensitive to Raman intensity at 532 nm but has a significant effect on the Raman lines after being mixed with explosives. The experimental results clearly show a shift in the NO₂ vibration modes and a reduction in the intensity of Raman bands. It is attributed to photon —electron — phonon interaction .We have estimated the reduced mass of the functional group to ascertain the force constant and the intensity ratio of anti-Stokes to the Stokes line, which helps us to reveal the charge transfer mechanism, which in turn, also substantiate the results obtained with the help of Photoacoustic spectroscopic technique. We have analyzed the individual Raman spectra of all the explosive samples considered along with their mixture in the PEDOT polymer matrix using only 1.0 mg of sample. It helped us to understand the charge transfer mechanism from explosive samples to PEDOT using a Raman spectroscopic technique in solid powder form. This approach can identify the participation of fundamental vibration modes of explosives and their mixture with PEDOT. The study confirms PEDOT interaction with explosives that causes a change in polarizability and broadening of the transition level due to the charge transfer mechanism. The present study opens a new channel of sensing mechanism research in physically mixed compounds, which are based on the chemical theory of charge transfer and supported by Pulsed Photoacoustic and FTIR spectroscopy.

Over the past few decades, the detection of explosive materials have become a major area of research and researchers all over the world are trying to develop different types of experimental and analytical techniques to meet the purpose, in terms of the cost-effectiveness, adequate flexibility to serve as a portable explosive detection system, use of low concentration of samples, and being non-destructive. Among the existing analytical technique, Raman spectroscopy is one of the most versatile experimental investigative techniques with enormous applications such as characterization of new organic materials, structural and standoff detection, and surface chemistry, which can also be used in the defense of homeland security. Also, with the advent of portable Raman systems, this can prove to be an important explosive detection technique. Researchers have effectively used Raman spectroscopy for the identification and characterization of explosive materials, especially resonance Raman spectroscopy in UV region has been extensively explored for explosive detection.

Various researchers, such as NorazrienaYusoff, have reported the detection of bio-analytes by using Graphene– polymer-based hybrid materials to develop electrochemical sensors. Also, Chao Wang et al. have reported an electro-chemiluminescent (ECL) immune-sensor for detecting Diclofenac as bioreceptor. HoHyun Jang et al. worked on a piezoresistive pulse sensor for its feasibility to measure physiological signals from the human body using a biomimetic mold replicated with PEDOT: PSS thin film. Tae- Gyu Kang et al. researched the thin conducting polymer's microwave transmission properties. SERS enhancement of Raman signal from RDX at 670 nm excitation, in the presence of graphene oxide, has also been reported.

For obtaining a near-perfect Raman spectrum, the Raman signal must dominate the fluorescence caused by the background. Moreover, improvised Raman techniques, which include remote Raman detection, need further improvement in noise ratio movement to reduce the fluorescence effect. Since the vapor pressures of almost all conventional explosives are very low, the detection of these explosives is still a challenging task in the vapor phase. Some other factors, such as limited sample size, deliberately concealed explosives, and interference from other organic molecules, are some of the physical constraints

in explosive detection. In the present Chapter, we propose a new approach for the identification of explosives by mixing them with PEDOT (poly (3,4ethylenedioxythiophene)) conducting polymer. The excellent conductivity of PEDOT is attributed to the presence of free charge carriers, which enables it to act as a sensor for detection of the low quantity of explosives, using the principle of charge-transfer phenomena, as discussed in Chapter 3.

• Brief Introduction to the samples used in the chapter:

Explosives used in this chapter for study are divided into three main categories (i) Aliphatic nitrate ester (R-O-NO₂), (ii) the nitro-aromatic (Ar-NO₂), and (iii) the cycloaliphatic nitramine (>N-NO₂) groups. The detailed discussion of the classification of explosives has already been discussed in Chapter 3. Among the explosives used in this thesis, TNT is the most commonly used explosive due to its ease of manufacturing and low melting point. RDX, a colorless, polycrystalline material, also known as hexahydro-1, 3, 5-trinitro-s-triazine and cyclotrimethylenetrinitramine has very high chemical stability. Similarly, HMX is another explosive whose properties can be compared with RDX, apart from having a high density and high melting point.RDX and HMX belong to the category of nitramine. A single RDX molecule comprises three nitro groups, whereas HMX contains four nitro groups, and a single TNT nitroaromatic molecule consists of three nitro groups and one methyl group. PEDOT is highly stable, both chemically and thermally, with a reasonable band gap and has low redox potential. Its high ductile properties and high conductivity are used in different applications such as an electrolyte in polymer capacitors, an organic light-emitting diode, and an electrode. It is also used in terahertz antireflection coatings and as pressure and Piezo-Resistive sensors. Researchers have also demonstrated the detection of NH₃ gas with PEDOT: PSS and graphene–PEDOT: PSS by an ink-jet printing technique. PEDOT was synthesized in our laboratory, adopting solid-state polymerization following the already reported procedure (Facile Solid-State Synthesis of Highly Conducting Poly (ethylene dioxythiophene) by the researchers H. Meng and D. F. Perepichka.

4.3 Experimental Details:

For the experiment, 1 mg of PEDOT powder was mixed with an equal amount of explosive in solid form and was ground together using a mortar-pestle for thorough mixing. It was then subjected to a Raman system (model No. WITEC-CRM200) with 600 line/m grating and an objective lens of 100 mm (NA=0.95). Nd: YAG laser at low power of 0.1 mW and 532 nm wavelength was used as a source. The Scan-Control spectroscopy plus software (WITECH, GMBH, and Germany) was used to control the stage movement and record the Raman spectra point by point using WITEC- alpha 300 micro Raman spectrometer.

4.4 Results and Discussion:

Figure 4.2 shows the Raman spectrum of pure PEDOT polymer. The vibration mode frequency at 1522 cm⁻¹ and 1578 cm⁻¹ present in the range corresponds to C_{α} = C_{β} asymmetric stretching. It is also referred to as 'G' or graphite peak due to carbon. The intense vibration bands observed at 1412 cm⁻¹ and 1441 cm⁻¹ between the range of 1400–1490 cm⁻¹ corresponded to symmetric C_{α} = C_{β} (-O) stretching and referred

to as 'D' or defect peak. The D peaks observed at 1359 cm⁻¹ and 1255 cm⁻¹ are due to C_{β} – C_{β} stretching and $C\alpha$ – C_{α} inter-ring asymmetric stretching, respectively. The vibration peaks at 1012 cm⁻¹, 1105 cm⁻¹,1132 cm⁻¹, and 617 cm⁻¹ are due to C–O–C and C–S–C stretching. The mode frequency observed at 571 cm⁻¹ corresponds to the oxyethylene ring deformation. The vibration mode frequencies at 3405 cm⁻¹ and 3496 cm⁻¹ can be assigned to overtones. The prominent peak at 2003 cm⁻¹ is the fingerprints of sphybridized carbon atoms due to stretching modes of C–C bonds.

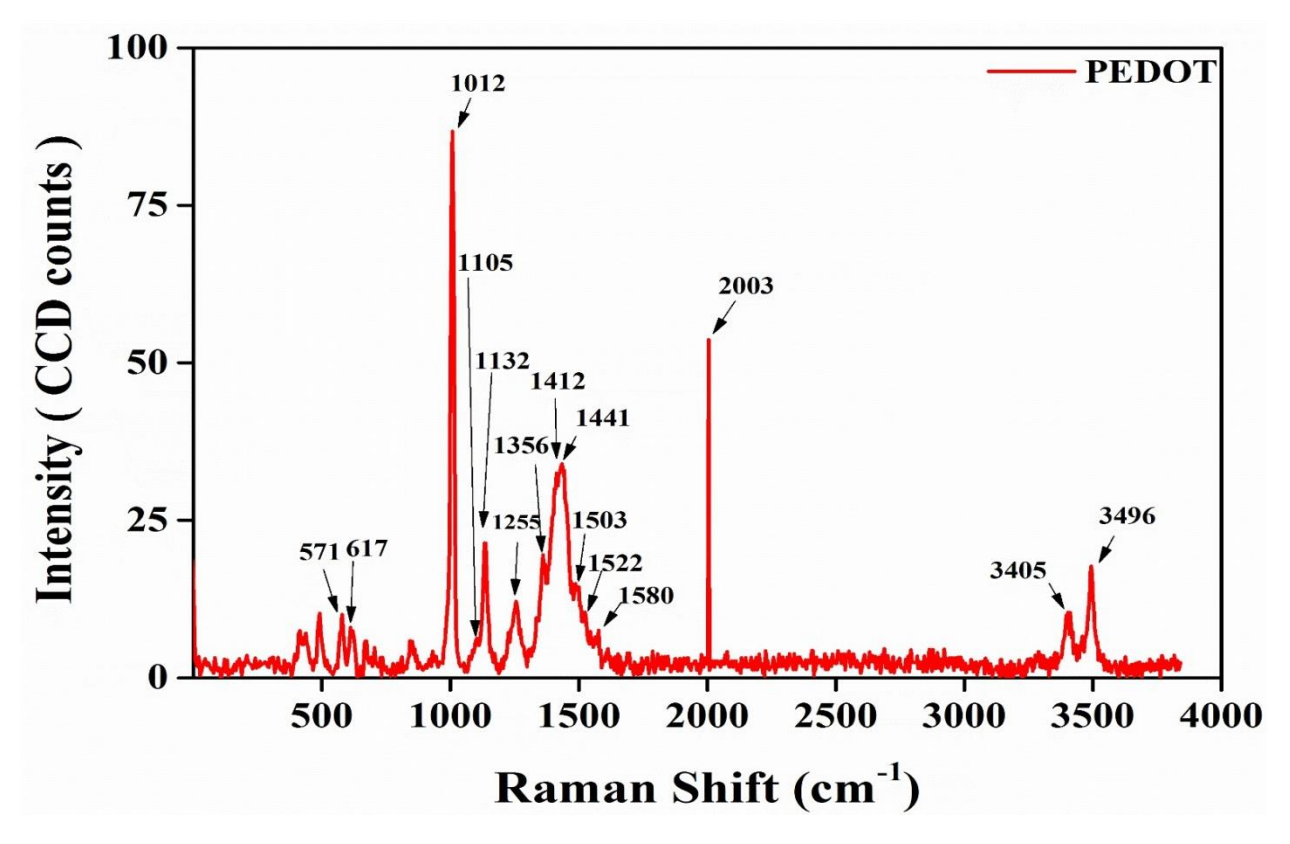


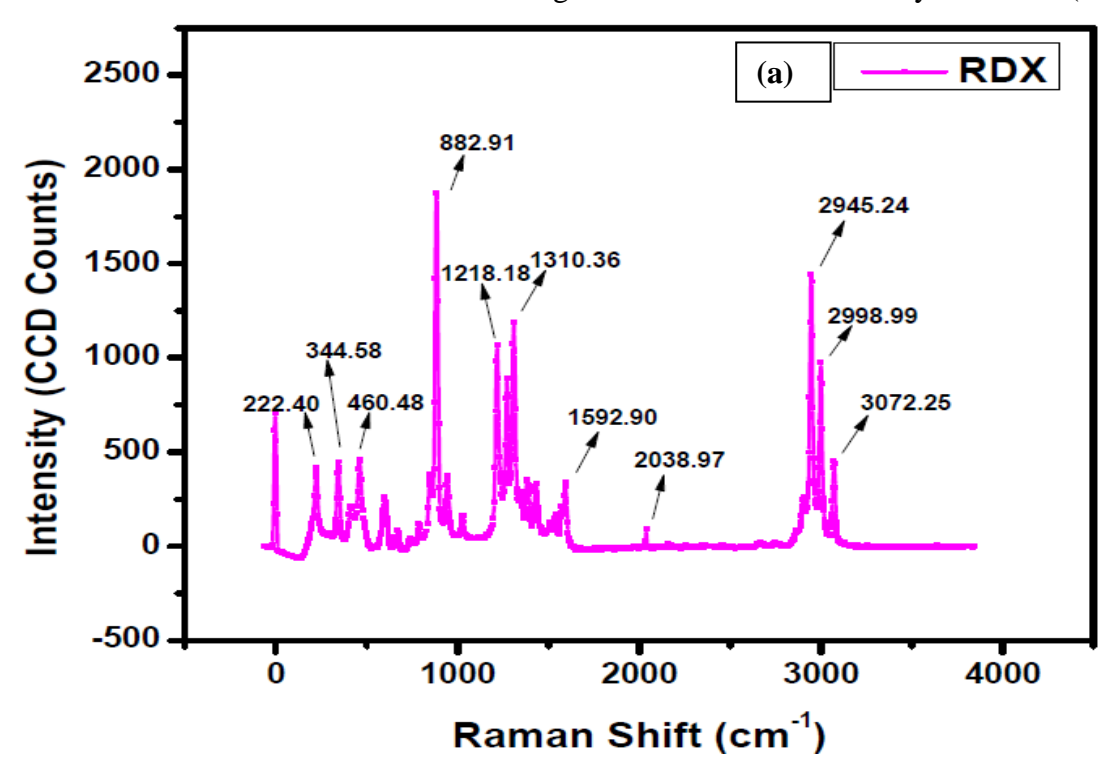
Figure 4. 2 The Raman spectrum of pure PEDOT polymer

Table 4. 1 Represents the peak assignment of some of the prominent peaks obtained in the Raman spectra of pure PEDOT.

Raman Shift(cm ⁻¹)	Peak Assignment
1012	C-O-C stretch
1132	C-S-C deformation
1441	Symmetric $C_{\alpha}=C_{\beta}$ (-O) stretching/ D-peak
2003	C-C Stretch
3405	Overtones
3496	Overtones

Analysis of RDX and RDX+PEDOT Raman spectra:

Figure 4.3 (a) represents the Raman spectrum of RDX. The most substantial peak is observed at 882.91 cm⁻¹, that corresponds to the symmetric ring stretching. The vibration mode frequency at 1027 cm⁻¹ is due to the ring-type vibrations of the c-N-c molecule. The peak obtained at 1218 cm⁻¹ is also due to the same region. Some of the less prominent peaks which have less intensity are due to the vibration mode frequency and are observed at 1384 cm⁻¹ and 1436 cm⁻¹, respectively. These peaks are obtained because of the CH₂ skeletal motions. The vibration modes corresponding to asymmetric stretching modes of the NO₂ group appear between 1540 cm⁻¹ and 1600 cm⁻¹ range. The vibration mode frequency at 1272 cm⁻¹ corresponds to the symmetric stretching of NO₂, and these frequencies modes obtained are close to the previously reported results by various researchers. This variation is attributed to the considerable strain in the RDX ring in its crystalline state. Two types of NO₂ groups in the staggered chair conformation of the molecules in RDX appear in terms of the split peak at 1592.90 cm⁻¹, whereas the peak obtained at 1310.36 cm⁻¹ is assigned to N -N vibrations of the molecules. The bands that appear between 2900 and 3100 cm⁻¹ regions are assigned to CH₂ stretching modes. The symmetric mode gives a very strong band in the spectra. The two peaks at (2945.24 cm⁻¹ and 2998.9 cm⁻¹) separated by approximately 54 cm⁻¹ are assigned to the symmetric stretching mode. The frequency mode for the CH₂ asymmetric stretching in the case of RDX is 2999 cm⁻¹, which is higher than that obtained for cyclohexane (2852 cm⁻¹).



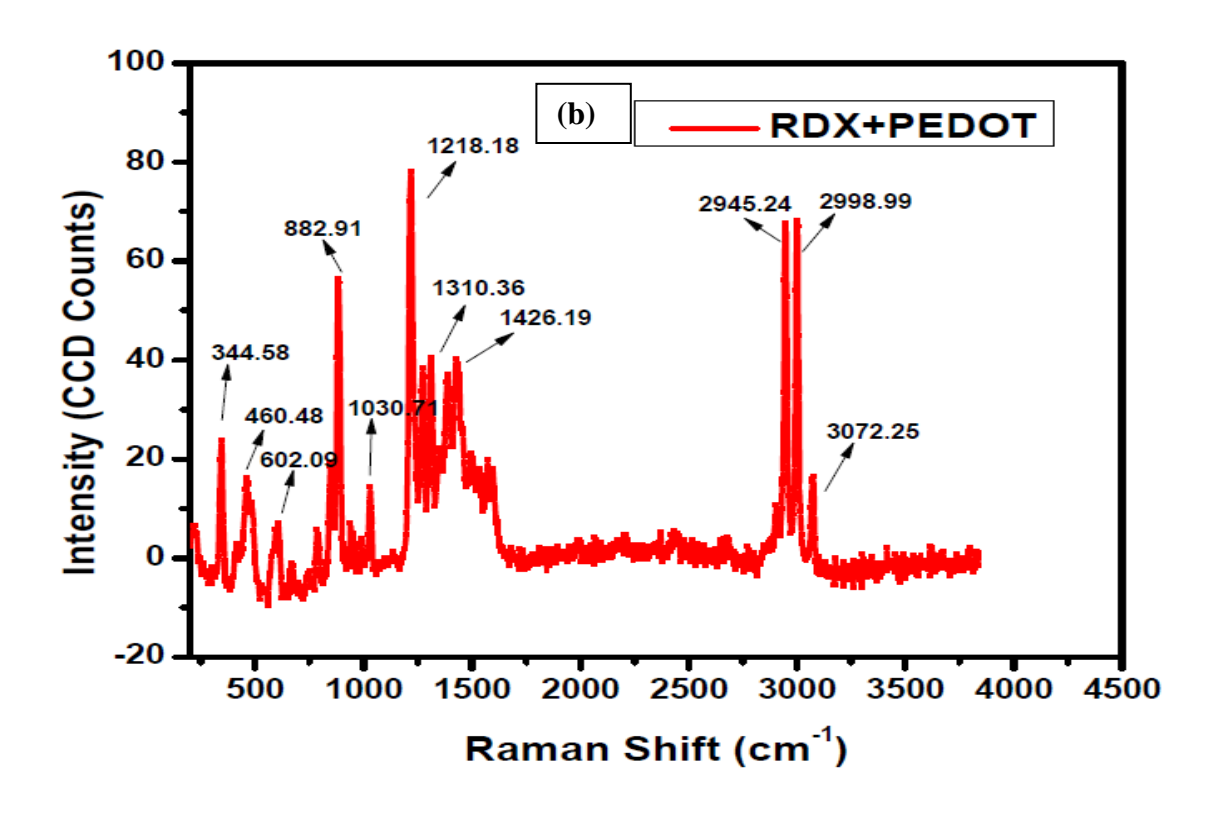


Figure 4. 3 (a) shows the Raman spectra of RDX and (b)and the RDX +PEDOT mixture.

Table 4. 2 Provides the details of the most prominent peaks observed in the Raman spectra of RDX and RDX+PEDOT.

S. No.	Major Raman	Peak	Major Raman	Peak
	Peaks for RDX	Assignment	Peaks for	Assignment
	(cm ⁻¹)	(RDX)	RDX+PEDOT	(RDX+PEDOT)
			(cm ⁻¹)	
1.	882.91	Symmetric Ring	882.91	=C-H bend
		Stretching		
2.	1218.00	C-N-C ring	1030.00	C-N-C Ring
		Vibration		Vibration
3.	1272.00	Symmetric NO ₂	1217.00	C-N-C Ring
		Stretching		Vibration
4.	1310.36	N-N Vibration	1218.18	C-O-C
				Asymmetric
				Stretch

5.	1592.90	Staggered-chair	-	-
		conformation		
6.	2900-3100	CH ₂ Stretching	2945.24	C-H Stretch
7.	2999	Symmetric stretching mode	2998.99	C-H Stretch

The Raman spectrum for RDX and PEDOT mixture excited by 532 nm visible light is given in fig. 4.3(b). Some of the most prominent peaks are observed at 882.91, 1218.18, 2945.24, and 2998.99 cm⁻¹. These peaks correspond to =C-H bend, C-O-C antisymmetric stretch, C-H stretch (for 2945.24 cm⁻¹), and 2998.99 cm⁻¹. However, numerous less prominent peaks having lower intensities have also been observed in the fingerprint spectra of PEDOT+RDX. The vibration frequency at 222 cm⁻¹ is due to C-N-C bending and torsion of the molecule. The band around 414 cm⁻¹ is due to an essential ring bending vibration, whereas the bands around 750 cm⁻¹ region such as 736 cm⁻¹ and 785 cm⁻¹ show a higher shift for the nitro group and are due to NO₂ vibration mode in deformation form. Usually, the skeletal NO₂ ways appear in the Raman spectrum's low-frequency region and are mixed with a large degree of torsional and bending ring vibrations. Two sets of vibration mode frequencies at 1030 cm⁻¹ and 1217 cm⁻¹ have been assigned to ring-type vibrations due to the C-N-C molecule. The Raman peaks, the intensity for the NO₂ vibration modes of RDX, and RDX+PEDOT are given in Table 4.3.

Table 4. 3 The NO₂ vibration mode frequency analysis of pristine RDX and mixed with PEDOT (RDX+PEDOT).

Raman sh	nift		The ratio of	IAS/ IS - RDX	IAS/ IS RDX+ PEDO	Diff. IAS/ IS RDX+	% change in the force constant	Assignment
RDX (cm ⁻¹)	RDX + PEDOT (cm ⁻¹)	Diff. (cm ⁻ 1)	Raman Intensities		Т	PEDOT - IAS/ IS - RDX		
460.45	461.71	-1.27	17.44	1.22	1.19	0.03	-0.548	NO ₂ skeletal
601.78	606.32	-4.54	17.12	1.29	1.28	0.03	-1.525	NO ₂ skeletal
1271.92	1273.27	-1.35	23.28	1.72	1.62	0.10	-0.212	NO ₂ symmetric stretching

1540.96	1536.46	4.50	15.42	1.93	1.73	0.14	0.583	NO ₂ asymmetric stretching
1593.21	1596.65	-3.44	20.41	1.97	1.83	0.14	-0.432	NO ₂ asymmetric stretching

The intensity of Raman spectra of PEDOT+RDX is reduced by 20 times as compared to pure RDX. Also, the most significant polarizability change in pure RDX is observed at 882.91 cm⁻¹. It is due to the symmetric ring stretching vibration. The mixture (PEDOT+RDX) has the most substantial peak at 1218.18 cm⁻¹, which is also due to ring stretching. When we compare the spectra of RDX+PEDOT and pure RDX, we observe that most of the vibration modes have a shift in the 0.38 cm⁻¹ to 4.98 cm⁻¹ range. The Raman peaks obtained at 414 cm⁻¹, 785 cm⁻¹, and 1310 cm⁻¹ due to C-N-C stretching, NO₂ deformation and N-N stretching, respectively have shown less sensitivity to PEDOT in terms of the frequency shift. The percentage change in the force constant for particular modes is negative which indicates a strengthening of the bond when it is mixed with PEDOT. However, for specific modes of vibration, the interaction between the atoms get weakened, and it leads to an increase in force constant. Also, as shown in Table 3, if the percentage of change in force constant is negative, the corresponding vibration frequency get red-shifted, and when it is positive, the decrease in force constant can lead to a change in the characteristic frequency towards the left-hand side of the Raman spectra. PEDOT's effect on RDX is also observed in terms of shift in the ratio of the intensity of anti-Stokes and Stokes lines, as shown in Fig. 4.4.

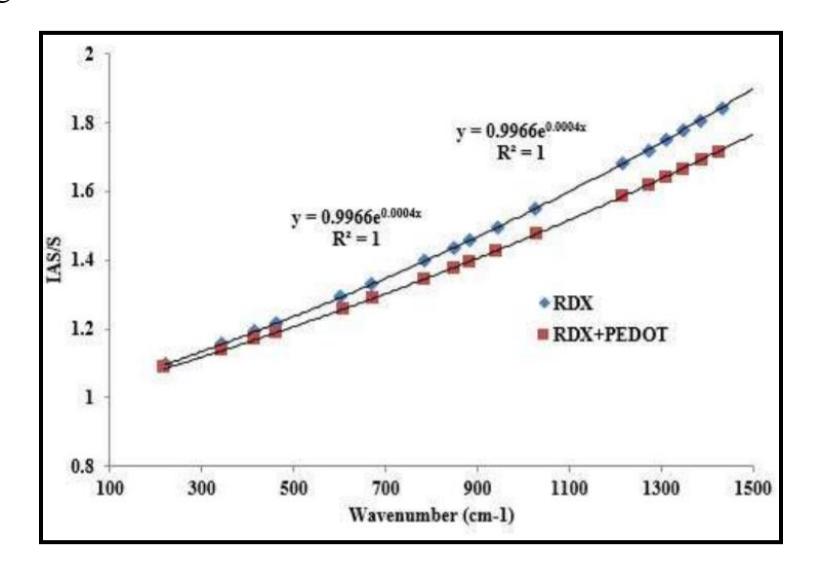


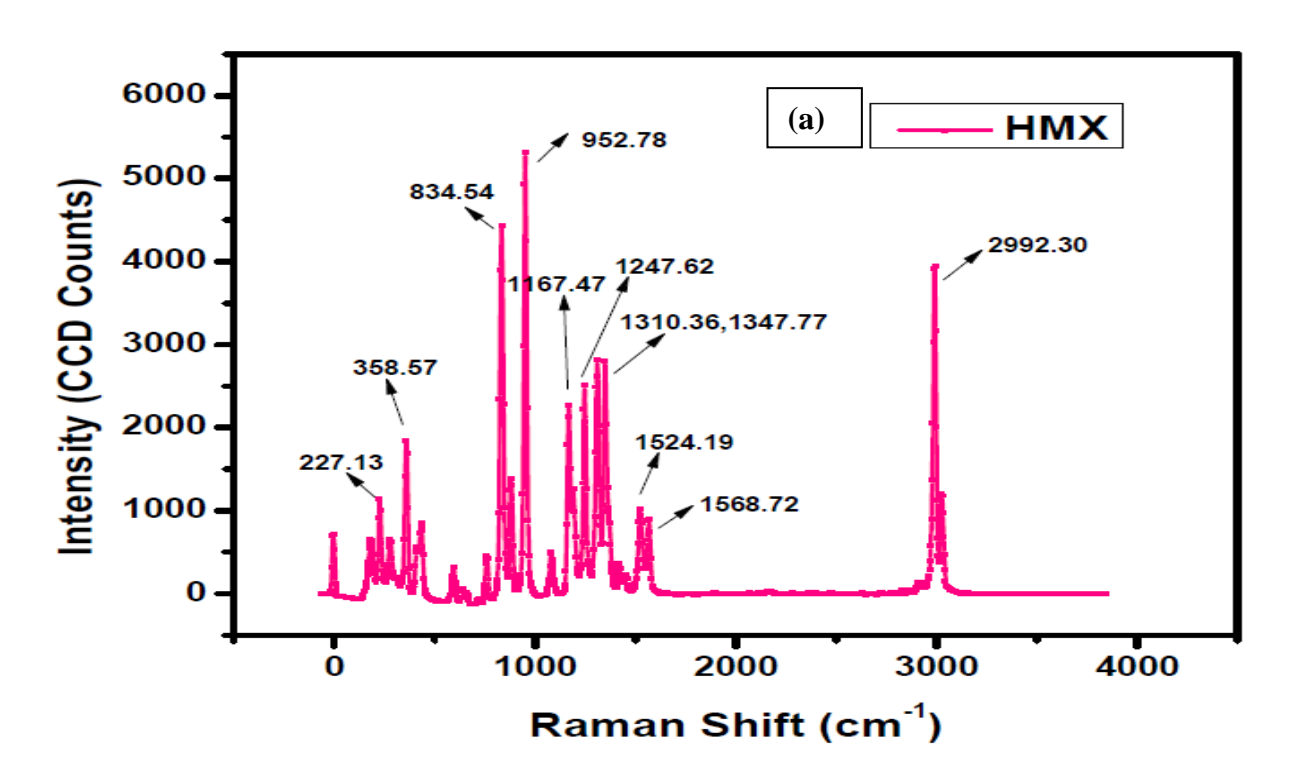
Figure 4. 4 The ratio of anti-stokes to stoke the intensity of Raman spectra of RDX and RDX - PEDOT concerning vibration modes.

The graph highlight the interaction of PEDOT with RDX molecule which appears in the form of deviation from the intensity ratio of anti-Stokes to Stokes lines when it moves toward the higher vibration frequency.

In case of the mixture of RDX and PEDOT, the signal intensitywas reduced of the order of 20 times as compared to the signal intensity of pure explosives. This is due to the loss of polar characteristics of the mixture due to the charge transfer mechanism. A negatively charged electron is transferred from RDX molecule to PEDOT which is responsible for rupturing the charge distribution pattern of the mixture. The interaction of positive charge of PEDOT and negative charge in the explosive leads to the reduction of Raman intensity. Also, the same positive charge fills the gap of lone pairs present on the oxygen molecule in NO₂ functional group of RDX. The vibration mode frequency is changed by an amount of $\pm \delta \nu$ which is attributed to specific molecular stretching.

HMX and HMX+PEDOT spectra:

The similar analytical process is repeated for the HMX molecules and HMX +PEDOT mixture and is represented in Figure 4.5, respectively.



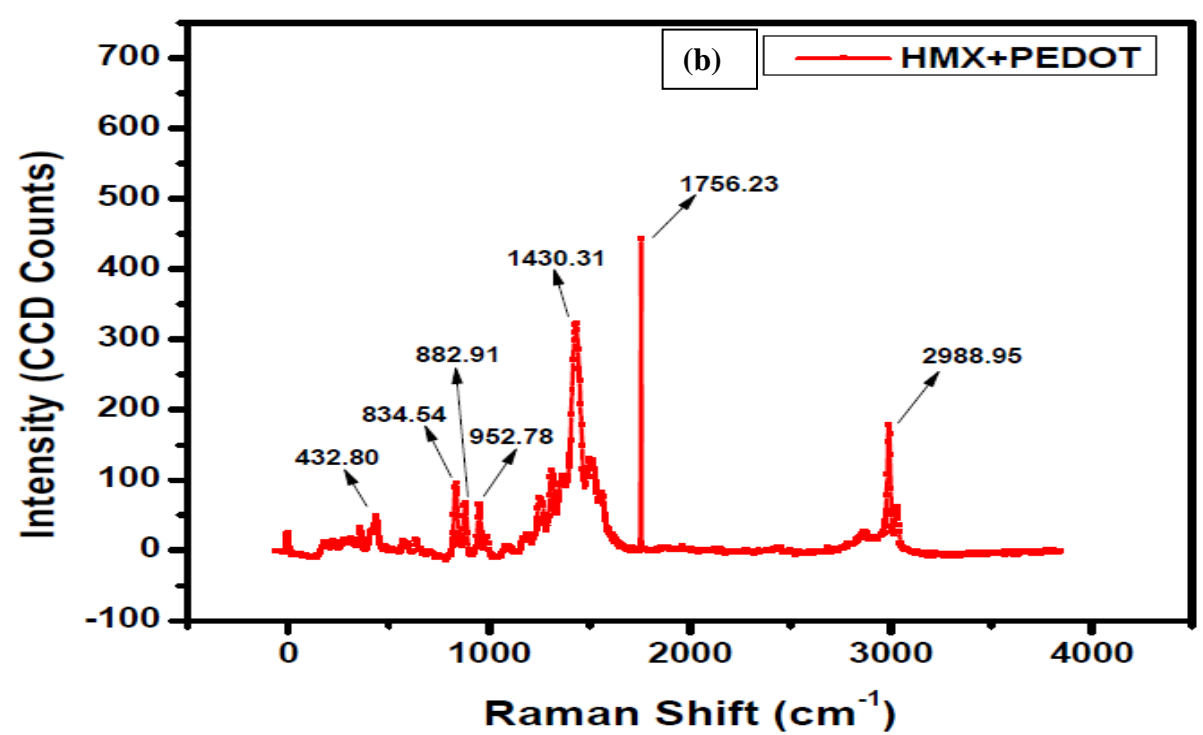


Figure 4. 5 Raman spectra obtained for (a) pristine HMX and (b) PEDOT is mix with HMX.

In the Raman spectrum of pure HMX, the peak at 227.13 cm⁻¹ corresponds to the C-N-C bond stretching and torsion motion. The vibration frequency at 433 cm⁻¹ is due to NO₂ skeletal movement, but it is less prominent as it has low intensity. The Raman peak obtained at 834.54 cm⁻¹ attributes to NO₂ deformation. The most substantial peak observed at 952.78 cm⁻¹ is C-C ring stretching, whereas the vibration frequency at 1078 cm⁻¹ corresponds to C-C stretching. The vibration frequencies at 1167.47 cm⁻¹ and 1247.62 cm⁻¹ are due to C-N-C stretching and the Raman peak at 1310.36 cm⁻¹ corresponds to NO₂ symmetric extension. A peak at 1568.72 cm⁻¹ is due to NO₂ asymmetric stretching. The vibration frequencies at 2992.30 cm⁻¹ and a peak at 3031 cm⁻¹, which has a lesser intensity, are due to CH₂ symmetric and asymmetric stretching.

When PEDOT is mixed with HMX, the intensity of Raman lines is considerably reduced, and different peaks have got shifted between 0.05 cm⁻¹ to 4.83 cm⁻¹ range. The less intense peak at 224 cm⁻¹ corresponds to the C-N-C bond stretching and torsion motion. The vibration frequency at 432.80 cm⁻¹ is due to NO₂ skeletal motion, whereas the Raman peak at 834.54 cm⁻¹ is attributed to NO₂ deformation. The peak observed at 952.78 cm⁻¹ is C-C ring stretching, whereas the vibration frequency at 1083 cm⁻¹ corresponds to C-C stretching and has less intensity. The vibration frequencies at 1164 cm⁻¹, 1430.31 cm⁻¹, and 1251 cm⁻¹ are due to C-N-C stretching, C-H stretching and C-N-C stretching. The Raman peak at 1312 cm⁻¹, which corresponds to NO₂ symmetric stretching and peak at 1566 cm⁻¹, is due to NO₂ asymmetric stretching. The vibration frequencies at 1756.23 are the strongest and correspond to C=O stretch whereas, the peaks at 2988.95 cm⁻¹ and 3029 cm⁻¹ are due to CH₂ symmetric and asymmetric stretching. The most prominent Raman peaks of HMX and HMX+PEDOT are represented in Table 4.4.

Table 4. 4 The peak assignment of pristine HMX and mixed with PEDOT (HMX+PEDOT)

S. No.	Major Raman Peaks for HMX (cm ⁻¹)	Peak Assignment (HMX)	Major Raman Peaks for HMX+PEDOT (cm ⁻¹)	Peak Assignment (HMX+PEDOT)
1.	227.13	C-N-C Bond Stretching	224	C-N-C Bond Stretching
2.	834.54	NO ₂ Skeletal Motion	432.80	NO ₂ Skeletal Motion
3.	952.78	C-C Stretching	834.54	NO ₂ deformations
4.	1167.47,1247.62	C-N-C Stretching	952.78	C-C Ring Stretching
5.	1310.36	NO ₂ Symmetric Stretching	1312.00	NO ₂ Symmetric Stretching
6.	1568.72	NO ₂ Asymmetric Stretching	1756.23	C=O Stretch
7.	2992.30	CH ₂ Symmetric Stretching	2998.00	CH ₂ Symmetric Stretching
8.	3031	CH ₂ Asymmetric Stretching	3029	CH ₂ Asymmetric Stretching

The Raman peaks, intensity, the percentage change in the force constant of corresponding vibration modes of HMX and HMX+PEDOT are comprised in Table 4.5.

Table 4. 5 The NO_2 vibration mode frequency analysis of HMX and it is mixed with PEDOT (HMX-PEDOT)

Raman HMX cm ⁻¹)	Shift HMXPED O T	Differenc e	The rati o of Ra ma n Intensit	HM X IAS/ IS - TN	HM X - PED OT IAS/	Differenc e	% change in the force constan	Assignment
	(cm ⁻¹)	(cm-1)	i es	T	IS - HMX+ PEDO T		t	
433.0	431.94	1.15	17.9	1.18	1.20	0.02	0.53	NO ₂ skeletal
836.4 4	834.38	2.06	42.8	1.37	1.42	0.05	0.49	NO ₂ deformation
1311. 7	1311.705	-0.05	29.0	1.64	1.74	0.10	-0.0076	NO ₂ Symmetric Stretching
1566. 5	1565.4	1.14	19.0	1.81	1.94	0.13	0.14	NO ₂ asymmetric Stretching

PEDOT's effect on HMX is visible in the form of the shift in the ratio of the intensity of anti-stokes to the stokes line, as represented shown in Fig. 4.6.

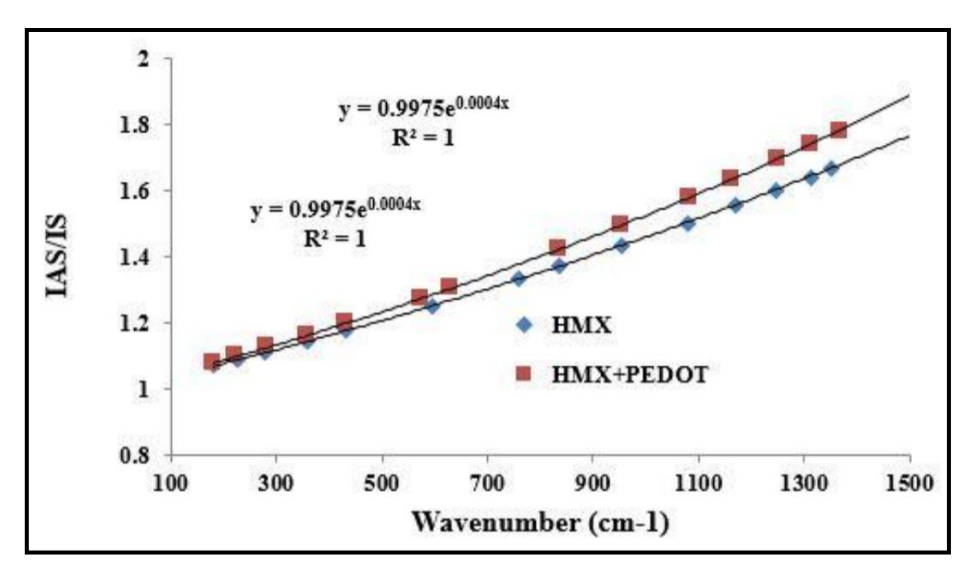
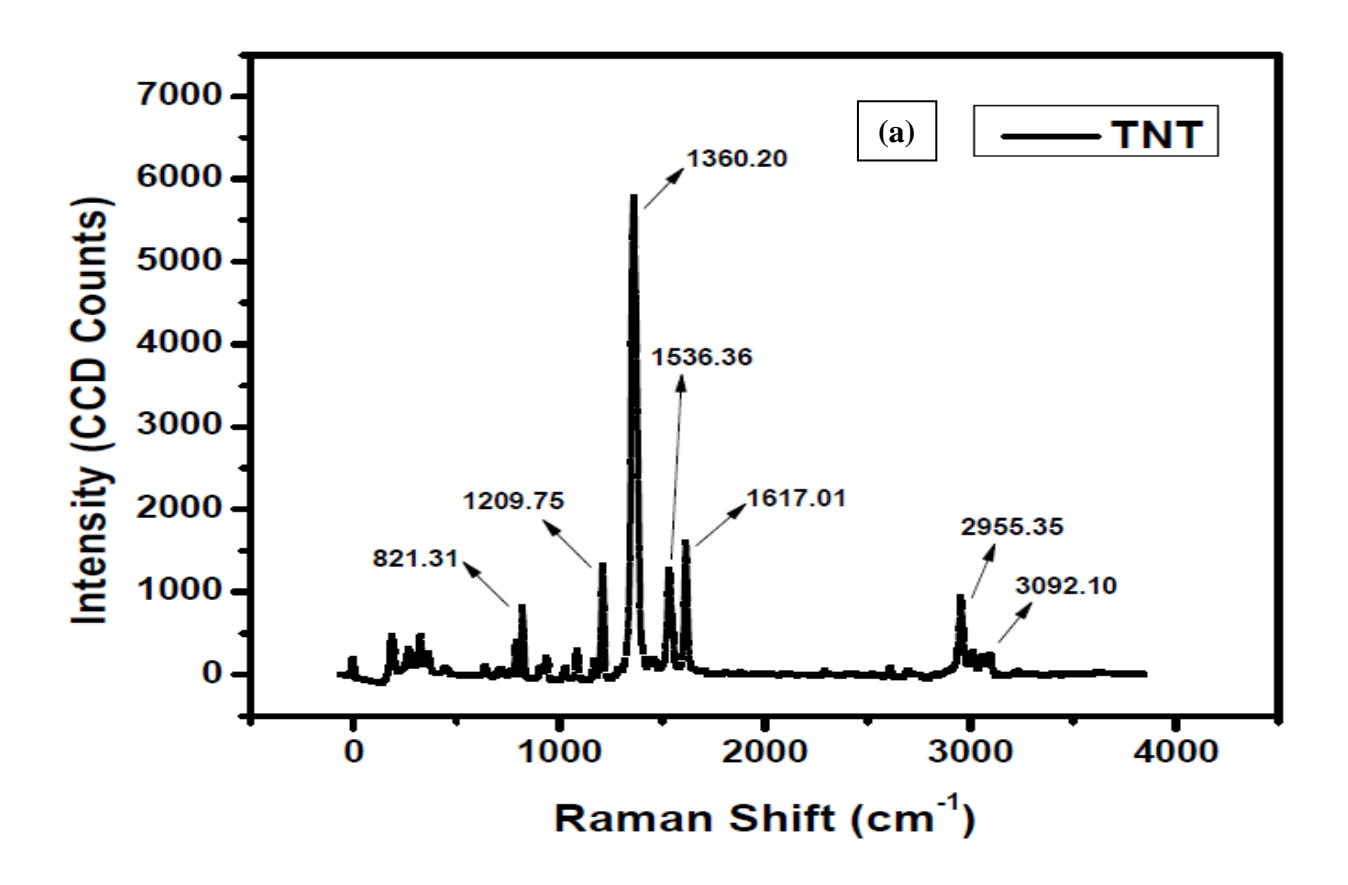


Figure 4. 6 The ratio of anti-stokes to stoke the intensity of Raman spectra of HMX and HMX - PEDOT concerning vibration modes.

The two curves show deviation in the intensity ratio of Anti-Stoke to Stoke lines. It offers more variation toward the higher-order vibration mode.

• TNT and TNT+PEDOT spectrum:

The Raman spectrum of pure TNT and TNT mixed with PEDOT, excited at 532 nm wavelength, is shown in Figure 4.7(a & b).



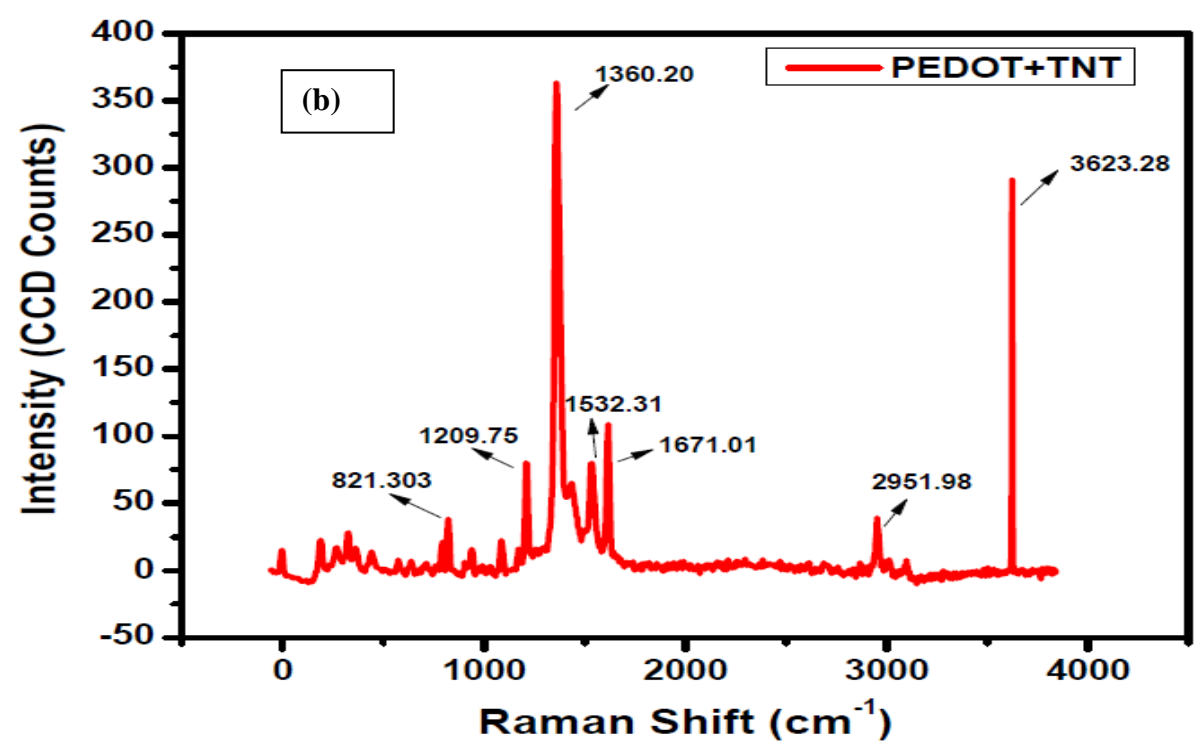


Figure 4. 7 Raman spectra obtained for pristine (a) TNT and (b) TNT and PEDOT.

The TNT molecule structure is an aromatic ring with a methyl group (toluene) attached to it. TNT has three nitro substituents attached to the benzene ring. Many prominent peaks were observed in its Raman spectrum. The band that appears at 325 cm⁻¹ is due to distortion of the vibration mode. Peaks observed at 447 cm⁻¹ and 764 cm⁻¹ correspond to CH₃ wagging and stretching. The nitro-group scissoring mode is assigned to the peak at 821.31 cm⁻¹. The vibration frequency at 1209.75 cm⁻¹ is due to ring breathing. NO₂ symmetric stretching vibration is located at 1360.20 cm⁻¹. The 2, 6-NO₂ asymmetric stretching vibrations are situated at 1617.01 cm⁻¹. The vibration peak at 2955.35 cm⁻¹ corresponds to CH₃ symmetric stretching. Also, the vibration modes analysis of TNT was already reported by Stewart et al. in 1986. The additional Raman active bands assignment was done by Clarkson *et al.* and Wackerbarth*et al.*

The same Raman analysis has been performed for TNT mixed with PEDOT and is shown in fig.4.7. The peaks which correspond to TNT were observed with little shift in the frequency in case of its mixture with PEDOT (TNT+PEDOT) along with a reduction in the intensity. The nitro-group scissoring mode was observed at 821.30 cm⁻¹. The peaks observed at 1360.20 cm⁻¹, 1523.31 cm⁻¹, and 1671.01 cm⁻¹ correspond to NO₂ symmetric stretching, 2,6 NO₂ asymmetric stretching, and 2,4 NO₂ asymmetric stretching, respectively. The peak at 2951.98 cm⁻¹ corresponds to CH₃ symmetric stretching and the O-H stretch is observed at 3623.28 cm⁻¹. The most prominent peaks observed for TNT and TNT+PEDOT are provided in Table 4.6.

Table 4. 6 shows the peak assignment of TNT and TNT+PEDOT

S. No.	Major Raman	Peak	Major Raman	Peak
	Peaks for TNT	Assignment	Peaks for	Assignment
	(- 1)	(TNT)	TNT+PEDOT	(TNT+PEDOT)
	(cm ⁻¹)		(cm ⁻¹)	
1.	821.31	Nitro-group	821.30	Nitro-group
		scissoring mode		scissoring mode
2.	1209.75	Ring breathing	1209.75	Ring breathing
3.	1360.20	NO ₂ Symmetric	1360.20	NO ₂ Symmetric
		Stretching		Stretching
4.	1536.36	2,6 NO ₂	1523.31	2,6 NO ₂
		asymmetric		asymmetric
		Stretching		Stretching
5.	1617.01	2,4 NO ₂	1671.01	2,4 NO ₂
		asymmetric		asymmetric
		Stretching		Stretching
6.	2955.35	CH ₃ Symmetric	2951.98	CH ₃ Symmetric
		Stretching		Stretching
7.	3029.10	C-H Stretch	3623.28	O-H Stretch

The corresponding vibration modes of TNT and TNT+PEDOT are depicted in Table 4.7.

Table 4. 7 The NO₂ vibration mode frequency analysis of TNX and it is mixed with PEDOT (TNT-PEDOT).

Raman	Shift		The rati o of Ra man	TN T IAS/ IS -	TNT + PEDOT IAS/ IS -	Diff. IAS/ IS -	% change in the force	Assignment
TNT (cm ⁻¹)	TNT +PED OT (cm ⁻¹)	Diff. (cm ⁻ 1)	Intensiti es	TNT	TNT+PED OT	TNT+PED OT- IAS/ IS - TNT	constant	
792.67	796.06	3.39	16.10	1.35	1.35	0.0017	-0.86	NO ₂ scissor
820.94	823.12	2.18	20.36	1.365	1.36	0.0011	-0.53	NO ₂ scissors
1360.3	1360.2	0.1	16.68	1.67	1.67	7.89E05	0.015	4, NO ₂ symmetric stretching
1536.6	1534.8	1.8	19.23	1.79	1.79	0.00117	0.234	2, 6-NO ₂ asymmetric stretch
1617.3	1617.9	-0.6	34.5	1.84	1.84	0.0004	-0.074	2, 4-NO ₂ asymmetric stretching

From Fig.4.7, It is clear that some of the CH₃ modes diminish when it is mixed with PEDOT. The ratios of anti-stokes to the Stokes Raman intensities of TNT mixture with PEDOT are evaluated using Eqn. 5. Fig.4.8 shows that both the intensities ratios are overlapping each other, which is a clear cut distinction between HMX and RDX.

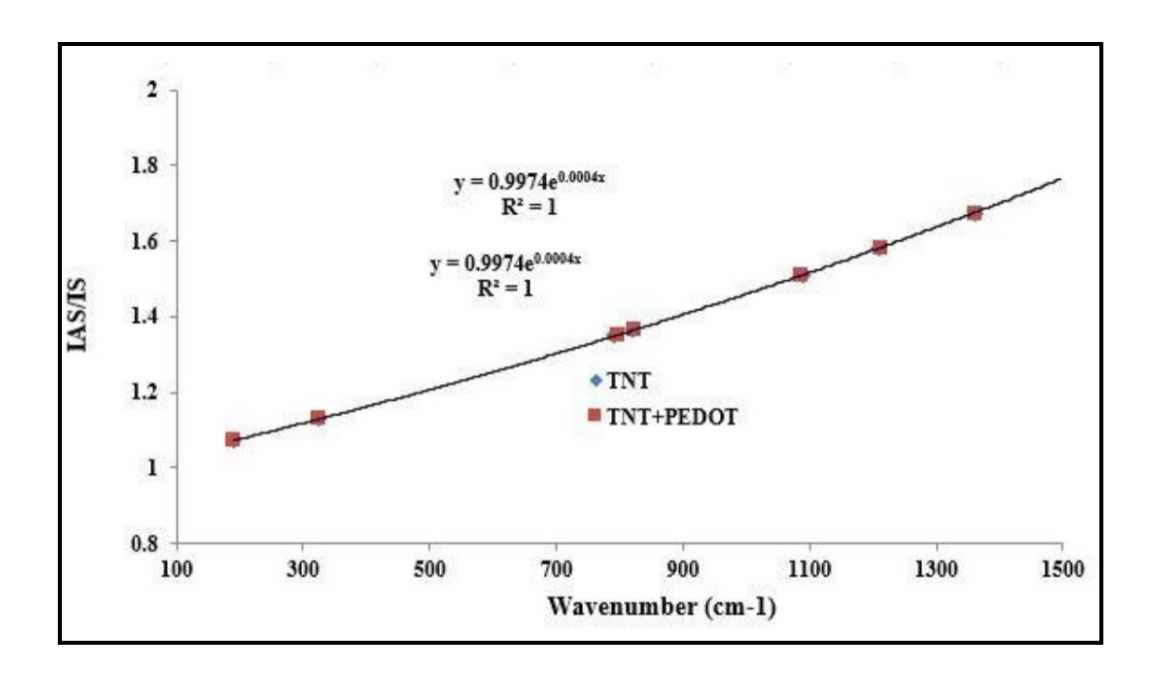
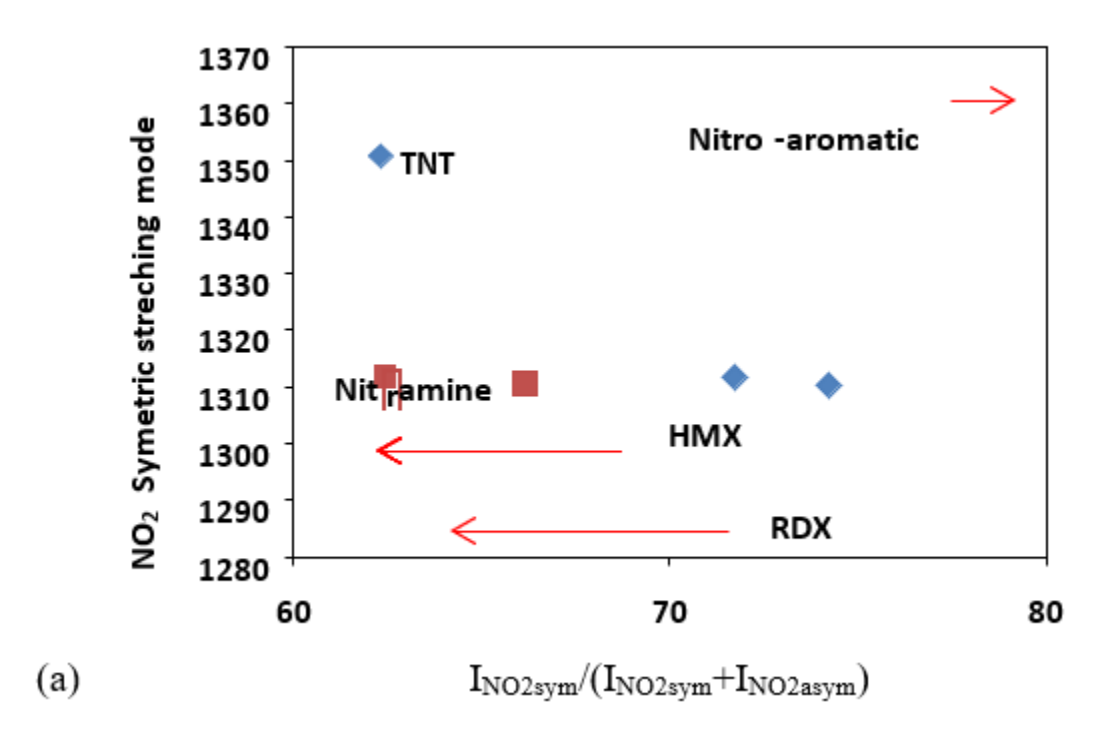
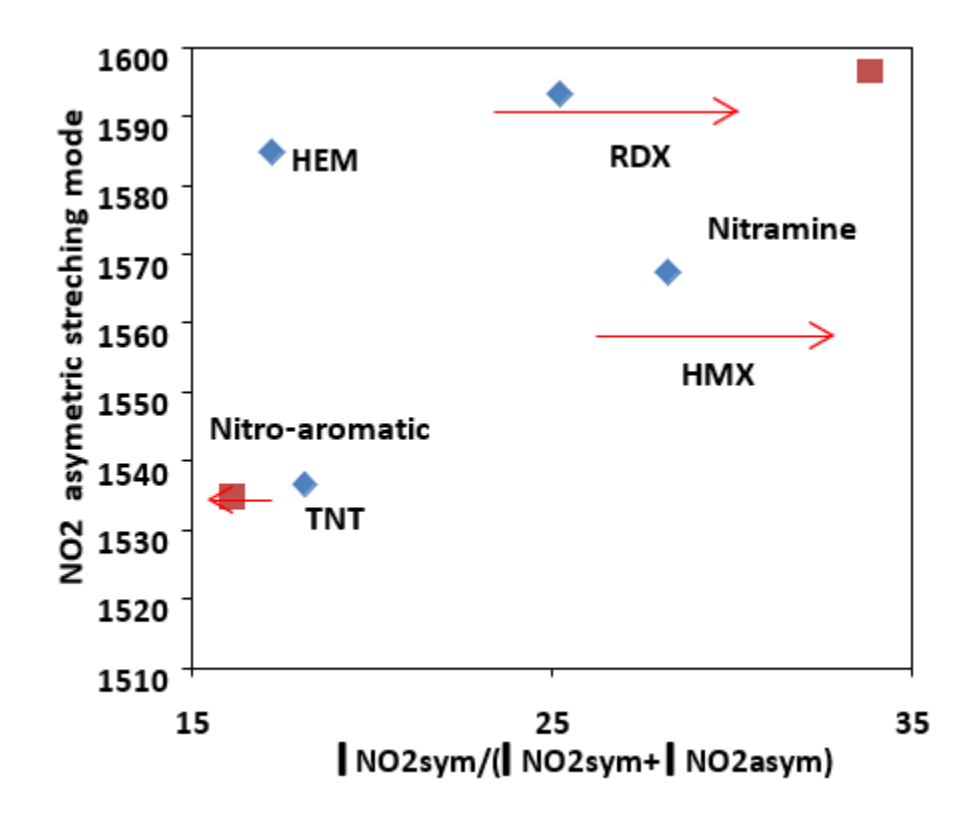


Figure 4. 8 The ratio of anti-stokes to stoke the intensity of Raman spectra of TNT concerning vibration modes.

• Intensity variation of NO₂ in symmetric and asymmetric stretching:

The symmetric NO_2 stretching band is typically very intense and visible, whereas the antisymmetric NO_2 stretching band shows weak Raman intensity, moreover, its position is quite uncertain.





(b)

Figure 4. 9 Intensity variation has been observed for (a) NO₂ symmetric stretch and (b) NO₂ asymmetric stretch of explosives when it is mixed with PEDOT.

• Interaction between PEDOT and the explosives:

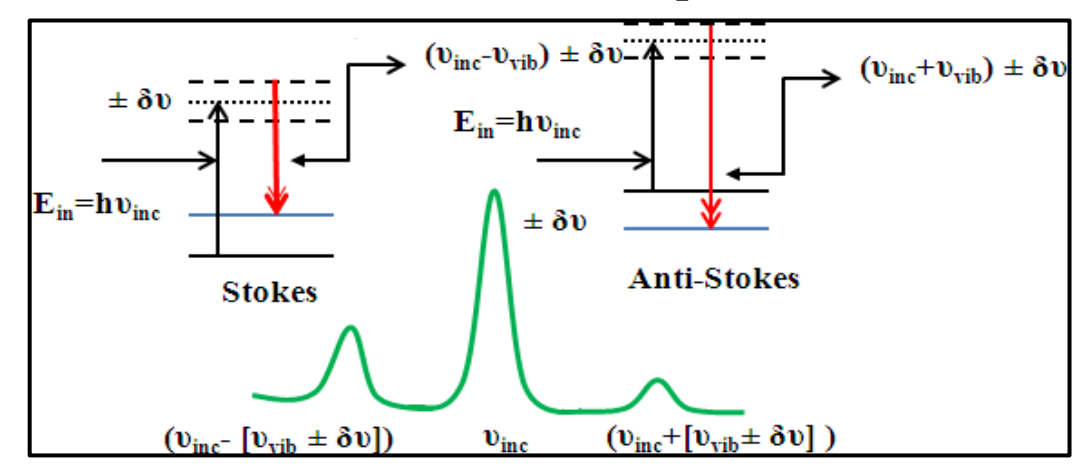


Figure 4. 10 The quantum Energy transitions for Raman Scattering represents the broadening of $\pm \delta \upsilon$ change of frequency at the excited state after mixing PEDOT with explosives

The charge-transfer mechanism is explained in Chapter 3 in detail, as well. Here, the only one-electron

energy level of explosive and PEDOT molecules are taken into consideration, where the distortion due to charge transfer between the positive center present in PEDOT on Sulfur and the lone electrons present on the (-NO₂) groups of explosives leads to an upward shift of the energy by an amount δE for the highest occupied molecular orbital (HOMO) and a similar type of downward shift of δE for LUMO [55]. It is also evident from the coupling constant, which shows a variation (Table 4.3, 4.5, 4.7) for specific NO₂ molecular vibration. Further, the bond's strength can be altered due to the excited electronic transition level, which gets broadened, as shown in Fig. 4.10. This is further explained in Fig.4.11(a).

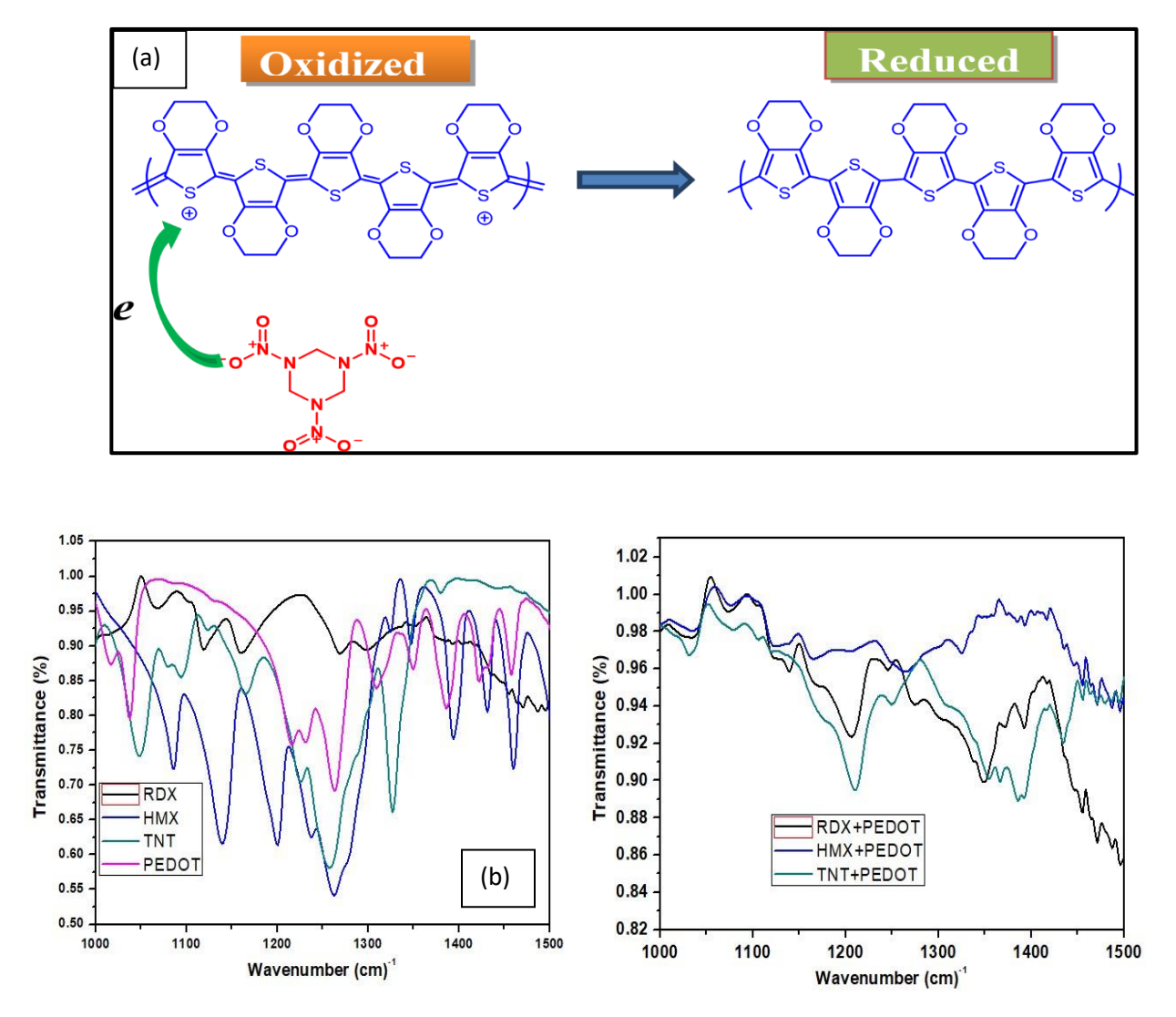


Figure 4. 11 (a) The Schematic representation of molecular interaction of oxidized PEDOT with RDX molecule and (b) shows the shift in the peak of FTIR spectra of explosive molecules when PEDOT is added to them

Sometimes the asymmetric stretching vibration appears in a region where there are other vibrations of similar intensity, as in aromatic ring vibrations for TNT. The nitroaromatic, nitrate ester, and nitramine based explosives show different positions for their symmetric and asymmetric NO₂ bands, fig. 4.9. When explosives were mixed with PEDOT, the NO₂ symmetric stretching modes do not significantly differ if

compared to the NO2 asymmetric stretching mode in terms of the frequency shift, as shown in tables 4.3, 4.5, and 4.7. Some of the prominent differences between the Raman spectra of the nitramines and the spectra of the nitroaromatic explosives when it is mixed with PEDOT are as follows:

- (a) The Raman spectral intensity is significantly changed when the explosive molecules are mixed with PEDOT
- (b) Most of the assigned peaks show the characteristic shift by $\sim 0.5~\text{cm}^{-1}$ to $6~\text{cm}^{-1}$ when PEDOT is mixed with explosive samples and offers a variation in their absorption percentage along with the redshift effect.

This confirms the effect of the charge transfer on the vibrational spectra of the mixture. These transfer of charges between positive charge on the PEDOT polymeric chain and the nitro-groups present on the explosive molecules is also confirmed by the shift in the peaks of FTIR spectra of these molecules as shown in Fig. 4.11 (b, and c).

• Evaluation of Molecular vibration and Force Constant:

In the case of harmonic vibrations, the molecules are considered an array of atoms connected by zeromass springs representing the intramolecular interaction between the particles. Let us assume that the two masses m_1 and m_2 , represent the mass of a diatomic molecule 1 and 2. When the particles are displaced along the x-axis from their equilibrium position, by Δx , and a restoring force F(x) acts on the weight of the particles and is defined using Hooke's law as,

$$F(x) = -C\Delta x \tag{7}$$

Where 'C' is the spring or force constant, representing the rigidity of the spring. It also refers to the strength of the bond between the atoms. The potential energy P is defined as the square of the displacement from the equilibrium position.

$$P = \frac{1}{2}C\Delta x^2 \tag{8}$$

And the kinetic energy K of the oscillating motion of this diatomic molecule can be expressed as

$$K = \frac{1}{2}\mu\Delta x^2 \tag{9}$$

Where µ is the reduced mass given as

$$\mu = \frac{m_1 m_2}{m_1 + m_2} \qquad (10)$$

According to the conservation of energy, K+V must be constant and thus their first partial derivative is equal to zero.

$$0 = \frac{dP}{dt} + \frac{dK}{dt} \tag{11}$$

The Eqn. (11), finally leads to the Newtonian equations of motion

$$\frac{d^2\Delta x}{dt^2} + \frac{c}{u}\Delta x = 0 \tag{12}$$

The Eqn. 12 can be compared to the equation of S.H.M

$$\frac{d^2\Delta x}{dt^2} + \omega^2 \Delta x = 0 \tag{13}$$

$$\omega = \sqrt{\frac{c}{\mu}} \tag{14}$$

The frequency (ω) of the harmonic vibration is directly proportional to the bond's strength and inversely proportional to the masses of the atoms. Here, the reduced mass of the three atoms are treated as the CM of the system by considering the bond length and bond angle between the particles. If we consider three atoms having masses m₁, m₂ and m₃, then the center of mass lies in between these molecules, and the bond angle made by two atoms can be used for the calculation of the reduced mass.

Estimation of reduced mass of NO₂ functional group:

By considering the bond stretching of the molecules in specific direction to be symmetric and as a vector quantity, the distances X_1 , X_2 and X_3 can be evaluated in terms of bond length and bond angle as explained further.

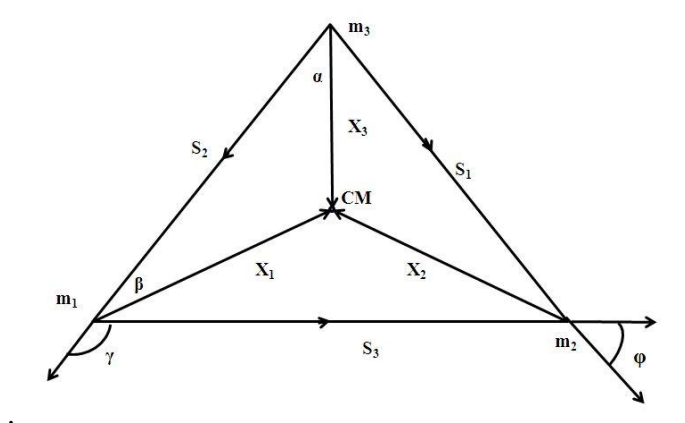


Figure 4. 12 The topology used for the stretching mechanism of three atoms to estimate the reduced mass of the system.

$$X_1 = \sqrt{S_2^2 - \frac{S_3^2}{2} - 2S_2 \frac{S_3}{2}} \cos\gamma \tag{15}$$

$$X_2 = \sqrt{(-S_1)^2 - \frac{S_3^2}{2} + 2S_1 \frac{S_3}{2}} \cos \varphi \tag{16}$$

$$X_3 = \sqrt{(-\frac{S_3}{2})^2} \tag{17}$$

$$I_{CM} = m_1 X_1^2 + m_2 X_2^2 + m_3 X_3^2 (18)$$

$$I_{CM} = m_1 X_1^2 + m_2 X_2^2 + m_3 X_3^2$$

$$R_{CM} = \frac{m_1 X_1 + m_2 X_2 + m_3 X_3}{m_1 + m_2 + m_3}$$
(18)

Hence, the reduced mass is given by

$$\mu = \frac{I_{\text{CM}}}{R_{\text{CM}}^2} \tag{20}$$

This analogy is used for calculating the force constant for particular stretching modes of the Raman signal. In case of asymmetrical stretching, the bond length and bond angle can be varied accordingly, but it is less than the reduced mass of the system.

4.5 Conclusion:

From the results obtained in this chapter, we can observe that the NO_2 symmetric stretching mode of Nitro-aromatic group (TNT) shows a percentage intensity increase of 5% when it is mixed with PEDOT (fig. 7 (a)). However, for the Nitramine group (RDX, HMX), it reduced to < 10%. Also,the TNT molecule's interaction with PEDOT is comparatively less than HMX and RDX. Out of these samples, only the RDX molecule shows the most prominent interaction with PEDOT which is also confirmed by a regression coefficient of $R^2 = 0.9988$. Moreover, in the case of nitramine such as RDX and HMX, the force constant of NO_2 stretching mode is increased when it is mixed with PEDOT. As a result, the period of oscillation decreases. Hence, the resultant complex molecule's total energy increases by δE with a frequency increment of δv , leading to a shift in the frequency mode towards the right side. For TNT, the decrease in force constant can weaken the strength of interaction, with a reduction in the frequency of δv lead to a shift in the frequency mode towards the left side. As compared to TNT, the explosive such as RDX and HMX shows the percentage of change in force constant to be negative, which shows the vibration frequency shift towards the right side when mixed with PEDOT.

In this chapter, we have also successfully analyzed the individual Raman spectra of RDX, TNT, and HMX along with their mixture in the PEDOT polymer matrix using a minimal quantity (one milligram only) of the sample. It helped us to understand the charge transfer mechanism from explosive samples to PEDOT using a Raman spectroscopic technique in solid powder form. This approach can identify the participation of fundamental vibration modes of explosives and their mixture with PEDOT. The study confirms PEDOT interaction with explosives that causes a change in polarizability and broadening of the transition level due to the charge transfer mechanism. Among these explosives, RDX has better interaction efficiency as compared to HMX and TNT. The difference in the ratio of anti-Stokes to the Stokes intensity because of the vibration frequency modes show a good regression coefficient of the order of 0.9988. Finally, the present study opens a new sensing mechanism research channel is physically mixed compounds based on the chemical theory of charge transfer and supported by Pulsed Photoacoustic and FTIR spectroscopy.

References:

- 1. J. S.Caygill, F. Davis, S. P. J Higson, Current trends in explosive detection techniques, Talanta. 88 (2012) 14-29.
- 2. M. López-López, C. García-Ruiz, Infrared and Raman spectroscopy techniques applied to identification of explosives, Trends Analyt. Chem. 54 (2014) 36-44.
- 3. S. Elbasuney, A. F. El-Sherif, Complete spectroscopic picture of concealed explosives: laser induced Raman versus infrared, Trends Analyt. Chem. 85 (2016) 34-41.
- 4. S. Sreedhar, M. A. Kumar, G. M. Kumar, P. P. Kiran, S. P. Tewari, S. V. Rao, Laserinduced breakdown spectroscopy of RDX and HMX with nanosecond, picosecond, and femtosecond pulses, Chemical, Biological, Radiological, Nuclear, and Explosives (CBRNE) Sensing XI, International Society for Optics and Photonics. 7665 (2010) 76650T.
- 5. G. Mogilevsky, L. Borland, M. Brickhouse, A. W. Fountain III, Raman Spectroscopy for Homeland Security Applications, Hindawi Publishing Corporation International Journal of Spectroscopy. 808079 (2012) 1-12.
- 6. M. A. Bañares, G. Mestl, Structural characterization of operating catalysts by Raman spectroscopy, Adv.Catal. 52 (2009) 43-128.
- 7. I. R. Lewis, N. W. Daniel, P. R. Griffiths, Interpretation of Raman spectra of nitrocontaining explosive materials. Part I: Group frequency and structural class membership, Appl. Spectrosc. 51 (1997) 1854-1867.
- 8. Finot, Eric, Thibault Brulé, Padmnabh Rai, Aurélien Griffart, Alexandre Bouhélier, and Thomas Thundat, Raman and photothermal spectroscopies for explosive detection, In Microand Nanotechnology Sensors, Systems, and Applications V, International Society for Optics and Photonics. 8725 (2013) 872528.
- 9. K. S. Rao, A. K. Chaudhary, F. Yehya. Investigation of solid carbon blacks using pulsed photoacoustic and double resonant Raman spectroscopy for the identification of trinitrotoluene, Sens. Actuators B Chem. 231 (2016) 830-836.
- 10. Y. Liu, R. Perkins, Y. Liu, N. Tzeng, Normal mode and experimental analysis of TNT Raman spectrum, Struct .Mol .J. 1133 (2017) 217-225.
- 11. S. Gulia, K. K. Gulati, V. Gambhir, R. Sharma, M. N. Reddy, Trace detection of explosive and their derivatives in stand-off mode using time gated Raman spectroscopy, Vib. Spectrosc. 87 (2016) 207-214.
- 12. I. Ricardo, L. C. Pacheco-Londoño, S. P. Hernández-Rivera, Monitoring the α→β solidsolid phase transition of RDX with Raman spectroscopy: A theoretical and experimental study, J. Mol. Struct. 970 (2010) 51-58.
- 13. P. Jander, R. Noll, Automated detection of fingerprint traces of high explosives using ultraviolet raman spectroscopy, Appl. Spectrosc. 63 (2009) 559-563.
- 14. D. D. Tuschel, A. V. Mikhonin, B. E. Lemoff, S. A. Asher, Deep ultraviolet resonance Raman excitation enables explosives detection, Appl. Spectro. 64 (2010) 425-432.
- 15. K. L. Gares, K. T. Hufziger, S. V. Bykov, S. A. Asher, Review of explosive detection methodologies and the emergence of standoff deep UV resonance Raman, J. Raman Spectro. 47 (2016) 124-141.

- 16. A. Hakonen, P. O. Andersson, M. S. Schmidt, T. Rindzevicius, M. Käll, Explosive and chemical threat detection by surface-enhanced Raman scattering: A review, Anal. Chim. Acta. 893 (2015) 1-13.
- A. K. M. Jamil, E. L. Izake, A. Sivanesan, P. M. Fredericks, Rapid detection of TNT in aqueous media by selective label free surface enhanced Raman spectroscopy, Talanta. 134 (2015) 732-738.
- 18. H. Östmark, M. Nordberg, T. E. Carlsson, Stand-off detection of explosives particles by multispectral imaging Raman spectroscopy, Appl. Opt. 50 (2011) 5592-5599.
- 19. A. Tripathi, E. D. Emmons, P. G. Wilcox, J. A. Guicheteau, D. K. Emge, S. D. Christesen, A. W. Fountain III, Semi-automated detection of trace explosives in fingerprints on strongly interfering surfaces with Raman chemical imaging, Appl. Spectro. 65 (2011) 611619.
- 20. M. R. Almeida, D. N. Correa, J. J. Zacca, L. P. Logrado, R. J. Poppi, Detection of explosives on the surface of banknotes by Raman hyperspectral imaging and independent component analysis, Anal. Chim. Acta. 860 (2015) 15-22.
- 21. J. I. Steinfeld, J. Wormhoudt, Explosives detection: a challenge for physical chemistry, Annu. Rev. Phys. Chem. 49 (1998) 203-232.
- 22. D. S. Moore, S. D. McGrane, Comparative infrared and Raman spectroscopy of energetic polymers, Struct .Mol .J. 661-662 (2003) 561-566.
- 23. R. Blue, Z. Vobecka, P. J. Skabara, D. Uttamchandani, The development of sensors for volatile nitro-containing compounds as models for explosives detection, Sens. Actuators BChem. 176 (2013) 534-542.
- 24. K. Dunst, J. Karczewski, P. Jasiński, Nitrogen dioxide sensing properties of PEDOT films, Sens. Actuators B-Chem. 247 (2017) 108-113.
- 25. Wang, Chao, Tingxiang Jiang, Kang Zhao, Anping Deng, and Jianguo Li. A novel electrochemiluminescent immunoassay for diclofenac using conductive polymer functionalized graphene oxide as labels and gold nanorods as signal enhancers. Talanta 193 (2019): 184-191.
- 26. Jang, Ho-Hyun, Joon-Shik Park, and Bumkyoo Choi. Flexible piezoresistive pulse sensor using biomimetic PDMS mold replicated negatively from shark skin and PEDOT: PSS thin film. Sensors and Actuators A: Physical 286 (2019): 107-114.
- 27. Kang, Tae-Gyu, Jin-Kwan Park, Gi-Ho Yun, Hyang Hee Choi, Hee-Jo Lee, and JongGwan Yook. A real-time humidity sensor based on a microwave oscillator with conducting polymer PEDOT: PSS film. Sensors and Actuators B: Chemical 282 (2019), 145-151.
- 28. Marc Parrilla Maria Cuartero Gaston A.Crespo, wearable potentiometric ion sensors TrAC Trends in Analytical Chemistry, 110, (2019), 303-320.
- 29. Kanchanapally, Rajashekhar, Sudarson Sekhar Sinha, Zhen Fan, Madan Dubey, Eugene Zakar, and Paresh Chandra Ray, Graphene oxide—gold nanocage hybrid platform for trace level identification of nitro explosives using a Raman fingerprint. The Journal of Physical Chemistry C, 118, 13 (2014): 7070-7075.
- 30. Hakonen, Aron, Kaiyu Wu, Michael Stenbæk Schmidt, Per Ola Andersson, Anja Boisen, and Tomas Rindzevicius, Detecting forensic substances using commercially available SERS substrates and handheld Raman spectrometers. Talanta 189 (2018): 649-652.
- 31. J. Yinon, S. Zitrin, Modern methods and applications in analysis of explosives, John Wiley & Sons. (1996).

- 32. P. Tehrani, A. Kanciurzewska, X. Crispin, N. D. Robinson, M. Fahlman, M. Berggren, The effect of pH on the electrochemical over-oxidation in PEDOT: PSS films, Solid State Ion. 177 (2007) 3521-3527.
- 33. M. Horikawa, T. Fujiki, T. Shirosaki, N. Ryu, H. Sakurai, S. Nagaoka, H. Ihara, The development of a highly conductive PEDOT system by doping with partially crystalline sulfated cellulose and its electric conductivity, J. Mater. Chem. C. 3 (2015) 8881-8887.
- 34. Y. H. Kim, C. Sachse, M. L. Machala, C. May, L. M.-Meskamp, K. Leo, Highly Conductive PEDOT: PSS Electrode with Optimized Solvent and Thermal Post-Treatment for ITO-Free Organic Solar Cells, Adv. Funct. Mater. 21 (2011) 1076-1081.
- 35. S. H. Chang, C-H. Chiang, F-S. Kao, C-L. Tien, C-G. Wu, Unraveling the enhanced electrical conductivity of PEDOT: PSS thin films for ITO-free organic photovoltaics, IEEE Photonics. J. 6 (2014) 1-7.
- 36. K. Yasuo, K. Akami, Y. Matsuya, Solid electrolytic capacitor with highly stable conducting polymer as a counter electrode, Synth. Met. 102, (1999) 973-974.
- 37. A. Šutka,., M. Timusk, J. Metsik, J. Ruža, M. Knite, U. Mäeorg, PEDOT electrodes for triboelectric generator devices, Org. Electron. 51 (2017) 446-451.
- 38. G. P. Pandey, A. C. Rastogi, C. R. Westgate, All-solid-state supercapacitors with poly (3, 4-ethylenedioxythiophene)-coated carbon fiber paper electrodes and ionic liquid gel polymer electrolyte, J. Power Sources. 245 (2014) 857-865.
- 39. L. Gomes, A. Branco, T. Moreira, F. Feliciano, C. Pinheiro, C. Costa, Increasing the electrical conductivity of electrochromic PEDOT: PSS films—A comparative study, Sol. Energy Mater Sol. Cells 144 (2016) 631-640.
- 40. W. H. Kim, A. J. Mäkinen, N. Nikolov, R. Shashidhar, H. Kim, Z. H. Kafafi, Molecular organic light-emitting diodes using highly conducting polymers as anodes, Appl. Phys. Lett. 80, (2002) 3844-3846.
- 41. M. Reyes-Reyes, R. López-Sandoval, Optimizing the oxidation level of PEDOT anode in air-PEDOT battery, Org. Electron. 52 (2018) 364-370.
- 42. F. Wang, X. Zhang, Y. Ma, W. Yang, Synthesis of HNTs@PEDOT composites via in situ chemical oxidative polymerization and their application in electrode materials, Appl. Surf. Sci. 427 (2018) 1038-1045.
- 43. J. F. Drillet, R. Dittmeyer, K. Jüttner, Activity and long-term stability of PEDOT as Pt catalyst support for the DMFC anode, J. Appl. Electrochem. 37 (2007) 1219-1226.
- 44. F. Yan, E. P. J. Parrott, X. D. Liu, E. Pickwell-MacPherson, Low-cost and broadband terahertz antireflection coatings based on DMSO-doped PEDOT/PSS, Opt. Lett. 40 (2015) 2886-2889.
- 45. J. Wang, R. S. Karmakar, Y. Lu, C. Huang, K. Wei, Characterization of piezoresistive PEDOT: PSS pressure sensors with inter-digitated and cross-point electrode structures, Sensors. 15 (2015) 818-831.
- 46. N. Trifigny, F. M. Kelly, C. Cochrane, F. Boussu, V. Koncar, D. Soulat, PEDOT:PSSBased Piezo-Resistive Sensors Applied to Reinforcement Glass Fibres for in Situ Measurement during the Composite Material Weaving Process, Sensors 13 (2013) 1074910764.
- 47. Y. Seekaew, S. Lokavee, D. Phokharatkul, A. Wisitsoraat, T. Kerdcharoen, C. Wongchoosuk, Low-cost and flexible printed graphene–PEDOT: PSS gas sensor for ammonia detection, Org. Electron. 15, (2014) 2971-2981.

- 48. S. Taccola, F. Greco, A. Zucca, C. Innocenti, C. J. Fernández, G. Campo, C. Sangregorio, B. Mazzolai, V. Mattoli, Characterization of free-standing PEDOT: PSS/iron oxide nanoparticle composite thin films and application as conformable humidity sensors, ACS Appl. Mater. Interfaces.5 (2013) 6324-6332.
- 49. P. M. Norris, A. P. Caffrey, R. J. Stevens, Femtosecond pump–probe nondestructive examination of materials, Rev. Sci. Instrum. 74 (2003) 400-406.
- 50. J. L. Bredas, G. B. Street, Polarons, bipolarons, and solitons in conducting polymers, Acc. Chem. Res 18 (1985) 309-315.
- 51. B. K. Sikder, A step towards the processability of insoluble or partially soluble functional and structural variants of polymers based on 3,4-alkylenedioxythiophene, RSC Adv.6 (2016) 107776-107784.
- 52. S. Garreau, G. Louarn, J. P. Buisson, G. Froyer, S. Lefrant, In Situ Spectroelectrochemical Raman studies of poly(3,4-ethylenedioxythiophene)(PEDT), Macromolecules. 32 (1999) 6807-6812.
- 53. M. Horikawa, T. Fujiki, T. Shirosaki, N. Ryu, H. Sakurai, S. Nagaoka, H. Ihara, The development of a highly conductive PEDOT system by doping with partially crystalline sulfated cellulose and its electric conductivity, J. Mater. Chem. C. 3 (2015) 8881-8887.
- 54. C. S. Casari, A. L. Bassi, A. Baserga, L. Ravagnan, P. Piseri, C. Lenardi, M. Tommasini, A. Milani, D. Fazzi, C. E. Bottani, P. Milani, Low-frequency modes in the Raman spectrum of sp-sp² nanostructured carbon, Phys. Rev. B 77, 19 (2008) 195444.
- 55. I-M. Chou, Calibration of Raman shifts of cyclohexane for quantitative analyses of methane in natural and synthetic fluid inclusions. J. Raman Spect. 46 (2015) 987-988.
- 56. J. J. P. Stewart, S. R. Bosco, W. R. Carper, Vibrational spectra of 2, 4, 6 trinitrotoluene and its isotopically substituted analogues, Spectrochim. Acta A. Mol Spect. 42 (1986) 13-21.
- 57. J. Clarkson, E. Smith, D. N. Batchelder, A. M. Coats, A theoretical study of the structure and vibrations of 2, 4, 6-trinitrotolune, J. Mol. Str. 648 (2003) 203-214.
- 58. H. Wackerbarth, L. Gundrum, C. Salb, K. Christou, W. Viöl, Challenge of false alarms in nitroaromatic explosive detection device based on surface-enhanced Raman spectroscopy, Appl. Opt. 49 (2010) 4367-4371.

Chapter: 5

Study of temperature-dependent non-linear absorption properties of CdTe crystal during the Process of THz generation and time-domain Spectroscopy of antibiotic Cefixime medicine

5.1 Abstract:

In this chapter, we have studied the temperature-dependent non-linear absorption properties of CdTe crystal used for THz generation in the range of 1-3 THz along with studying its temperature-dependent properties like absorption induced by femtosecond laser pulses in the temperature range of 300-408 K. The Ti: Sapphire laser used as a source is tunable in the range of 650-1180 nm with the central wavelength at 800 nm. The temperature-dependent study was carried out in the improvised temperature tuned spectrophotometer (500-1500 nm) and temperature wavelength tuned femtoseconds laser-based spectrometer. Using theoretical and experimental results, we have established the role of temperature and refractive index properties, along with the damage threshold of CdTe crystal. The generated THz-TDS is also used to investigate one of the popular antibiotic drugs, Cefixime, obtained from different pharmaceutical companies to ascertain its absorbance and quality assessment. The refractive index, absorption coefficient, and absorbance strength of this drug in the THz domain were evaluated. The obtained results provide the chemical composition and effect of other ingredients on Cefixime's signature peak and help distinguish between different polymorphs of similar drugs. The Raman spectroscopy further confirms this variation. An extension of THz to THz-Raman is also examined to facilitate the study of molecules that vibrate at very low frequencies.

5.2 Introduction:

The terahertz (THz) frequency lies in the spectral region between 0.1 THz and 10 THz and bridges the gap between microwave and infrared (optical) regions of the electromagnetic spectra. The word 'tera' means 'multiply by 10¹²'in the metric system. Though the THz frequency is low powered and highly absorbed by the water molecule, it still has many advantages over other spectral bands. Therefore, it is used for different types of applications, such as detecting explosives and contraband drugs for defense and homeland security, imaging of biological tissues, the study of water mechanism and harmful chemicals in fruits and vegetables, freshness of edible items, etc. [1-4]. Table 5.1 provides the comparison of conversion of THz frequency in the visible and IR region.

Table 5. 1 Comparsion of conversion of THz frequency in the visible and IR region

(0.1-10) THz range	(400-700) nm Visible range	(0.7 μm-1mm) IR range
Radiation at 1 THz has a time-	In the Visible region, the photon	Photon energy at 700 nm is
period of 1 picosecond (ps).	energy at 400 nm is,	0.28 eV.
$\lambda = \frac{c}{v} = 300 \mu m$	$E = h\nu = h\frac{c}{\lambda}$	$E = hv = h\frac{c}{\lambda}$
c is the speed of light, and v is	$= 7.875 * 10^{-20} J$	$=4.517*10^{-20}J$
its frequency.	$= 0.49 \ eV$	= 0.28 eV
Wavenumber,	Thus, $E=0.49eV$.	Thus, <i>E=0.28eV</i> .
$K = \frac{k}{2\pi} = \frac{1}{\lambda} = 33.33 \ cm^{-1}$		
Photon Energy,		
E = hv = 4.1 meV, at 1 THz,		
and it is 6.5 meV at 10 THz.		
where h is the Plank's		
Constant.		

The photon energy of THz frequency is ~ 4.1 meV, which is significantly very less ($< 10^3$ order) as compared to the visible and near IR photons (which is an order of eV). Hence, it becomes highly improbable for the sample to get ionized or decomposed due to THz radiation's low energy photons. This region is also referred to as the 'terahertz gap.' The investigation of a wide range of weak spectroscopic interactions occurring in this range is a challenging task due to the source's low power. The low photon energy of THz responds to the low-frequency dielectric relaxation, rotational and vibrational transitions of molecules and molecular torsions, and THz spectroscopy provides a link infrared and microwave spectroscopy. Therefore, it works as a versatile tool in supramolecular chemistry, drug analysis, X-ray diffraction (XRD), and solid-state NMR (ssNMR) [3].

Unlike Raman and Infrared spectroscopy, the techniques used to generate and detect terahertz radiation are new and will go through many new developments. Over the last three decades, significant advancement has been done in the field of THz technology. Various sources of generation of THz have also been established. Some of the most commonly used are nonlinear crystals, semiconductors, Photoconductive (PC) antennas, and optical rectification processes [5-12]. In this chapter, we have focused on nonlinear absorption properties of femtoseconds pulses in Cadmium Telluride (CdTe) during the THz generation process. We have also analyzed the various polymorphs of the drug sample Cefixime using terahertz spectroscopy and extended the results obtained to THz-Raman spectroscopy. However, before trying to generate THz from the nonlinear crystal, CdTe, we have studied its linear and nonlinear temperature-based properties such as its transmission, absorption, and refractive index in both UV-Vis-NIR region and the ultrafast region using femtosecond laser from Cameleon Ti: Sapphire Laser at 80 MHz repetition rate [13]. CdTe crystal, which belongs to the Group II-VI semiconductor materials, possesses excellent optical properties and high electro-optical (4.5 pm/V and nonlinear coefficient (81.8pm/V) suitable for the generation of THz. Besides, it possesses strong absorption in the visible region [14-16]. This crystal can be used for the fabrication of optoelectronic devices and photovoltaic cells as well.

For the detection of the THz generated from the crystal, we have employed a Low Temperature-GaAs-based Photoconductive (PC) antenna. A photoconductive antenna is a modified version of the Schottky diode. It is composed of a high resistive semiconductor, which shows conductivity under photons (photoconductor), and gold metal plates, which also works as an electrode. The schematic design is shown in Fig. 5.1(a). Also, GaAs, InP, and radiation-damaged silicon wafers are used in antenna fabrication. Antenna structure has the provision of applying a bias voltage to create a strong electric field in the PC antenna gap, as shown in Fig.5.1(b). The process of detection with the help of a PC antenna is known as PC sampling.

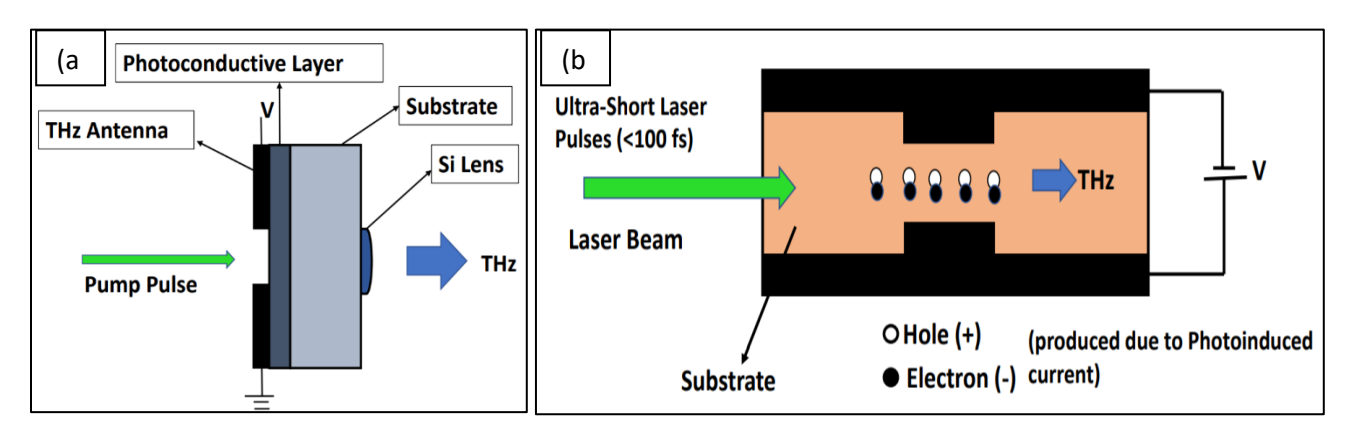


Figure 5. 1 (a) represents the side-view of a photoconductive (PC) antenna and (b) shows the basic working principle of a PC antenna

We have studied the temperature-dependent properties of CdTe crystal using a modified spectrometer, which is explained in the upcoming sections of this chapter. We have further used the time-domain terahertz spectroscopy to study the spectral and optical properties of commonly used antibiotic drugs; Cefixime and its various polymorphs obtained from different pharmaceuticals, which is used for curing bacterial infections.

The chapter consists of two sections: Section 1 comprises the study of temperature-dependent linear and nonlinear transmission and absorption properties of CdTe crystal in the temperature range between 300-408K range using tunable 780-970 nm wavelengths of 140 fs duration at 80 MHz repetition rate obtained from Ti: Sapphire laser. The same laser pulses were employed for THz generation from CdTe the crystal. Section 2 deals with a time-domain THz spectroscopy application to study and analyze the various polymorphs present in the Cefixime drug. The results obtained in this case are further extended to Raman spectroscopy. Since the stokes lines of Raman spectra can be extended up to FIR spectral range, therefore, an extension of the THz spectral range overlaps the considerable part of Raman spectra.

Section: 1

Temperature-dependent Study of linear/nonlinear absorption Properties of CdTeCrystal:

5.3 Experimental Details:

The experimental details of this chapter are given in Appendix B.

For the measurement of temperature based transmission properties of CdTe crystal using femtoseconds laser, the crystal was placed in an oven coupled with the indigenously designed temperature controller. The temperature is manually tuned in regular intervals at seven kelvin per minute between 298-473 K. The linear transmission of the crystal was evaluated using Lambda 650 spectrophotometer (Fig. 5.2(b)) which has enabled us to measure the transmittance data of the same CdTe crystal between 500-1500 nm.

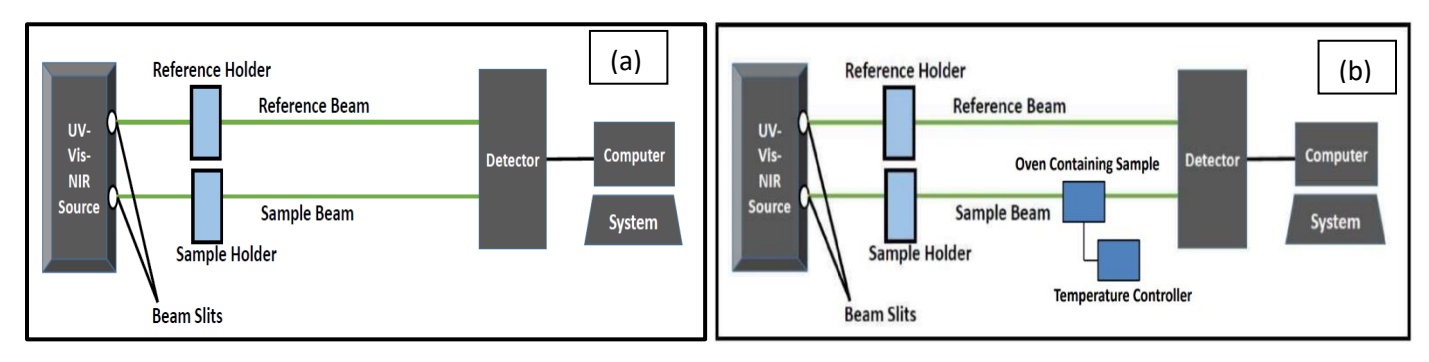


Figure 5. 2 (a) UV-Vis-NIR Lambda 650 spectrophotometer and (b) modified spectrometer with the introduction of the oven with temperature controller

5.4 Results and Discussion:

When femtosecond laser beam tunable between at 750 nm, 800 nm and 970 nm wavelengths obtained from a Ti: Sapphire laser was made to incident upon the CdTe crystal, it was observed that the transmission for two wavelengths; i.e., 750 nm and 800nm are very near to each other at 11.68% which becomes 0.18% at higher temperature and 12.60%; respectively, whereas in the case of wavelength 970

nm, it is around 47.12% as shown in fig. 5.3. This is much higher as compared to 750 and 800 nm wavelength.

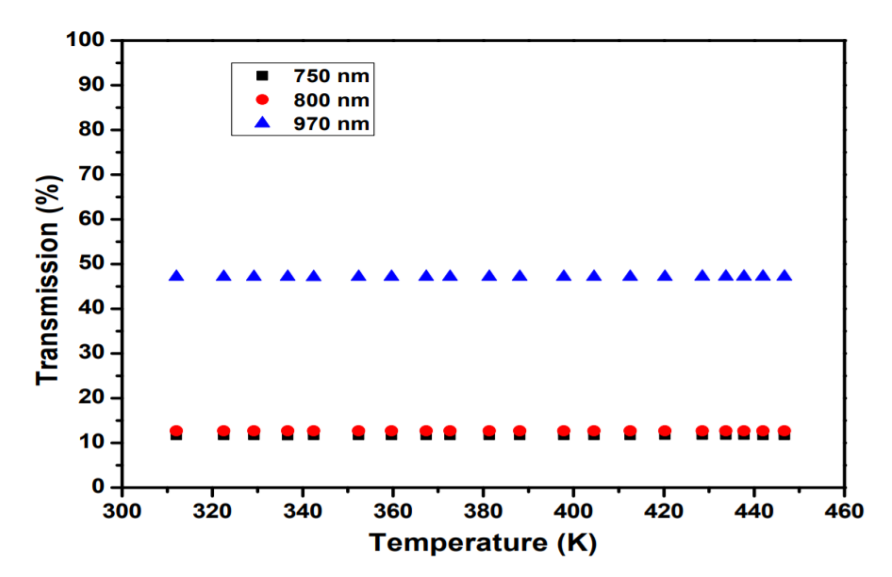


Figure 5. 3 The nonlinear transmission of CdTe using femtosecond laser pulses at different wavelengths

To estimate the transmittance of the CdTe [17], we have recorded the intensity of the incident beam at 750, 800, and 970 nm keeping the temperature constant at room temperature. The intensity of the light beam passing through the crystal at a particular wavelength without the sample is considered as the reference beam, $I_R(h\vartheta)$ and the intensity of light at the same wavelengths passing through the sample placed in the sample holder inside the temperature- controller unit at a different temperature, $I_S(h\vartheta)$ is the sample intensity which is also recorded.

Thus, the percentage of transmission T (h θ) is given as:

$$T(h\vartheta) = \frac{I_S(h\vartheta)}{I_B(h\vartheta)} \tag{1}$$

From Fig. 5.3, it is observed that the transmission at 750 nm and 800 nm is around 11%, which approaches zero at higher temperatures, whereas in the case of 970 nm, it is approximately 47%. This discrepancy is attributed to the induced nonlinearity in the crystal when it is subjected to femtosecond pulses. The transmission of the same crystal in the UV-Vis-NIR domain is shown in Fig. 5.4 (a). It is evident from this graph that the transmission remains approximately zero up to 850 nm, and then it suddenly increases to 67.4% at 858 nm from where it shows saturation up to 1500 nm. Fig. 5.4 (b) shows the variation of transmission with respect to temperature. The transmission decreases with an increase in temperature. Still, a peak is observed at 380 K, followed by a dip at 390 K and another peak at 400 K. Here, transmission decreases, and at 408 K, the transmission was almost zero. Thus, we can conclude that CdTe crystal becomes opaque at 408 K and beyond.

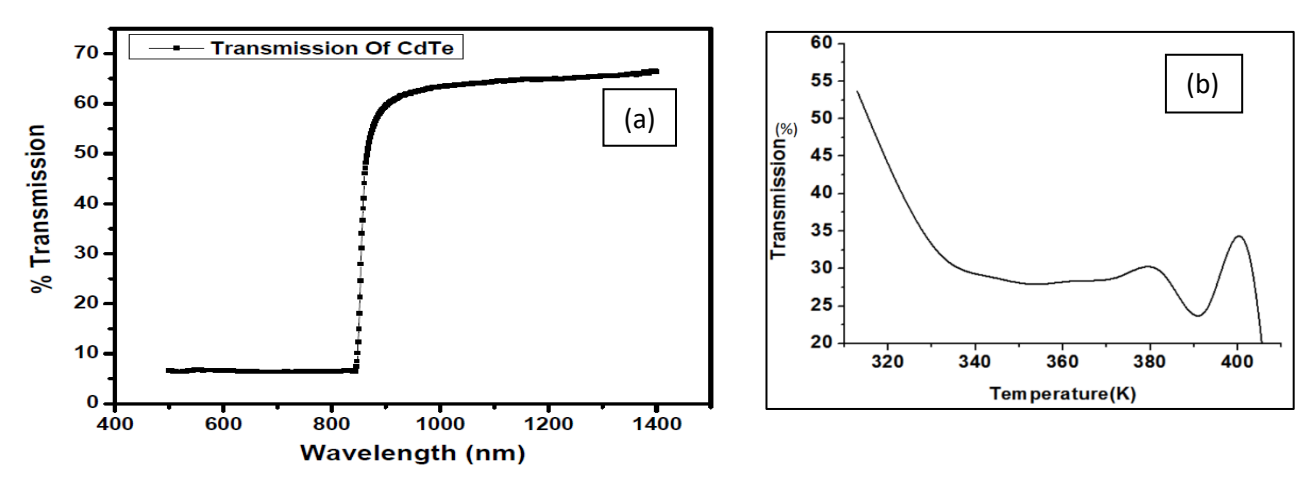


Figure 5. 4 (a & b) shows the variation of transmission of CdTe with respect to Wavelength and temperature when subjected to UV-Vis-NIR spectrometer

• Bandgap Energy of CdTe:

CdTe has numerous applications in various fields and has been a subject of extensive research for several decades. It shows a considerable variation in the bandgap energy (Eg) at room temperature lying in the range lies 1.37-1.54 eV range. This variation is observed due to various characterization techniques such as absorption and photoreflectance. The energy, Eg, is estimated by fitting the experimental points to a theoretical model given by the M-W equation, in which Eg is a fitting parameter. In photoluminescence (PL), Eg is calculated from an extrapolation technique due to the weak PL emission at room temperature. Another reason for the dispersion in the Eg data is the incorrect use of the Varshni equation to describe the temperature dependence Eg(T); since this equation is valid only for IV and III–V semiconductors.

The energy bandgap (Eg) of CdTe crystal as a function of temperature is expressed in equation (2), also known as M-W equation [18]:

$$E_g = 1.60657 - 5 * 10E(-5) * T - 3.29 * 1E(-2) * \left(\coth\left(\frac{91.5}{T}\right) - 1\right)$$
 (2)

The first term of the equation is the initial energy at 4 K, the second term represents the lattice thermal vibrations, and the third term corresponds to phonon-phonon interaction. With an increase in temperature, we observe a shift in the energy that also gets reflected in the case of femtosecond laser pulses as a discrepancy in the transmission of the same crystal at different wavelengths. This phenomenon concludes that there is a nonlinear absorption of light in the CdTe crystal. This energy shift also shows that all the energy is not utilized to generate THz, but some energy is lost while heating the crystal to bring it to a specific temperature. The same crystal is subjected to an improvised version of temperature tuned spectrophotometer (Lambda 650) for linear transmission/absorption study. The temperature of the crystal was adjusted from room temperature to 473 K. The transmission curves are shown in Fig 5.5 (a). The expression in equation (2) matches the accepted literature value of E_g at 4.2K [19], and hence, it can be used at room temperature as well, fig. 5.5 (b).

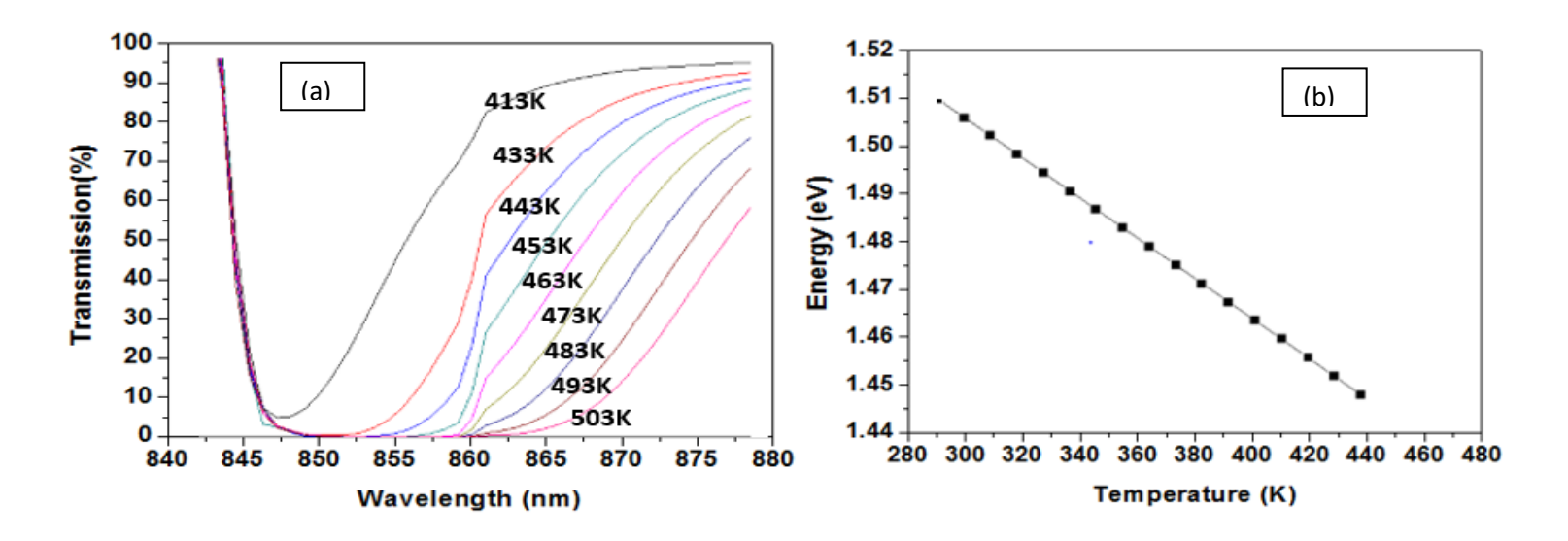


Figure 5. 5 (a) Transmission vs. wavelength for CdTe at different temperatures and (b) Temperature vs. Energy of CdTe given by M-W equation.

Estimation of Refractive Index and Absorption Coefficients of CdTe:

To estimate the absorption coefficient of CdTe, we have used the same procedure as in [20,21]. The absorption coefficient increases for all the considered wavelengths with increasing temperature, as shown in Fig. 5.6 (a). The refractive index in the range 800-1400 nm (0.8-1.4 μ m) shows approximate linearity with increasing photon energy, as shown in Fig. 5.6 (b).

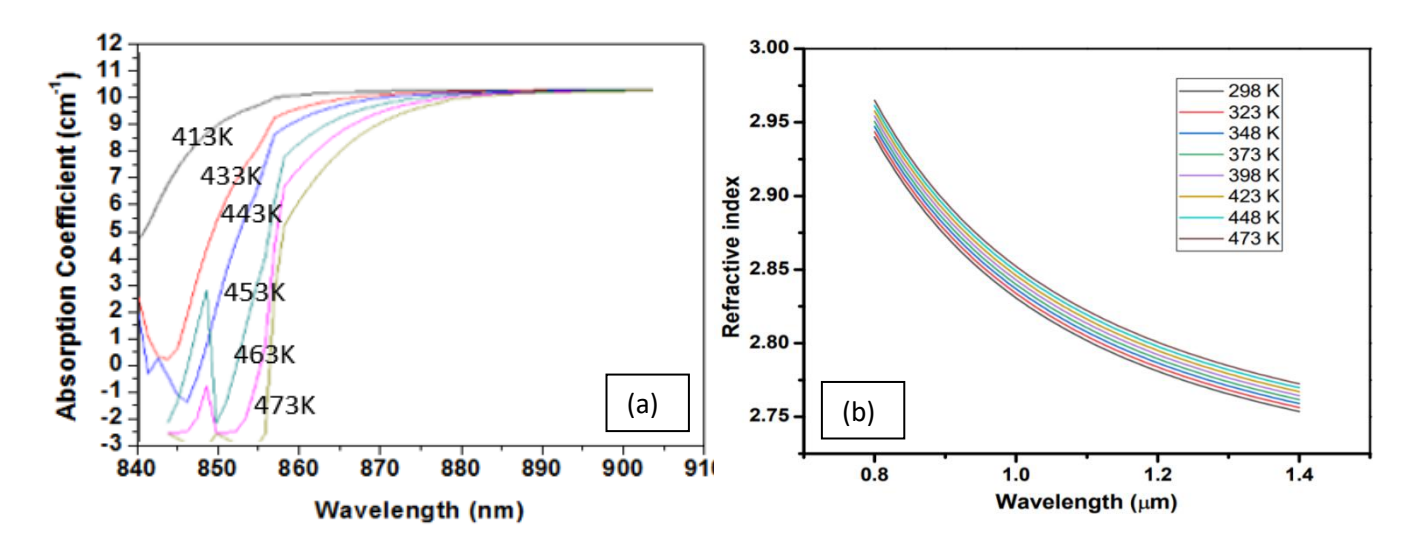


Figure 5. 6 Physical properties of CdTe: (a)Absorption Coefficient and (b) refractive index

The absorption edge shows a spread with an increase in wavelength, which could be due to two reasons (i) increase in phonon population with respect to change in the temperature, or (ii) Effect of temperature on impurities/defects and change in concentration of electrons and holes in the conduction and valence bands. Fig. 5.6 (b) represents the refractive index's variation with respect to the wavelength at different temperatures. This knowledge is crucial for the optical designing of the materials. Harvey and Wolfe have also studied the effect of temperature on the refractive index. [22]. We have estimated the refractive index

in both optical (n_{opt}) and terahertz domain (n_{tera}) , as it further helps estimate the coherence length of the crystal. The expression used for examining the above parameters for the crystal is given below.

$$n^{2} - 1 = \frac{6.1977889\lambda^{2}}{\lambda^{2} - 0.1005326} + \frac{3.2243821\lambda^{2}}{\lambda^{2} - 5279.518} ; (in optical domain)$$
 (3)

$$n^{2} = 3.7582 + \frac{3.4612\lambda^{2}}{\lambda^{2} - 0.1866} + \frac{6.2926\lambda^{2}}{\lambda^{2} - 9352.0} (in THz)$$
(4)

• Measurement of Coherence length and Damage Threshold:

The coherence length of a crystal is defined as:

$$lc = \frac{\lambda}{2|n_{opt} - n_{tera}|}\tag{5}$$

The crystal's coherence length at considered wavelengths; 800, 850, and 900 nm are comprised in Table 5.2.

Table 5. 2 The crystal's coherence length at considered wavelengths; 800, 850, and 900 nm

S. No.	Wavelength (λ)	n _{opt}	n _{tera}	Coherence
	(nm)			Length (l _c) (mm)
1.	800	2.933	3.2	8.6
2.	850	2.90	3.2	8.2
3.	900	2.87	3.2	7.85

• Generation of THz Radiation using CdTe Crystal:

The experimental arrangement for THz generation from CdTe crystal and detection from the PC antenna is provided in Appendix B. The source of the femtosecond light beam was a Ti: Sapphire laser tunable between 650-1180nm. The pulse duration and repetition rate were fixed at 140 fs and 80 MHz for THz generation. A variable attenuator used in the beam's path helps in regulating the power of the incident beam. The nonlinear crystal, CdTe, was placed in a high precession rotation mount for varying the azimuthal angle with respect to the incident laser beam's polarization. This helps in increasing the amplitude of the generated THz signal. The employed pump and probe powers were 300 and 75 mW, respectively. For detecting the generated THz, we have used PC (photoconductive) sampling with the help of a PC antenna, having a gap of 5 μ m and a length of 20 μ m. The probe beam was focused by using another plano-convex lens of focal length 50 cm. The focused probe beam was allowed to be incident on detecting antenna. The output was fed to low noise current preamplifier connected to the voltage input of a lock-in-Amplifier. The obtained THz pulses are measured in the temporal domain

with respect to probe beam delay, with a time constant of 100 ms in the lock-in amplifier, fig. 5.7.

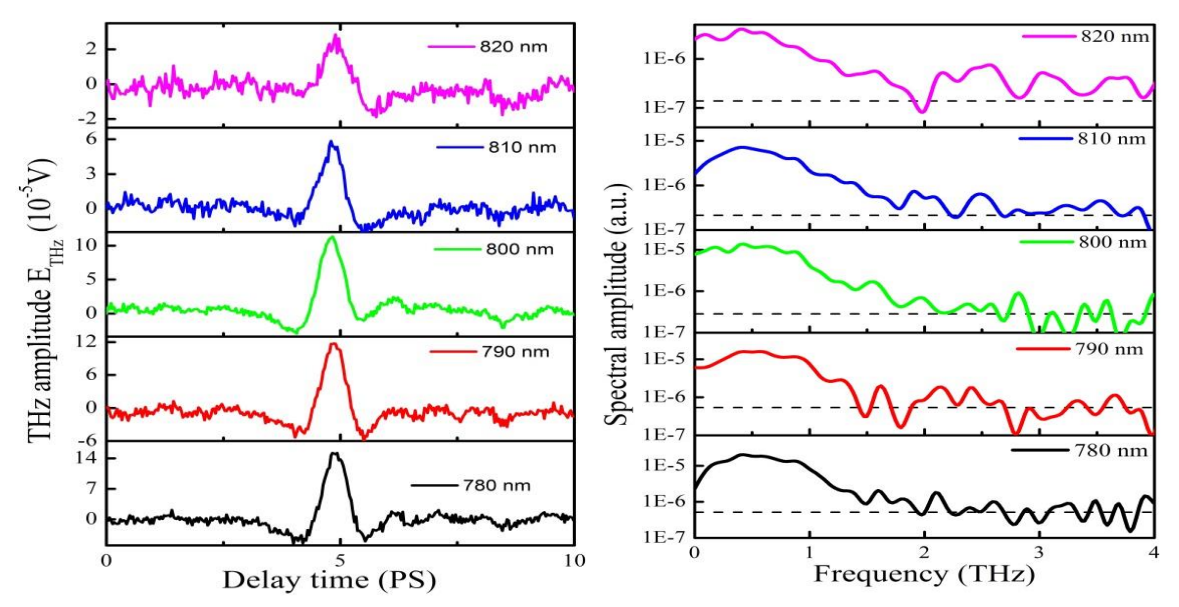


Figure 5. 7 (a &b): the measured THz temporal profiles of <110>CdTe with respect to incident laser central wavelength, which is tunable between 780 to 820 nm at input laser power 300 mW. It shows a variation of THz amplitude with respect to delay time and frequency.

The measured temporal profiles are shown in Fig. 5.7, has full width at half maximum of 0.55 picoseconds and its peak amplitude is decreasing with increasing in incident laser wavelength. Here, the incident photon energy of laser is above the band gap of the CdTe crystal i.e. 1.47 ev. The THz signal amplitude increases with decrease in incident laser wavelength, when incident photon energy is greater than the band gap of semiconductor crystals. This may be attributed to remarkable change of nonlinear susceptibility of CdTe crystal above and near the band gap of material. The spectral amplitude of generated THz radiation from CdTe crystal as a function of incident laser central wavelengths is depicted in figure 5.7(b). The spectral amplitudes of generated THz radiation with 780, 790, 800, 810 and 820 nm are 2.01, 1.56, 1.36, 0.75 and 0.48 a.u., respectively. This implies that the emitted spectral amplitude is decreasing with increase in laser central wavelength. The figure shows that the spectrum of obtained THz radiation is extended up to 2 THz. We observed that the crystal has comparatively lower transmission between 780-820 nm range but provides significant THz transmission between 0.1-1.2 THz. The lower transmission above 1.2 THz range is due to higher absorption coefficient of crystal at room temperature. The effect of incident laser wavelength on generated THz peak amplitude is illustrated in Fig. 5.8(a). The emitted THz peak amplitude with 780, 790, 800, 810 and 820 nm are 15.2, 11.8, 11.3, 5.84 and 2.85 a.u., respectively. These values imply that the incident laser central wavelength affects the generated THz peak amplitude and it is decreasing with increase in laser wavelength. The dependence of THz radiation on incident angle of laser pulses with respect to crystal surface normal is shown in Fig.5.8(b). The emitted THz amplitude with 45° (9.8 a.u.) is high as compared to 0° (0.76 a.u.) angle of incidence. This is due to contribution of excited coherent phonons and optical rectification process in CdTe crystal at 45° incident angle whereas 0° emits radiation via optical rectification process only.

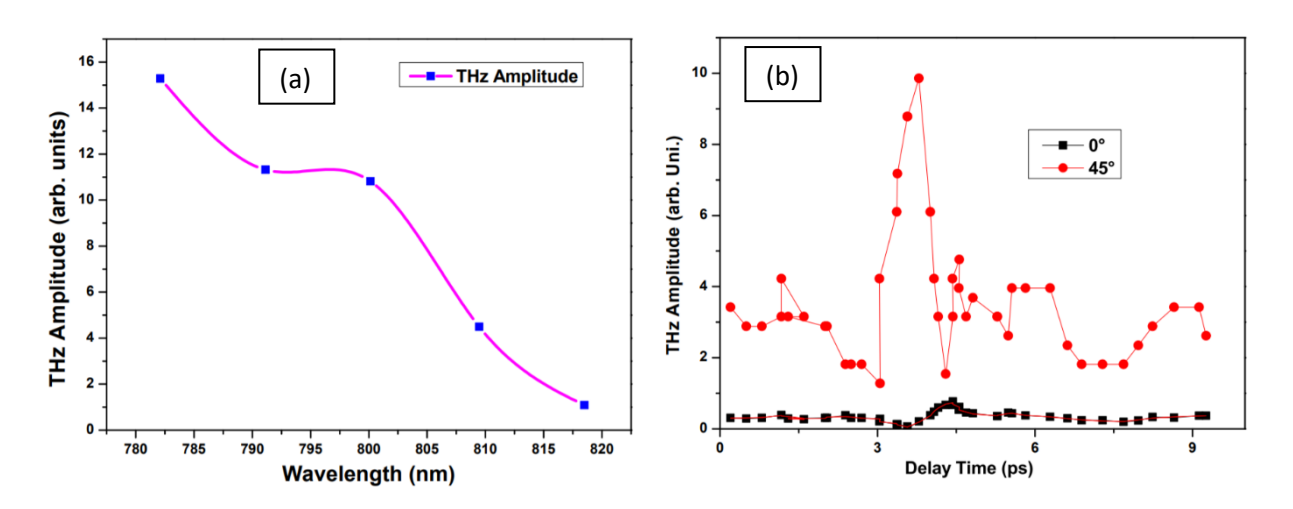


Figure 5. 8 (a) Variation of THz amplitude as a function of wavelength and (b) Dependence of THz radiation on incident angle of laser pulses

Section: 2

Application of Time-domain Terahertz Spectroscopy

Characterization of an antibiotic Cefixime drug and its polymorphs obtained from the different origin along with an assessment of their quality

This section focuses our study on the Cefixime antibiotic tablet, an orally administered cephalosporin with a broad spectrum of antibacterial activity in-vitro.

We have generated THz in the range of 0.1-2 THz in the previous section. We have used the same experimental arrangement to analyze the samples. To prepare the samples for analysis, we have prepared the medicine pallets by mixing it in the PTFE (Teflon) matrix in equal proportion (1:1 ratio). For this purpose, Cefixime samples weighing 200 mg were mixed with 200 mg of PTFE (Teflon) powder and were crushed and ground together using a mortar-pestle [23-26]. It was then thoroughly mixed with 20 ml of CH₃OH solvent and was dried entirely before grinding it again to convert it into a homogenous powder. It was divided into two halves and transferred to a solid stainless-steel die, then subjected to 2 tons of pressure to prepare a pellet. The thickness and diameter of the pellet are maintained at 2 mm and 12mm, respectively. These pallets were then subjected to the THz system, and time-domain spectra were recorded. We have estimated THz-TDS's possibility as an evaluation technique for differentiating between different polymorphs of the same medical tablets in terms of differences in THz and Raman spectroscopy peaks, along with changes in the physical parameters like absorption coefficient and refractive indices. We have further estimated the possibility of extending the THz-study to THz-Raman to study the characteristics of molecules that vibrate at very low frequencies.

5.5 Results and Discussion (Section 2):

• Time-domain THz Spectroscopy:

The THz absorption in the molecular system is dominated by the excitation of intra-molecular and inter-molecular vibrations. The THz spectrum's spectral features depend on the vibration of weak non-covalent bonds like hydrogen or other non-valence bonds. It has a lot of applications in the pharmaceutical field and is used for the analysis of pharmaceutical products as well. Fig. 5.9 (a, b) shows the temporal and spectral air profiles, PTFE (Teflon) and medicine samples in the terahertz range after passing through the pellet. The details of the samples used are provided in Table 5.3.

Table 5. 3 shows the details of the polymorphs of the medicine samples of Cefixime procured from different pharmaceuticals and used for the study in this chapter

S.No.	Sample	Manufacturing	Major	Mass	Molecular	Chemical Formula
		Company	Component	(mg)	Weight	
					(g/mol)	
1.	Cefixime	Cipla	Cefixime	200	453.444	$C_{16}H_{21}N_5O_{10}S_2.H_2O$
	Tablet IP					
2.	Cefixime	Sun	Cefixime	200	453.444	$C_{16}H_{21}N_5O_{10}S_2.H_2O$
	Tablet IP	Pharmaceutical				
		Ind. Ltd				
3.	Cefixime-	German	Cefixime	200	453.452	$C_{16}H_{21}N_5O_{10}S_2.H_2O$
	AZ	Remedies				
4.	Taxim-O	ALKEM	Anhydrous	200	453.444	$C_{16}H_{21}N_5O_{10}S_2$
		Health Science	Cefixime			
5.	Milixim	Glenmark	Anhydrous	200	453.444	$C_{16}H_{21}N_5O_{10}S_2$
			Cefixime			

When the experiment was performed, it was observed that the delay time of each THz pulse after passing through different samples are different. Such delay is the variation in the optical path, which also causes a change in the refractive index of the materials. The variation in the spectral intensity of medicine samples is shown in Fig. 5.9.

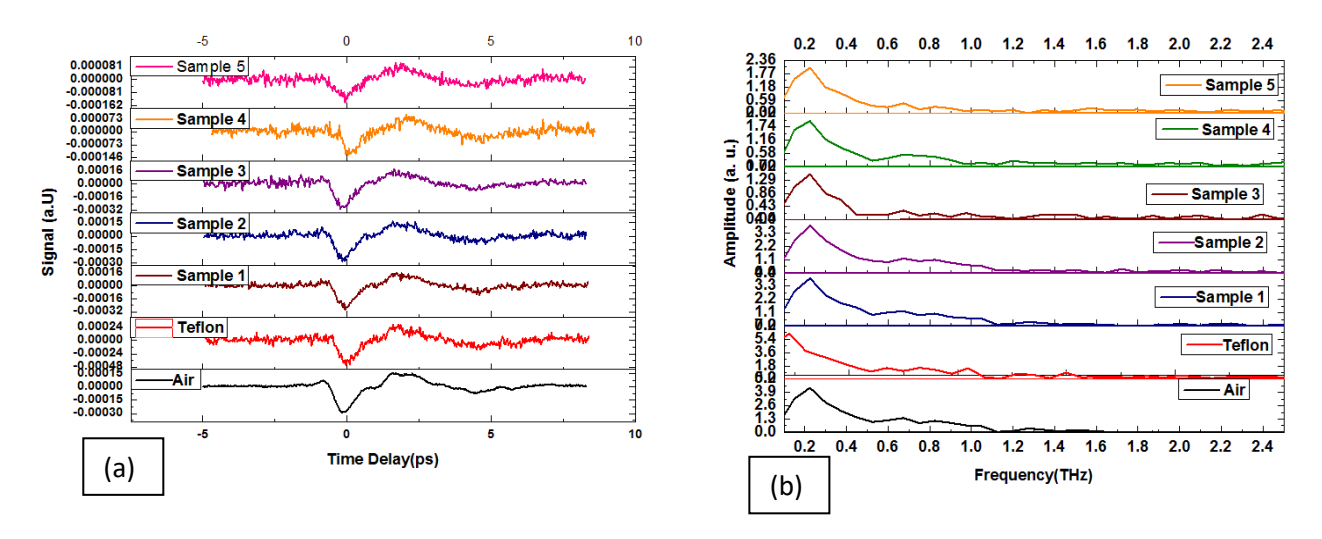


Figure 5. 9 (a, b): Terahertz spectrum of medicine samples, (a) Temporal profile of THz-pulse, and (b)frequency domain spectra

Figure 5.9 shows the temporal and frequency domain spectrum of the samples between 0.1-2.4 THz range. The amplitude of spectral lines lies between 10^{-4} to 10^{-7} range, which is used to

record the medicine samples' weak absorption peaks. The corresponding THz absorption peaks for sample 1 to sample 5 are 3.4, 3.4, 1.30, 1.75, 2.00 arbitrary units, respectively.

• Raman Spectroscopy:

As represented in Table 5.3, the same samples were subjected to 785nm Raman spectroscopy to study the different frequency bands present in the medicine samples. The Raman Spectra obtained are shown in Fig.5.10. Raman spectroscopy is widely used as a standard technique for the investigation of solid-state drugs. Raman spectra of the cefixime tablet are recorded in the 200–3000 cm⁻¹ range, as shown in Fig. 5.10. Experimental results show that all the samples (1-5) share a standard peak at 1612.97 cm⁻¹, which corresponds to the D' (Defect) band. This helps us conclude that there is some similarity between the samples, which is evident from the fact that all the samples considered are different versions or polymorphs of the same tablet; cefixime procured by various manufacturers in the market but an essential point to be considered is that apart from this peak, there is no other peak found common among the sample which should ideally have been the case since all the samples have the same composition. The intensities and vibrational modes of Raman spectra are related to the change in polarization of specific chemical bonds within molecules. The details of the peaks observed are represented in Table 5.4.

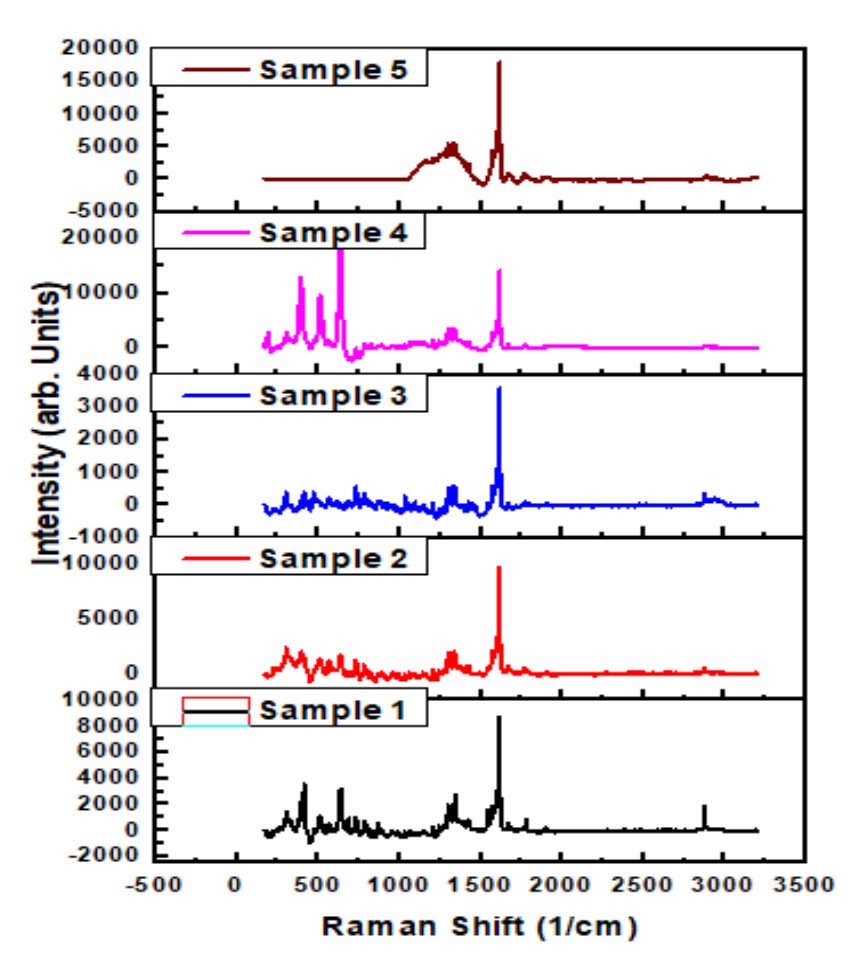


Figure 5. 10 Raman Spectroscopy of medicine samples (1-5)

Table 5. 4 shows the correspondence of various peaks obtained in the Raman Spectra to its corresponding bond assignment

S. No.	Common propertie s	S1		S2		S3		S4		S5	
		Raman Shift (cm ⁻¹)	Intensity (arb.uni.)	Raman Shift (cm ⁻¹)	Intensity (arb.uni.)	Raman Shift (cm ⁻¹)	Intensity (arb.uni.)	Raman Shift (cm ⁻¹)	Intensity (arb.uni.)	Raman Shift (cm ⁻¹)	Intensity (arb.uni.)
1.	Aliphatic Chain	302.764	373.578	304.946	1409.44	-	1	305.223	2270.27	88.508	2726.21
2.	Aliphatic Chain	4 302.764 4	173.164	413.442	3597.30 6	1	ı	413.4	1450.89	1	1
3.	D	302.764	506.642	1300.65 3	1934.9	1330.25 6	5400.71	1300.83	1858.74	1300.41 5	3502.19
4.	D	302.764	598.360	1336.19 3	8	1336.64	5589.85 7	1336.00 4	82.0002	1336.08 4	3549.17 2
5.	D	302.764	401.4031	1345.9073	2721.211	-	1	-	-	_	1
6.	D	302.764	16.0139	1	1	1403.37 3	2699.17 9	1	1	ı	1
7.	G	302.764	47.5579	1541.01	1530.93 6	-	1	-	-	1	ı
8.	G	302.764	560.931	1570.0937	1870.402	1570.8	4383.901	1569.29	2088.358	1569.93	2687.5
9.	D'	302.764	3570.124	1612.62	8602.194	1612.939	17870.18	1612.967	9654.499	1613.809	14135.15

• Comparison between THz Spectroscopy and Raman Spectroscopy:

Raman spectroscopy finds its application in various research fields, beginning from fundamental material science, pharmaceuticals and narcotics analysis, explosive detection to cancer pathology. This technique is fast, easy to use, less expensive, and compact. Spectral analysis using portable Raman systems are also commonly available now. Raman spectroscopy mostly provides chemical information about the samples, and its extension to structural analysis is limited due to its detection efficiency and cost of expense. In pharmaceuticals and narcotics, which involves the detailed analysis of various drugs, the molecular structure becomes vital as molecules exist in multiple forms, known as "polymorphs." Many pharmaceutical medicines have Carbon's presence, which can exhibit radically different properties based on the way it is arranged. For example, pencil lead, diamond crystal, graphene sheet, carbon-nanotube, etc. are various forms of carbon, but their properties are entirely different. In today's scenario, the commonly used techniques for structural studies are mainly XRD, FTIR, THz absorption spectroscopy, etc., which have many limitations individually. Some of the common limiting factors are their high cost and the requirement of detailed sample preparation techniques. They are limited by the physical form in some cases (solid, liquid, or gaseous samples) and are also affected by environmental conditions. On the other hand, Raman spectroscopy is non-destructive, non-invasive, and requires a minimal amount of any sample (solid, liquid, or gas). Important structural information like polymer structure, orientation, and phonon modes can also be determined. The only limitation in Raman spectroscopy is its spectral range from 200 cm⁻¹ to 4000 cm⁻¹.

Within this range, the region between 500 and 1500 cm⁻¹ is usually called the "fingerprint" of the molecules. This spectrum helps us identify different substances, but, in this case, molecules with very low vibrational frequencies are difficult to analyze using Raman spectroscopy. The most recent reports suggest that Raman spectroscopy can provide details up to 50cm⁻¹ range as well, but no information about the molecule can be obtained beyond that. This is where THz spectroscopy can play an important role. Therefore, the peaks which were missing in the Raman spectroscopy due to low phonon absorption and low vibrational frequencies could be detected in the THz domain. The range of THz generated for the medicine samples is 0.1-1.6 THz, as shown in Fig.5.9 (b), which corresponds to 3.3356 cm⁻¹-53.3702 cm⁻¹. When we consider the Raman spectroscopy shown in Fig. 5.10, we can see that such a low vibrational frequency (3.3356 -53.3702 cm⁻¹) is not available in the case of Raman Spectroscopy. However, it becomes very evident in the case of THz Spectroscopy for the same molecules. This is also shown in Table 5.5.

Table 5. 5 Comparsion between THz and Raman Spectroscopy

Parameter (Experimental)	THz Spectroscopy(THz)	Corresponding Raman Spectroscopy(cm ⁻¹)
Initial Frequency Obtained	0.1	3.3356

Final Frequency Obtained	1.6	53.3702
Time at these frequencies	10,000 fs	625.00 fs

The following schematic diagram, Fig. 5.11 explains the joint region between Raman Spectroscopy and time-domain THz spectroscopy.

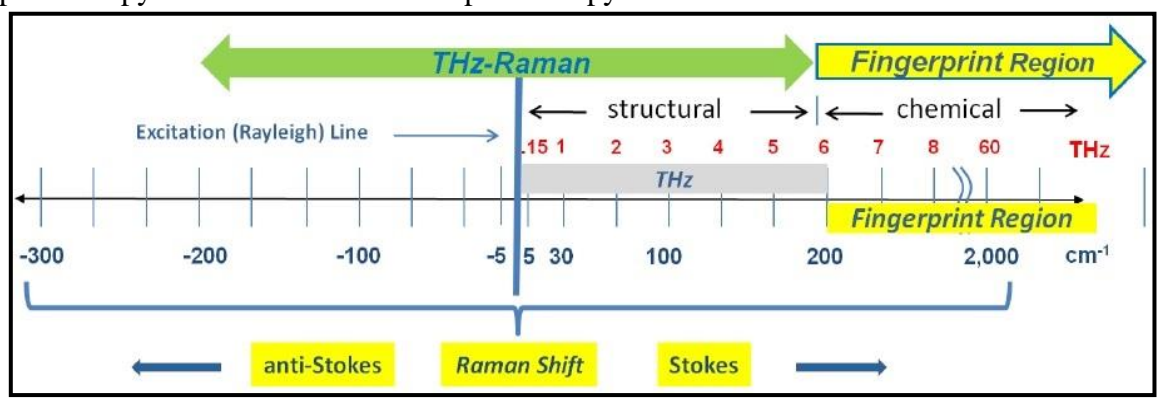


Figure 5. 11 Schematic diagrams explaining the joint region between Raman Spectroscopy and time-domain THz spectroscopy, excerpt taken from reference [27-29].

THz frequency is unavailable for traditional Raman Spectrometers due to edge/notch filters used to block out the Rayleigh backscatter from the excitation laser source. Raman spectroscopy is very similar to IR spectroscopy. By extension to THz-Time domain spectroscopy, both techniques provide vibrational bands at different frequencies. We can easily find the spectra of molecules at lower frequencies. Recent advancements in Ultra-Narrow Band Filters' area will provide an essential step towards extending the Raman system into ultra-frequency Terahertz Raman (THz-Raman). This will allow structural analysis within the standard Raman system. Another significant advantage of doing this would help us overcome the sensitiveness to water vapor for the traditional THz spectroscopy system. Further details are given in Appendix E.

The peaks which were missing in the Raman spectroscopy due to low phonon absorption could only be detected in THz domain. The absorption coefficients of the samples Sample 1 to Sample 5 follow the following order: At 0.5 THz: $S_5 > S_2 > S_3 > S_4 > S_1$; at 1 THz: $S_4 > S_5 > S_2 > S_1 > S_3$; at 1.5THz: $S_4 > S_2 > S_3 > S_5 > S_1$; at 2.0 THz: $S_5 > S_4 > S_1 > S_2 = S_3$ and at 2.5 THz: $S_2 > S_4 > S_5 > S_3 > S_1$. The refractive index constantly decreases up to a value of 1.5 THz in case of all samples and then it becomes constant. The refractive index of sample 4 is highest and has the value 1.75 followed by sample 5, 2, 3, and 1.

Absorbance Strength:

Once the spectral data of a sample were obtained, the absorbance (A(v)) could be calculated in dB as:

$$A(v) = -10 \log \frac{E(v)sample}{E(v)reference}$$

Where, $E(\nu)$ represents the strength of the THz peak. In order to calculate the specific absorbance strength, the effective mass, M_{eff} is required to be calculated. Thus,

$$M_{eff} = M_{Sample} * \frac{cross - section \ area \ of \ THz \ beam}{cross - section \ area \ of \ the \ sample \ pellet}$$

Hence, Specific absorbance $A_s(v)$ is given as,

Specific Absorbance
$$As(v) = \frac{A(v)}{Meff}$$

The specific absorbance is calculated at THz frequencies; 0.5 THz. The results are provided in Table 5.6.

Table 5. 6 The absorbance and specific absorbance at THz frequencies; 0.5 THz

Sample	Absorbance Strength, A(v)	Specific Absorbance, A _s (v)
S1	2.13	0.095
S2	2.13	0.095
S3	6.57	0.295
S4	5.07	0.228
S5	4.94	0.222

The following graphs, fig. 5.12 represent the above data at three frequencies: 0.25, 0.5, and 0.8 THz.

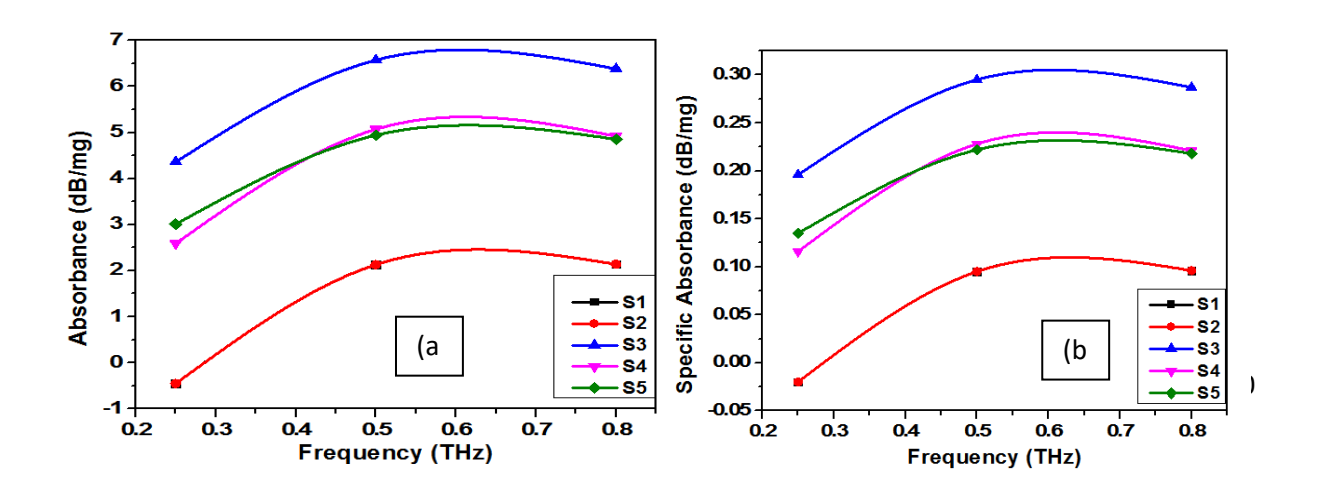


Figure 5. 12 (a)shows the absorbance strength, and (b) represents the specific absorbance of all samples(S1-S5) at different frequencies.

Thus, in this section, we have analyzed the recorded time-domain THz Spectra, Raman Spectra, refractive indices, and the samples' absorption coefficients. The most important finding is that in-spite of having the same chemical structure of all the various versions of Cefixime tablet used, their refractive index, absorption coefficient, and the absorbance strength are constant physical parameters change for each of the medicine samples considered.

5.6 Conclusion:

We have demonstrated the effect of femtosecond laser pulse duration, temperature, and incident laser power on the THz generation process from nonlinear CdTe crystal. In the case of femtosecond laser pulses, the drop in the transmission is utilized in nonlinear absorption. The contribution to phonon-phonon interaction and thermal lattice vibration is also analyzed. Finally, as observed from the modified spectrophotometer of CdTe, the transmission becomes close to zero at 408K, which proved the opacity of CdTe at higher temperatures. We have also successfully recorded the time-domain THz and Raman Spectra of Cefixime drug obtain from different manufacturers. In addition, we have ascertained their refractive indices and absorption coefficients and carried out quantitative analysis using absorbance strength. The Raman spectra help to identify the aliphatic chain, D, and G bands. In contrast, THz spectroscopy identifies the crystalline nature and quantifies the sulphha pyridine and thiazole groups, which are the drug molecules' principal ingredients. Absorbance and absorption strength were also estimated, which helps in the quality assessment of the drug molecules.

References:

- 1. Y-S Lee, Principles of Terahertz, Science and Technology, Springer, (2009).
- 2. X-C Zhang and J Xu, Introduction to THz Wave Photonics, Springer Science + Business Media, LLC, (2010).
- 3. D. F. Plusquellic, K. Siegrist, E. J. Heilweil and O. Esenturk, Applications of Terahertz spectroscopy in biosystems, Chem Phys Chem, 8, 2412-2431 (2007).
- 4. S. Dexheimer, Terahertz Spectroscopy: Principles and Applications in Terahertz Spectroscopy: Principles and Applications, Taylor & Francis, 360 (2007).
- 5. Z Wang, Generation of terahertz radiation via nonlinear optical methods, IEEE. Trans. Geosci. Remote Sens., 1, 1–5, (2001).
- 6. K Dobroiu, C Otani, and K Kawase, Terahertz wave sources and imaging applications, Meas. Sci. Tenchnol., 17(11), 161–174, (2006).
- 7. B Pradarutti, G Mattäus, S Riehemann, G Notni, S Nolte, and A Tünnermann, Advanced analysis concepts for terahertz time domain imaging, Optics Communication., 279, 248–254, (2007).
- 8. D L Woolard, W R Leorop, and M S Shur, Terahertz sensing technology, World Scientific Publishing Co. Pte. Ltd., 1, (2003).
- 9. F D Bruner, A Schneider, and P Günter, Terahertz time domain spectrometer for simultaneous transmission and reflection measurements at normal incidence, Optical Society of America, 17(23), 20684-20693, (2009).
- 10. M T Reiten. Spatially resolved terahertz propagation. PhD thesis, Oklahoma State University, 80 Stellenbosch University http://scholar.sun.ac.za Bibliography, (2006).
- 11. S Wietzke, C Jansen, T Jung, M Reuter, B Baudrit, M Bastian, S Chantterjee, and M Koch, Terahertz time-domain spectroscopy and a tool to monitor the glass transition in polymers, Optical Society of America., 17(21), 19006–19014, (2009).
- 12. Applied Research and Photonics, Terahertz spectroscopy brings new dawn of biological research, available from http://arphotonics.net, (2008).
- 13. V Mottamchetty and A K Chaudhary, Improvised design of THz spectrophotometer using LT-GaAs photoconductive antennas, pyroelectric detector and band-pass filters, Indian J Phys, 90, 73-78 (2015)

- 14. Y.P. Varshni, Temperature Dependence of the energy gap in Semiconductors, Physica, 34(1), 149-154 (1967)
- 15. A. Kumari, M. Venkatesh, and A. K. Chaudhary, in 13th International Conference on Fiber Optics and Photonics, OSA Technical Digest (online) (Optical Society of America, 2016), paper W3A.6.
- 16. G. G. Rusu, On the Electrical and Optical Properties Of Nanocrystalline CdTe Thin Films, Journal of Optoelectronics and Advanced Materials, 3(4), 861 866, (2001).
- 17. Marek Buga' r n , Eduard Belas, Jan Procha' zka, Pavel Hlı'dek, Roman Grill, Jan Franc, Pavel Hoschl, IR transmittance of CdTe after high-temperature annealing Nuclear Instruments and Methods in Physice Research, A633, S83-S85, (2011)
- 18. M. Quintero, J. Conzalez and J. C. Wolley, Optical energy-gap variation and deformation potentials in CuInTe₂. Journal of Applied Physics 70, 1451 (1991).
- 19. G. Fonthal, Temperature dependence of the band gap energy of crystalline CdTe. Journal of Physics and Chemistry of Solids. 61. 579-583, (2002).
- 20. E. Belas, E.Uxa Grill, R.Hlídek, P.Šedivý, L.Bugár, High temperature optical absorption edge of CdTe single crystal: Journal of Applied Physics 116, 103521, (2014)
- 21. R. F. Brebrick and R. Fang, CdTe I: Solidus Curve And Composition-Temperature-Tellurium Partial Pressure Data For Te-Rich CdTe(s) From Optical Density Measurements, J. Phys. Chem. Solids 57, 451 (1996).
- 22. Laser-induced damage measurements in CdTe and other II-VI materials M. J. Soileau, William E. Williams, Eric W. Van Stryland, and M.A. Woodall APPL~ED OPTIC_S, Vol. 21, page 4059, November 15 (1982)
- 23. T. Bardon, R. K. May, P. F. Taday, and M. Strlič, Influence of Particle Size on Optical Constants from Pellets Measured with Terahertz Pulsed Spectroscopy, IEEE Trans. Terahertz Sci. Technol. 6, 408–413 (2016)
- 24. J. Chen, Y. Chen, H. Zhao, G. J. Bastiaans, and X.-C. Zhang, Absorption coefficients of selected explosives and related compounds in the range of 0.1-2.8 THz., Opt. Express 15, 12060–12067 (2007)

- 25. Mrudul R Keskar and Ravin M. Jugade, Spectrophotometric Determination of Cefixime Trihydrate in Pharmaceutical Formulations Based on Ion-Pair Reaction with Bromophenol Blue, Anal.Chem. Insights, 10,11-16 (2015)
- 26. JanakideviSirisolla and K.V. Ramanamurthy, Formulation and Evaluation of Cefixime Trihydrate Matrix Tablets Using HPMC, Sodium CMC, Ethyl Cellulose, Indian J. Pharm. Sci. 77(3), 321-327 (2015)
- 27. K. S. Rao, A. K. Chaudhary, M. Venkatesh, K. Thirupugalmani, and S. Brahadeeswaran, DAST crystal based terahertz generation and recording of time resolved photoacoustic spectra of N2O gas at 0.5 and 1.5 THz bands, Curr. Appl. Phys. 16, 777–783 (2016).
- 28. M. Venkatesh, K. Thirupugalmani, K. S. Rao, S. Brahadeeswaran, and A. K. Chaudhary, Generation of efficient THz radiation by optical rectification in DAST crystal using tunable femtosecond laser pulses, Indian J. Phys. 91, 319–326 (2017).
- 29. P. Jepsen and B. Fischer, Dynamic range in terahertz time-domain transmission and reflection spectroscopy, Opt. Lett. 30, 29 (2005).
- 30. F. Fan, W. Li, W. H. Gu, X. H. Wang, and S. J. Chang, Cross-shaped metal-semiconductor-metal plasmonic crystal for terahertz modulator, Photonics Nanostructures Fundam. Appl., 11(1), 48–54 (2013).
- 31. M. He, A. K. Azad, S. Ye, and W. Zhang, Far-infrared signature of animal tissues characterized by terahertz time-domain spectroscopy, Opt. Commun., 259(1), 389–392, (2006).
- 32. Y. Jiang, F. Zhou, X. Wen, L. Yang, G. Zhao, H. Wang, H. Wang, Y. Zhai, J. Wu, K. Liu, and J. Chen, Terahertz absorption spectroscopy of benzamide, acrylamide, caprolactam, salicylamide, and sulfanilamide in the solid state, J. Spectrosc., 2014, 1–9, (2014).
- 33. D. J. Olego, J. P. Faurie, S. Sivananthan, and P. M. Raccah, Optoelectronic properties of $Cd_{1-x}Zn_xTe$ films grown by molecular beam epitaxy on GaAs substrates, Appl. Phys. Lett. 47, 1172 (1985).
- 34. European Scientific Journal January 2014 edition vol.10, No.3 ISSN: 1857 7881 (Print) e ISSN 1857- 7431
- 35. IEEE Journal Of Selected Topics In Quantum Electronics, 14, 2, (2008)
- 36. K. Chattopadhyay, X. Maa, J.-O. Ndapa, A. Burger, T. E. Schlesingerb, M. Greavesb, : H. L. Glass, J. P. Flint, and R. B. Jamesd: Thermal Treatments of CdTe and CdZnTe Detectors, 487,229, (1998)

- 37. S.Lalitha1, S.Zh.Karazhanov, P.Ravindran, S.Senthilarasu1, R.Sathyamoorthy and J.Janabergenov, Electronic structure, structural and optical properties of thermally evaporated CdTe thin films, arxiv.org, Material Science, Phys. B, (2006)
- 38. E. Belas, Š. Uxa, R. Grill, P. Hlídek, L. Šedivý, and M. Bugár High temperature optical absorption edge of CdTe single crystal, J. Appl. Phys. 116, 103521 (2014).
- 39. Mandal, Krishna C. Kang, Sung Hoon Choi, Michael Chen, Jian Zhang, Xi Cheng Schleicher, James M., IEEE Journal of Selected Topics in Quantum Electronics, 14, 2, (2008).
- 40. R. F. Brebrick and R. Fang, CdTe II: Defect chemistry, J. Phys. Chem. Solids 57(4), 451-460, (1996).
- 41. G. Fonthal, L. T. Mejia, J. I. M. Hurtado, H. A. Calderon, and J. G. M. Alvarez, High Temperature Optical Edge of CdTe, J. Phys. Chem. Solids 61, 579 (2000).
- 42. Li, Bing Feng, Lianghuan Zheng, Jiagui Cai, Wei Cai, Yaping Zhang, Jingquan, Conference Record of the IEEE Photovoltaic Specialists Conference, (2006).
- 43. S. Lalitha, S. Karazhanov, Electronic Structure, Structural and Optical Properties of Thermally Evaporated CdTe Thin Films, Physica B Condensed Matter 387(1-2), (2006).
- 44. M. Venkatesh, K.S. Rao, T.S. Abhilash, S.P. Tewari, A.K. Chaudhary, Optical characterization of GaAs photoconductive antennas for efficient generation and detection of Terahertz radiation, Optical Materials 36, 596–601, (2014).
- 45. B. Ferguson and X.-C. Zhang, Materials for terahertz science and technology., Nat. Mater., 1(1), 26–33, (2002).
- 46. Y. Jiang, F. Zhou, X. Wen, L. Yang, G. Zhao, H. Wang, H. Wang, Y. Zhai, J. Wu, K. Liu, and J. Chen, Terahertz absorption spectroscopy of benzamide, acrylamide, caprolactam, salicylamide, and sulfanilamide in the solid state, J. Spectrosc., 2014, 1–9, (2014).
- 47. Y. C. Shen, P. C. Upadhya, E. H. Linfield, H. E. Beere, and A. G. Davies, Ultrabroadband terahertz radiation from low-temperature-grown GaAs photoconductive emitters, Appl. Phys. Lett., 83(15), 3117–3119, (2003).
- 48. A. Bonvalet, M. Joffre, J. L. Martin, and A. Migus, Generation of ultrabroadband femtosecond pulses in the mid-infrared by optical rectification of 15 fs light pulses at 100 MHz repetition rate, Appl. Phys. Lett., 67(79), 2907, (1995).

- 49. R. N. Brogdenand D. M. Campoli-Richards, Cefixime: A Review of its Antibacterial Activity, Pharmacokinetic Properties and Therapeutic Potential, Drugs 38 (4): 524-550. (1989).
- 50. Review in terahertz spectral analysis Josette El Haddad, Bruno Bousquet, Lionel Canioni, Patrick Mounaix, 749-788, (2013)
- 51. M. Tonouchi, Cutting-edge terahertz technology, Nature Photonics 1, 97–105, (2007).
- 52. Anthony J. Fitzgerald, Bryan E. Cole, Nondestructive Analysis of Tablet Coating Thicknesses Using Terahertz Pulsed Imaging, J Pharm Sci 94:177–183, (2005)
- 53. M. Venkatesh, S. Ramakanth, A.K. Chaudhary, and K.C. James Raju, Study of terahertz emission from nickel (Ni) films of different thicknesses using ultrafast laser pulses, Optical Materials Express 6(7), 2342, (2005).
- 54. N.P. Barnes and M.S. Piltch, Temperature dependent sellmeier Coefficients and coherence length for cadmium telluride, J. Opt. Soc. Am., 67(5),628-629 (1977)
- 55. A. Khachatrian, S. Qadri, and J. S. Melinger, High resolution THz spectroscopy of ammonium nitrate and potassium nitrate crystalline films, 2011 Int. Conf. Infrared, Millimeter, Terahertz Waves 1–2 (2011).
- 56. T. Trzcinski, N. Palka, and M. Szustakowski, THz spectroscopy of explosive-related simulants and oxidizers, Bull. Polish Acad. Sci. Tech. Sci. 59, 445–447 (2012).
- 57. K. Tanaka, H. Hirori, and M. Nagai, THz nonlinear spectroscopy of solids, IEEE Trans. Terahertz Sci. Technol. 1, 301–312 (2011).
- 58. M. a Jarzembski, M. L. Norman, K. a Fuller, V. Srivastava, and D. R. Cutten, Complex refractive index of ammonium nitrate in the 2-20-microm spectral range., Appl. Opt. 42, 922–30 (2003).
- 59. Ganesh Damarla, M. Venkatesh, and A. K. Chaudhary, Temperature-dependent terahertz spectroscopy and refractive index measurements of aqua-soluble and plastic explosives, 57, 29,8743-8750 (2018)
- 60. 5. P. R. Smith, D. H. Auston, and M. C. Nuss, SubpicosecondPhotoconducting Dipole Antennas, IEEE J. Quantum Electron., 24(2), 255–260, (1988).
- 61. 6. C. Fattinger and D. Grischkowsky, Terahertz beams, Appl. Phys. Lett., 54(6), 490–492, (1989).
- 62. 7. M. D. King, W. D. Buchanan, and T. M. Korter, Understanding the Terahertz Spectra of Crystalline Pharmaceuticals: Terahertz Spectroscopy and SolidState Density

- Functional Theory Study of (S)-(+)-Ibuprofen and (RS)- Ibuprofen, J. Pharm. Sci., 100(3), 1116–1129, (2011).
- 63. 8. O. Esenturk, J. S. Melinger, P. A. Lane, and E. J. Heilweil, Uiltrafast Photoinduced Carrier Dynamics of Organic Semiconductors Measured by Time-resolved Terahertz Spectroscopy, Org. Thin Film. Photonic Appl., 1039, 241–254, (2010).
- 64. 10. O. Esenturk, J. S. Melinger, and E. J. Heilweil, Photoconductivity of organic semiconductor polymers studied by time-resolved THz-TDS, Jt. 32Nd Int. Conf. Infrared Millim. Waves 15Th Int. Conf. Terahertz Electron, 178 (2), 655–656, (2007).
- 65. 11. C. J. Docherty and M. B. Johnston, Terahertz properties of graphene, J. Infrared, Millimeter, Terahertz Waves, 33(8), 797–815, (2012).
- 66. 12. M. C. Kemp, P. F. Taday, B. E. Cole, J. Cluff, A. J. Fitzgerald, and W. R. Tribe, Security applications of terahertz technology, Proc. SPIE, 5070, 44–52, (2003).

Chapter 6 Conclusion and Future Scope

Spectroscopic techniques have become a significant part of scientific research related to studying different organic, inorganic, and explosive substances and their characterization based on their properties. This thesis successfully explores the wide range of electromagnetic spectra between UV-Vis-NIR and far IR regions. It uses various spectroscopic techniques to characterize the properties of organic, inorganic, and explosive samples in different ranges of the EM spectra. This thesis has attempted to provide a link between other spectroscopic techniques such as Photoacoustic, Raman, and Terahertz (THz) spectroscopy. Further, we have tried to extend the range of information obtained from the molecules using Terahertz spectroscopy to Raman spectroscopy, especially for bulky molecules, by combining these techniques using the THz-Raman spectroscopic technique. Also, the results obtained by Photoacoustic spectroscopy have been further substantiated by another standard and well-established spectroscopic tool, which is the Raman Spectroscopy.

In this thesis, we have selected different laser-based spectroscopic techniques such as the use of visible (532 nm) nanosecond laser for photoacoustic spectroscopy, use of CW laser (532nm and 785nm) for Raman spectroscopy, use of femtosecond laser for generation and detection of Terahertz using non-linear CdTe crystal and use of FTIR and Raman spectroscopy to establish the new results obtained. We have also concentrated on the temperature-dependent properties of CdTe along with its non-linear absorption and have explained how the properties change when subjected to femtosecond laser pulses using a modified temperature-based spectrometer. The region between UV-Vis-NIR covers different aspects of molecular spectroscopy such as electronic transition-based vibronic and vibrational modes, vibrational-rotation and weak vibrational-rotation bands along with Raman scattering. An attempt has been made to use these techniques without any chemical treatment and in a non-destructive way to be reused again.

One of the advantages of photoacoustic spectroscopy is that it can be performed on all phases of matter. In one section of this thesis, the emphasis has been given on pulsed photoacoustic technique using 532 nm wavelength (visible) of pulsed laser for the study of conducting polymers like PEDOT and its role as a detector for solid explosives. It is also extended to study the physical properties of different types of natural rubber added with reenforcing agents like

organic and inorganic fillers. Fig. 6.1 briefly illustrates the link between other techniques used in the thesis.

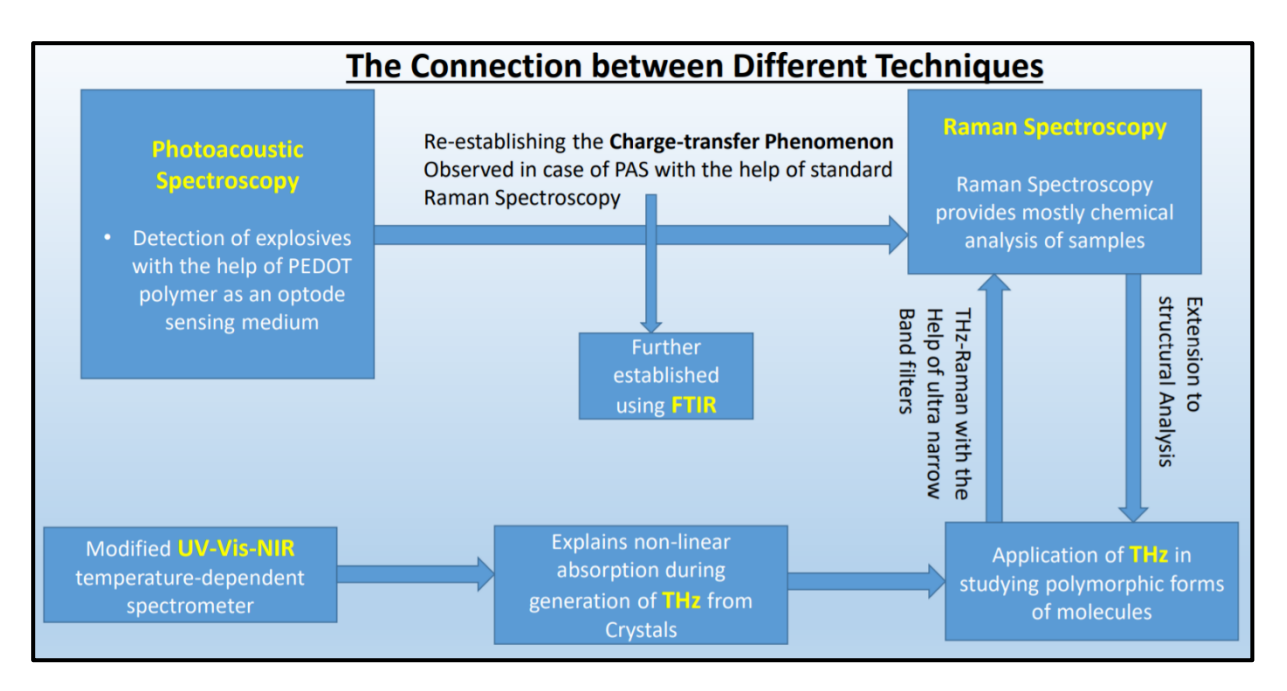


Figure 6. 1 It briefly illustrates the link between different techniques used in the thesis.

Scientists have been researching various methods for detecting explosives and high energy materials for several decades as they are a grave danger to life, health, and environment. Detection of explosives like RDX, HMX, TNT, CL20, and TEX has always been a challenge and possesses no significant absorption in the visible region. There is a high demand for portable, reliable, and low-cost sensors for war against explosives in terror activities. In the past few years, various analytical spectroscopic techniques such as metal detectors, ion mobility spectroscopy (IMS), and thermal neutron analysis are being used to detect and quantify explosive molecules. Unfortunately, metal detectors, the most commonly used device, are prone to false results.

Using non-radiative, non-destructive, and visible range Photoacoustic Spectroscopy (PAS), we have been able to successfully establish the conjugated PEDOT polymer as a cost-effective, reliable, and highly sensitive optode sensor for low level detection of solid explosives like RDX, HMX, TNT, CL-20, and TEX. This polymer can also be bottled in liquid form as spray for easy distribution. We have also proposed an alternative method for the detection of these explosives in the matrix of the polymer PEDOT using Raman Spectroscopy. Using the Stokes/anti-Stokes Raman lines intensity ratio, we have clearly indicated the changes that occur when explosives are mixed with PEDOT. The FTIR spectroscopy further substantiates these results. Additionally, we have studied the effects of fillers used as reinforcements to increase the durability and strength of polymers, especially the rubber polymer.

We have also successfully recorded the transmission properties of a non-linear crystal, CdTe using a self-modified temperature-dependent UV-Vis-NIR spectrometer to explain the changes in properties of the crystal when it is subjected to femtosecond laser pulses for a long duration

of time. This same crystal has been used for the generation of THz frequency. This THz frequency has been utilized to probe and analyze different polymorphs of the antibiotic Cefixime drug on the basis of their physical properties along with their quality assessment, which is very crucial for the food and drug industries.

Future Scope:

Photoacoustic Spectroscopy

In Spectroscopy:

- > Storing of PEDOT conjugated polymer in liquid form in spray bottles keeping in mind its easy use on the field, cost, and availability. It has already been tested by our group that liquid PEDOT polymer has a characteristic fingerprint spectrum in Photoacoustic Spectroscopy.
- ➤ Use of picosecond and tunable Quantum Cascade Laser (QCL) in the visible to the mid-IR range to further broaden the range of detection of explosive molecules.
- ➤ Design and use of liquid photoacoustic cell for studying liquid solvents and detection of explosives dissolved in water and other solvents.
- ➤ Photoacoustic imaging of various solid samples along with explosives and High Energy Materials.

In Medicine and Biophysics:

Based on Solid Cell Photoacoustic Spectroscopy

➤ Using PAS in the food/drug industry for optical characterization of fruits, vegetables, condiments, grains, legumes, flours, etc. to evaluate adulterated, irradiated, and contaminated food and their quality assessment.

Based on Solid Cell Photoacoustic Spectroscopy

- > Study of optical properties of Cancerous tissues and cells
- ➤ Blood cells can be imaged at a single wavelength in the visible range because of their high optical absorption contrast compared to surrounding tissues.
- > To detect oxygen saturation in blood vessels

Terahertz Spectroscopy and Raman Spectroscopy:

In medicine, various polymorphs of different drugs and drugs are often confused due to similar-sounding names. THz spectroscopy can play a significant role in differentiating such polymorphs, thereby proving to be an essential part of the food and drug industry. Further, bulk molecules can be analyzed in more critical details, and the information about the vibration of

molecules even lower than 50 cm⁻¹ can be determined using THz-Raman Spectroscopy. Various other future scopes exist, some of which are listed below:

- ➤ Generation of efficient Terahertz radiations using nonlinear crystals other than CdTe, such as ZnTe, ZnGeP₂, etc. coupled with bandpass filters and gratings to record the pulsed PA spectra of HEMs. This will help us combine the two well established spectroscopic techniques; Photoacoustic and Terahertz.
- Most of the HEMs possess several rotational lines. Therefore, THz spectroscopy helps us to record the fingerprint spectra of these compounds.
- ➤ The time-domain THz spectroscopy, as well as PA Spectroscopy, can help us to build a library database for the detection of HEMs.
- ➤ Development of optical parametric oscillator (OPO) using the DFG technique for efficient generation of tunable THz radiation.

Publications

- 1. **Archana Kumari**, A. K. Chaudhary, and M. Venkatesh, "Linear and nonlinear temperature-dependent transmission/absorption characteristics of cadmium telluride crystal for terahertz generation," Appl. Opt. 59, 3417-3421, (2020)
- 2. **Archana Kumari**, A. K. Chaudhary, Rajasekhar K. "Study of charge transfer mechanism of PEDOT polymer for detection of solid TEX and CL-20 explosives using pulsed photoacoustic technique" Spectrochim Acta A Mol Biomol Spectrosc. 241, 118597 (2020)
- 3. **Archana Kumari**, M. Venkatesh, and A. K. Chaudhary, "Terahertz generation from Cadmium Telluride crystal using tunable oscillator laser pulses," in *13th International Conference on Fiber Optics and Photonics*, OSA Technical Digest (online) (Optical Society of America, 2016), paper W3A.6. (2016)
- 4. **Archana Kumari**. A. K. Chaudhary, "Study of metal and metal oxides in the matrix of graphite and graphene using photoacoustic technique" AIP Conference Proceedings, 2265, 030691 (2020)
- 5. Ramachandran K., **Archana Kumari**, Jitendra Acharya, Anil Kumar Chaudhary, "Evaluation of PEDOT as a photoacoustic sensor for the detection of high energy materials using time-resolved pulsed photoacoustic and Raman spectroscopy"

Status: In Review in JOLT(Journal of Optics and Laser Technology)

6. **Archana Kumari**, Anil Kumar Chaudhary, "Detection of RDX, TNT, and HMX Using PEDOT Optode in Pulsed Photoacoustic Spectroscopy – A Non-Radiative Decay Technique"

Status: Under Revision with Applied Physics B

7. **Archana Kumari**, Ramachandran K., Jitendra Acharya, Anil Kumar Chaudhary, "Methodology for the use of PEDOT polymer as an active host medium for detection of High Energy Materials (HEMs) using Raman Spectroscopy"

Status: Submitted to MethodX

8. **Archana Kumari,** Hanna J Maria, A.K. Chaudhary, and S. Thomas, "Time Domain Pulsed Photoacoustic Technique to Study the Effect of Organic and Inorganic Fillers on Thermal and Optical Properties of Natural Rubber/Chlorobutyl Rubber Blend Nanocomposites"

Status: Under Revision in PRAMANA

9. Archana Kumari, D. Ganesh and A.K. Chaudhary, Use of Time domain Terahertz Spectroscopy for the characterization of Antibiotic Cefixime drug obtained from different origin along with assessment of their quality **Status**: **Communicated to International Journal of Pharmaceutics**

List of Conferences and workshops:

- 1. Participated in 10th International Conference on High Energy Materials Conference & Exhibit,11-13th February 2016, Hyderabad
- 2. Presented a poster, "Terahertz generation from Cadmium Telluride Crystal using tunable oscillator laser pulses" 13th International Conference on Fiber Optics and Photonics, Photonics 2016, IIT Kanpur, December 04-08, 2016. (OSA proceedings:ISBN: 978-1-943580-22-4).
- 3. Attended SERB School on Optical Metrology 01-21st June 2016, held at Department of Physics, Tezpur University, Tezpur, Assam
- 4. Participated in a "workshop on Mendeley" held at the University of Hyderabad on 9th March 2017, organized in collaboration with Elsevier Publisher.
- 5. Presented a poster in DAE-BRNS Theme meeting on Ultrafast Science 2017 (UFS-2017) held on November 2-4, 2017 organized by ACRHEM, University of Hyderabad & Indian Society for Radiation and Photochemical Science (ISRAPS)
- 6. Paper titled "Study of PEDOT Polymer as a Sensor for RDX and CL-20 in Photoacoustic Technique" ID: 3059 selected for Poster Presentation at Materials & Technologies for Energy Conversion and Storage (M-TECS 2018) held September 26-29, 2018 at Bhabha Atomic Research Centre, Mumbai
- 7. Selected for oral presentation for "Study of Charge transfer mechanism of PEDOT polymer for detection of solid explosives using pulsed Photoacoustic technique," 20th International Conference on Photoacoustic and Photothermal Phenomena, Session C4: Spectroscopy III, (159-160), 2019, held in Moscow, Russia, 2019
- 8. Presented a poster (ID: m0019) in 64th DAE Solid State Physics Symposium held at IIT Jodhpur, Rajasthan during 18-22nd December 2019

Raman, Time-Domain Photoacoustic and Terahertz Spectroscopy of some Inorganic, Organic and High Energy Materials

ORIGINALITY REPORT

12%

5%

11%

2%

SIMILARITY INDEX

INTERNET SOURCES

PUBLICATIONS

STUDENT PAPERS

PRIMARY SOURCES

Archana Kumari, A.K. Chaudhary, K.
Rajasekhar. "Study of charge transfer
mechanism of PEDOT polymer for detection of
solid TEX and CL-20 explosives using pulsed
photoacoustic technique", Spectrochimica Acta
Part A: Molecular and Biomolecular
Spectroscopy, 2020

2%

Publication

Archana Kumari, Mottamchetty Venkatesh, Anil K. Chaudhary. "Terahertz generation from Cadmium Telluride crystal using tunable oscillator laser pulses", 13th International Conference on Fiber Optics and Photonics, 2016

2%

Publication

3

www.osapublishing.org

Internet Source

1%

4

Archana Kumari, A. K. Chaudhary, M. Venkatesh. "Linear and nonlinear temperature-

1%

Dr. Anil Kr. Chaudhary
Professor (Physics)
Advanced Centre of Research in
High Energy Materials (ACRHEM).
High Energy Materials (ACRHEM).

dependent transmission/absorption characteristics of cadmium telluride crystal for terahertz generation", Applied Optics, 2020
Publication

5	shodhganga.inflibnet.ac.in Internet Source	<1%
6	Submitted to University of Hyderabad, Hyderabad Student Paper	<1%
7	Ganesh Damarla, M. Venkatesh, A. K. Chaudhary. "Temperature-dependent terahertz spectroscopy and refractive index measurements of aqua-soluble and plastic explosives", Applied Optics, 2018 Publication	<1%
8	G. Fonthal, L. Tirado-Mejía, J.I. Marín-Hurtado, H. Ariza-Calderón, J.G. Mendoza-Alvarez. "Temperature dependence of the band gap energy of crystalline CdTe", Journal of Physics and Chemistry of Solids, 2000 Publication	<1%
9	Samuel S. R. Dasary, Anant Kumar Singh, Dulal Senapati, Hongtao Yu, Paresh Chandra Ray. "Gold Nanoparticle Based Label-Free SERS Probe for Ultrasensitive and Selective Detection of Trinitrotoluene", Journal of the American Chemical Society, 2009	<1%

Anil Kr. Chaudhary
Professor (Physics)
Professor (Physics)
Advanced Centre of Research in
High Energy Materials (ACRHEM).
High Energy Materials (NOIA)

This is to certify that the thesis entitled "Raman, Time-Domain Photoacoustic and Terahertz Spectroscopy of some Inorganic, Organic and High Energy Materials" has been screened by the Turnitin software at the library of the University of Hyderabad. The software shows 12% similarity index, out of which 5% came from the candidate's own published research articles related to this thesis. The major part of the remaining (4%) comes from other articles published by my research group. Hence, the total similarity of the thesis is less than 10%.

Therefore, the thesis is free from plagiarism.

Prof. Anil Kumar Chaudhary

Dr. Anil Kr. Chaudhary
Professor (Physics)
Advanced Centre of Research in
High Energy Materials (ACRHEM),
UNIVERSITY OF HYDERABAD
HYDERABAD-500 046, T.S. INDIA.

Appendix A

• Heat Flow equation within the Photoacoustic Cell:

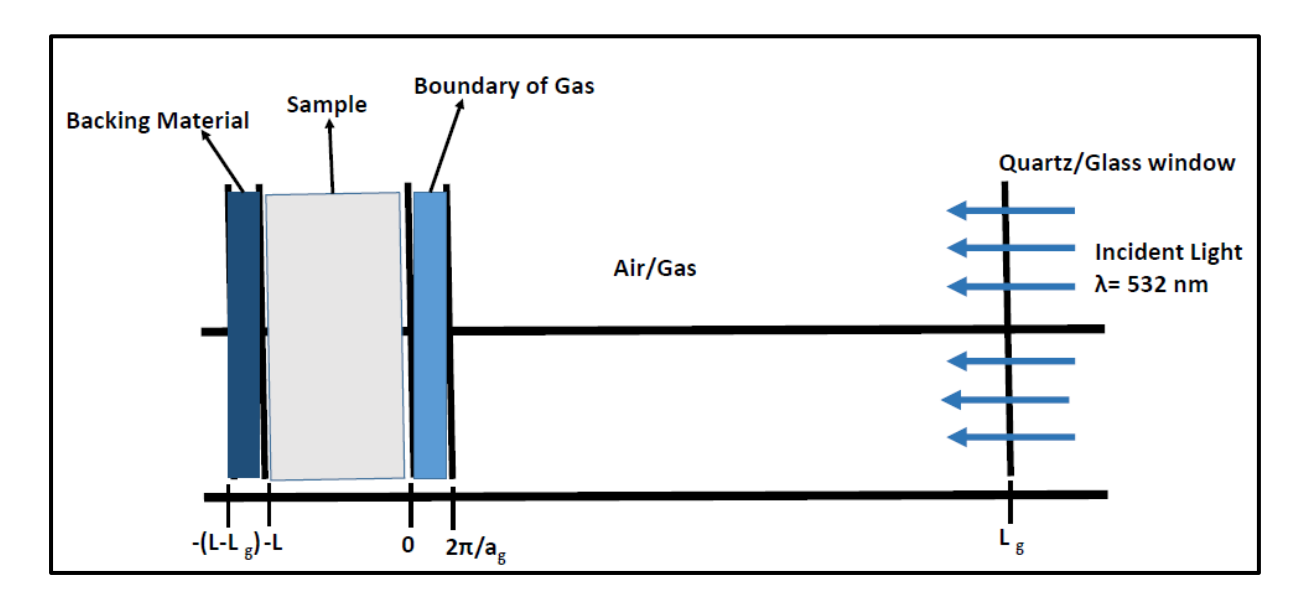


Fig:1 Schematic diagram of a one-dimensional solid-phase photoacoustic cell

• Assumptions made for the heat flow equation:

- 1. The photoacoustic cell is filled with non-adsorbing gases, for example, air.
- 2. The gas within the photoacoustic (P.A.) cell must have weak adsorption/absorption properties.
- 3. The body of the cell is made up of a substance such as solid aluminium/copper/gold, etc., which has a large thermal mass as it requires a large amount of energy to raise its temperature and cause any significant change in the acoustic signal due to body of the P.A. cell.
- 4. The primary source of the acoustic signal in the P.A. cell is local heating of the sample, leading to heat flow from the material to the surrounding solid when the sample is heated by the incident light.
- 5. The magnitude of the P.A. signal is proportional to the heat flowing from the solid sample and depends on the amount of incident light absorbed by the specimen.
- 6. The length 'L' of the cell is considered small compared to the wavelength used for the production of acoustic signals.

The incident light absorbed by the sample was converted into heat by nonradiative deexcitation processes within the solid cell. A one-dimensional schematic diagram of the heat flow in the section resulting from the absorbed light energy is given in fig. 7. A monochromatic light source with wavelength, λ (532 nm in our case) at a modulated frequency, ω is made incident on the solid sample with intensity, I, which is given as,

$$I = \frac{1}{2}I_0(1 + \cos\omega t) \tag{1}$$

 I_0 represents incident monochromatic light flux (W / cm²), and β denotes the solid sample's optical absorption coefficient (in cm⁻¹) for the wavelength, λ . The heat density (H_d) produced at any point 'x' within the cell due to light absorbed at this point in the solid is given by,

$$H_d = \frac{1}{2}\beta I_0 \exp(\beta x) \left(1 + \cos\omega t\right) \tag{2}$$

Here, 'x' takes negative values since the solid cell extends from x = 0 to x = -L with the light intensity at x = 0. As shown in fig.7, the gas column extends from x = 0 to x = Lg and the backing from x = -L to x = -(L + Lg).

The heat is generated within the sample and is given by Eqn. (2). It slowly warms up the sample and the backing material by adding ζ (x, t) above the ambient temperature, T_0 and hence, the rise in temperature is expressed by

$$\zeta(x,t) = T(x,t) - T_0 \tag{3}$$

The amount of heat transferred by the sample depends on the thermal conductivity of the medium. Therefore, the thermal diffusion equation for the sample is given by

$$\frac{\partial^2 \zeta}{\partial x^2} = \frac{1}{\alpha_s} \frac{\partial \zeta_s}{\partial t} - A e^{\beta x} (1 + e^{i\omega t}) \tag{4}$$

Where α_s is the thermal diffusivity, and A is a constant, which have been defined as

$$\alpha_s = \frac{k_s}{\rho_s C_s} \tag{5}$$

And

$$A = \frac{I_0 \beta \eta}{2k_c} \qquad for - L \le x \le 0 \tag{6}$$

Here, Cs is the specific heat capacity of the sample at constant pressure, and ρ_s represents the density of the sample. The absorbed light's efficiency is given by η at wavelength λ is converted into heat through nonradiative deexcitation processes. The value of η is considered unity, which is assumed for most solids at room temperature. To solve the thermal diffusion equations, proper boundary conditions have been used. Here the boundary conditions for the temperature and heat flux at the sample surface are given by

$$\zeta_a(0,t) = \zeta_s(0,t) \tag{7}$$

$$\zeta_b(-L,t) = \zeta_s(-L,t) \tag{8}$$

$$k_g \frac{\partial \zeta_g(0,t)}{\partial x} = k_s \frac{\partial \zeta_s(0,t)}{\partial x} \tag{9}$$

$$k_b \frac{\partial \zeta_g(-L, t)}{\partial x} = k_s \frac{\partial \zeta_s(-L, t)}{\partial x} \tag{10}$$

Using the above boundary conditions (Eqn 7-10) in the thermal wave equations, the constants can be determined. Those solutions are essential for evaluating the cell's temperature distribution in terms of optical, thermal, and geometric parameters of the system. Thus, the general solution of the equation is given as,

$$\zeta_s(x,t) = a_1 + a_2 x - \frac{1}{\beta^2} e^{\beta x} + \zeta_1(x) e^{i\omega t}$$
(11)

Where,
$$\zeta_1(x) = Ue^{\lambda_S x} + Ve^{-\lambda_S x} - \left(\frac{A}{\beta^2 - \lambda_S^2}\right)e^{\beta x}$$
 (12)

And
$$\lambda_s = (1+i)a_s$$
 (13)

Here,
$$\frac{1}{\alpha_s} = (2\alpha_s i\omega)^{1/2}$$
 (14)

And $\lambda_s = (1+i)a_s$ (13) Here, $\frac{1}{\alpha_s} = (2\alpha_s i\omega)^{1/2}$ (14) Like a1, a2, U, and V, the other constants can be determined using boundary conditions at x=0 and x=-L.

Appendix B

• <u>Terahertz (THz) Experimental Arrangement:</u>

The experimental arrangement used for generation and detection of Terahertz (THz) is as follows:

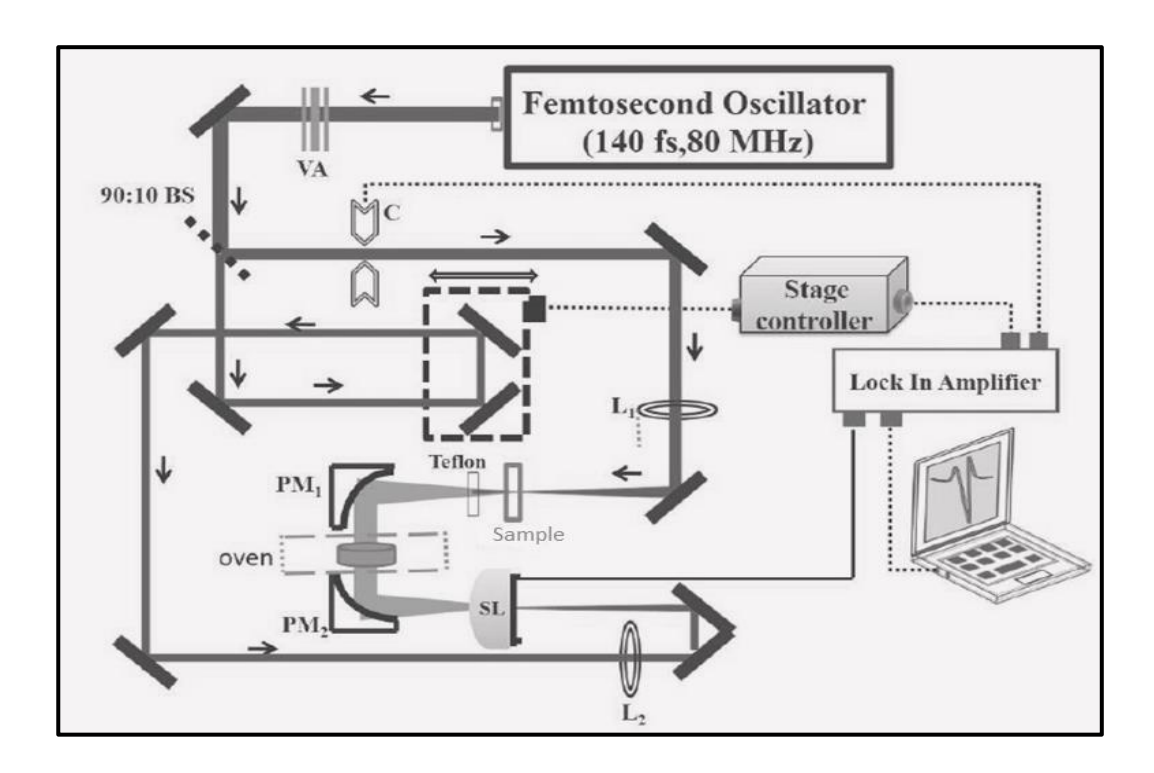


Fig. 1: shows the experimental setup used for THz generation using crystals and its detection with the help of by Photoconductive (PC) antenna. The various symbols used in the diagram are as follows: (VA-Variable attenuator, BS-Beam Splitter, C - mechanical chopper, L_1 & L_2 - Plano Convex Lens, PM_1 & PM_2 –parabolic mirrors, and SL- Hyper hemispherical silicon lens connected to the PC antenna) [ref: 1,2]

This experiment was performed using an UV-Vis-NIR spectrometer, temperature-tuned modified UV-Vis-NIR spectrometer and a Ti: Sapphire laser for femtosecond Laser pulses. The experiment is subdivided into three sections: (1) Using Femtoseconds Laser Pulses: The commercially available CdTe crystal (M/s Eksma Co. Ltd) and LT-GaAs based PC antennas were employed for generation and detection of THz radiation. The thickness, diameter and orientation of employed crystal are of the order 0.5 mm, 15 mm and <110> orientation, respectively. The experimental arrangement for THz emission and detection is same as in reference [1,2], with the slight modification of introducing a temperature-controlled oven containing the sample as shown in fig 2. The coherent chameleon ultra-II (~ 140 fs at 80 MHz repetition rate) was employed which is tunable between 680 - 1080 nm wavelength ranges as the laser source in this experiment. A variable attenuator (VA) was used to attenuate the incident laser pulses and the laser beam with selective average power before being allowed to incident on the nonlinear crystal (CdTe) which works as the source of THz radiation. This crystal was housed in a high precession rotation mount (WP-840-0186) for varying its

azimuthal. The employed pump and probe powers were of the order of 300 and 75 mW, respectively. The residual pump beam from CdTe source crystal is eliminated using the combination of Teflon and polyethylene filters. The generated radiation was maximized by azimuthally rotation of the crystal and polarization of laser pulses and the generated THz radiation was detected with the help of photoconductive sampling technique. The generated THz radiation from crystals was collimated and focused onto the THz detector i.e. PC antennas (gap \sim 5 μ m, length \sim 20 μ m) by two parabolic mirrors (PM₁ & PM₂). The transmitted portion of the probe beam of the beam obtained from the beam splitter was delayed with respect to THz radiation using a translation stage. The probe beam was focused by using another Planoconvex lens of focal length 50 cm. The focused probe beam was allowed to incident on the detecting antenna and its output was fed to low noise current preamplifier that is connected to voltage input of SR830 lock-in Amplifier. The obtained THz pulses were measured in temporal domain with respect to the delay in the probe beam. The temporal profiles were recorded with 100 ms time constant (i.e. in lock in amplifier).

Appendix C

Explosive materials are a highly reactive substance that consists of an enormous amount of potential energy, which is also known as High Energy Materials (HEMs). Based on structure and performance, explosives have been classified into many types (Fig. 3). Basically, explosives are classified as low and high explosives and both types are further classified into different forms. The detonation velocity rates of low explosives, such as propellants, smokeless powder, black powder, pyrotechnics, etc. are lower (cm s⁻¹). In contrast, high explosives detonate at much higher velocities of the order of km s-1. High explosives have also been subdivided into three groups according to their function, i.e. primary explosives, secondary explosives, and tertiary explosives. Primary explosives, which include lead azide and lead styphnate, are highly susceptible to initiation and are often referred to as 'initiating explosives' because they can be used to ignite secondary explosives. Secondary explosives, which include nitroaromatics and nitramines are much more prevalent at military sites than primary explosives. This category of explosives is often used as main charge or bolstering explosives because they are formulated to detonate only under specific circumstances. Secondary explosives can be loosely categorized into melt-pour explosives which are based on nitroaromatics, such as trinitrotoluene (TNT), dinitro toluene (DNT) and plastic-bonded explosives which are based on a binder and crystalline explosive, such as hexahydro-1,3,5 trinitroazine (RDX).

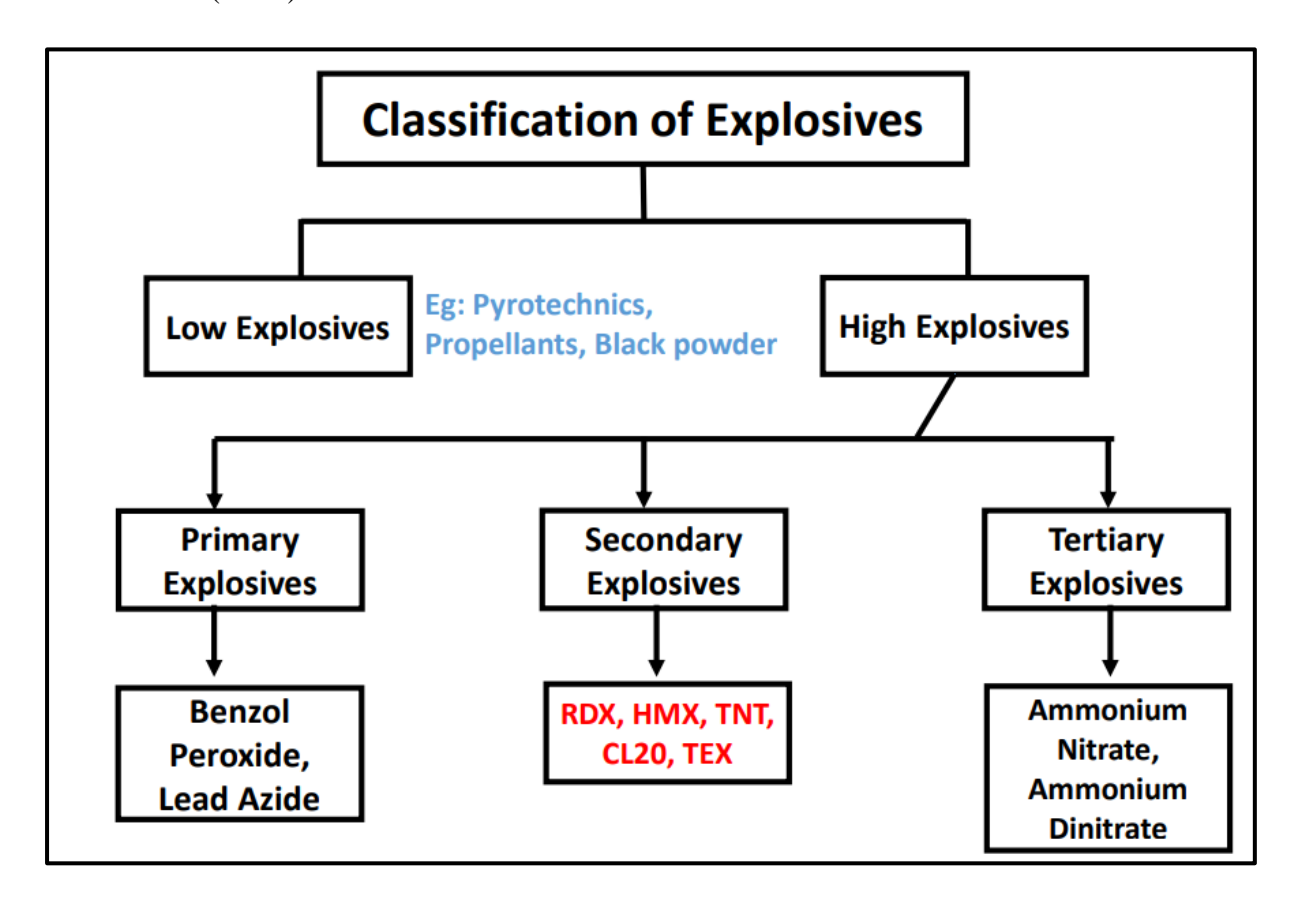


Fig. 1: This figure schematically represents the classification of High Energy Materials

Table 1 shows some of the characteristics of the explosives used in this thesis:

Table 1

S.No.	Compound	Compound Class	Formula
1.	RDX	Nitramines	$C_3H_6N_6O_6$
	(Trinitro-	$(C-N-NO_2)$	
	triazacyclohexane)		
2.	TNT	Aromatic Nitro	C7H5N3O6
	(2,4,6-Trinitrotoluene)	$(C-NO_2)$	
3	HMX	Nitramines	C ₄ H ₈ N ₈ O ₈
	(Tetranitro-tetraazacyclo-	$(C-N-NO_2)$	
	octane)		
4.	CL20	Nitroamine	$C_6H_6N_{12}O_{12}$
	(Hexa-	(H_2N-NO_2)	
	nitrohexaazaisowurtzitane)		
5.	TEX	Nitramines	C ₆ H ₆ N ₄ O ₈
	(4,10-dinitro-2,6,8,12-	$(C-N-NO_2)$	
	tetraoxa-4,10-		
	diazatetracyclo		
	$[5.5.0.0^{5,9}.0^{3,11}]$ -dodecane)		

Table: 1 shows the compound class and chemical formula of the explosive samples considered for the study

• Details of PEDOT Conducting Conjugate Polymer

Electrically conducting polymers have found wide applications in the field of electronics and bioelectronics among various other applications in the field of chemistry and spectroscopic studies. A large number of conducting polymers are available, both commercially as well as those synthesized in laboratories. Poly(3,4-ethylenedioxythiophene) or commonly known as PEDOT, is one such conducting polymer which is available commercially under the name of Poly (styrene sulfonate) or (PEDOT: PSS) as well as it can be easily synthesized. PEDOT has attracted much interest as a conjugated polymer due to its high conductivity, excellent chemical stability and good optical properties. It finds use in the field of organic electronics as transparent conductive oxides (TCO) as a hole-conducting layer or electrochromic layer in a variety of devices such as organic light-emitting diodes (OLEDs) and organic photovoltaic devices (OPVs), and the field of electrochromic. Recently, it has also found its application as effective biosensors. Fig 4 shows the structure of the polymer. It is the most successful conducting polymer in terms of practical application. It possesses many unique properties, such as good film-forming ability by versatile fabrication techniques, superior optical transparency in visible light range, high electrical conductivity, intrinsically high work function and good physical and chemical stability in air.

Appendix D

• Classical Theory of Raman Scattering:

According to classical theory, Raman Scattering can be explained as follows: the electric field strength, E, of the EM wave (Laser beam), fluctuates with time, t, and can be represented as:

$$E = E_0 cos 2\pi v_0 t \tag{1}$$

If a diatomic molecule is irradiated by this light, an electric dipole moment is induced, which is given as,

$$P = \alpha E(2)$$

$$P = \alpha E_0 \cos 2\pi \nu_0 t \tag{3}$$

Here, α is a proportionality constant known as polarizability. If the molecule vibrates with a frequency, ν_m , then the nuclear displacement, q, can be expressed as,

$$q = q_0 cos2\pi v_m t \tag{4}$$

The value of α is a linear function of q for a small amplitude of vibration. Thus, at the equilibrium position,

$$\alpha = \alpha_0 + \left(\frac{\partial \alpha}{\partial q}\right)_0 q_0 + \cdots \tag{5}$$

Combining equations, (3), (4), and (5);

$$p = \alpha E_0 cos 2\pi \nu_0 t$$

$$p = \alpha E_0 cos 2\pi \nu_0 t + \left(\frac{\partial \alpha}{\partial q}\right)_0 q E_0 cos 2\pi \nu_0 t$$

$$p = \alpha E_0 cos 2\pi \nu_0 t + \left(\frac{\partial \alpha}{\partial q}\right)_0 q_0 E_0 cos 2\pi \nu_0 t cos 2\pi \nu_m t$$

$$p = \alpha E_0 cos 2\pi \nu_0 t + \frac{1}{2} \left(\frac{\partial \alpha}{\partial q}\right)_0 q_0 E_0 [\cos\{2\pi(\nu_0 + \nu_m)t\} + \cos\{2\pi(\nu_0 - \nu_m)t\}]$$
(6)

The first term of Eqn. (6) represents the oscillating dipole that has a frequency, ν_0 which represents the Rayleigh Scattering while, the second term represents the Raman scattering of frequency, $\nu_0 - \nu_m$ (Stokes) and $(\nu_0 + \nu_m$ (anti-Stokes). Also, one important point to note is that if $\left(\frac{\partial \alpha}{\partial q}\right)_0$ is zero, then there is no Raman scattering or we can say that the molecule is not Raman-active. Thus, to be Raman-active, the rate of change of polarizability; α , with the vibration has to be non-zero.

The vibrational spectrum of a molecule has bands representing active normal vibrations. The Raman spectrum depends on various factors such as the mass of the atoms in the molecule, the strength of their chemical bonds, and the atomic arrangement. Different molecules have different vibrational spectra, which are known as their fingerprint spectra because of its uniqueness. Vibrational Raman spectroscopy is not limited to intramolecular vibrations. Some of the Crystal lattice vibrations are also Raman-active. Their spectra are important in various research fields such as polymers and semiconductors.

Appendix E

• Absorption Coefficient and Refractive Index of antibiotic Cefixime drug:

The time-domain terahertz signal received after passing through the samples was converted into frequency domain spectra using FFT. The value of absorption coefficient (α (ω)) was calculated form FFT spectrum. The transmitted field T is given by equation (1):

$$T = \frac{E_{sample}}{E_{\text{Re ferance}}} \tag{1}$$

Where S_{ample} and $R_{eference}$ are the amplitudes of THz radiation after passing through material and reference samples, respectively. We can calculate the effective thickness (l) of the sample distributed in PTFE (Teflon) matrix using formula

$$l = \frac{m}{\rho} \frac{4}{\Pi D^2} \tag{2}$$

Here, 'm'is the weight of the sample (100 mg), 'D'represents the diameter of sample (12 mm), and ' ρ ' is the density of the sample. Since the pellets contains mixture of two sample absorption coefficient (α) can be ascertained using formula [1-2].

Absorption coefficient(
$$\alpha$$
) = $-\frac{1}{l} \ln \frac{T_m}{T_s}$ (3)

Where l is the effective thickness of the sample and T_m , T_R are the transmitted intensity from material sample and reference, respectively. The Refractive index of the sample can be calculated by using equation (9).

$$n = 1 + \frac{\Delta \phi \times c}{2\pi \nu \times d} \tag{4}$$

Where $\triangle \phi$ represents the phase difference between reference and sample, v is frequency, dis thickness of pellet and cis the velocity of light. The refractive index then, can be represented using Kramer's -Kronig model as,

$$n=n+i\kappa$$
 (5)

Where n is the real part of the refractive index and κ is the extinction coefficient which is related to the power absorption coefficient (α). Fig. 1 (a & b) represent the absorption coefficient and the refractive indices of the samples with respect to frequency respectively.

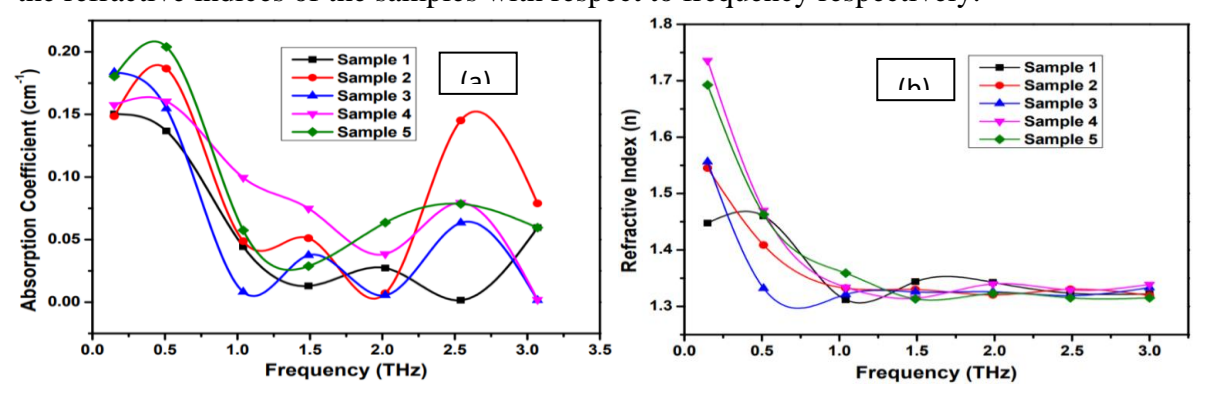


Fig. 1 (a & b): shows the absorption coefficient and the refractive index of the medicine samples 1-5.

• References:

- 1. V Mottamchetty and A K Chaudhary, Improvised design of THz spectrophotometer using LT-GaAs photoconductive antennas, pyroelectric detector and band-pass filters, Indian J Phys, 90, 73-78 (2015)
- 2. Ganesh Damarla, M. Venkatesh, and A. K. Chaudhary, Temperature-dependent terahertz spectroscopy and refractive index measurements of aqua-soluble and plastic explosives, 57, 29,8743-8750 (2018)